**Title**
Manipulating Light and Matter with Non-Conventional Metamaterials



**Author**
Ren, Xuexin

**Publication Date**
2019

Peer reviewed|Thesis/dissertation

# Manipulating Light and Matter with Non-Conventional Metamaterials

By

Xuexin Ren

A dissertation submitted in partial satisfaction of the
requirements for the degree of
Doctor of Philosophy
in
Applied Science & Technology
in the
Graduate Division
of
University of California, Berkeley

Committee in charge:
Professor Xiang Zhang, Chair
Professor Jie Yao
Professor Boubacar Kanté

# Abstract

## Manipulating Light and Matter with Non-Conventional Metamaterial

By

Xuexin Ren

Doctor of Philosophy in Applied Science & Technology

University of California, Berkeley

Professor Xiang Zhang, Chair

Metamaterials are artificial materials that consist of subwavelength unit cells (meta-atoms). They attain their electromagnetic properties from the unit cell response rather than the constituent materials, and can be designed to exhibit properties that are not readily found in natural materials. In the past decade, the study of metamaterials has opened up a route to many exciting applications, such as superresolution imaging and invisibility cloaks.

In recent years, metasurfaces, which can be considered as two-dimensional metamaterials, have attracted intensive research interests. Due to their reduced dimensionality, metasurfaces are much easier to fabricate and yet offer a higher degree of freedom in molding the flow of waves (optical, acoustic), compared to bulk metamaterials. Being optically thin, metasurface has reduced absorptive loss and thus offers higher efficiency. Metasurfaces utilize resonances to achieve abrupt phase shifts on subwavelength scale distances, in contrast to traditional optical devices that rely on propagation effect.

We are interested in investigating non-conventional interactions between light and meta-atoms. We show that by introducing novel types of light-matter interactions mediated by metamaterials, new degrees of freedoms can be elevated for precise controlling of light and matter at the nanoscale.

This dissertation consists of three independent studies: 1. We design a color sorting metasurface under the regime where neighboring meta-atoms are strongly coupled. The coupling enabled enhanced quality factor and reduced detrimental crosstalk, leading to a color sensor with a pixel size below the diffraction limit. 2. We study the interaction of metasurface with quantum light. By engineering the quantum vacuum by a phase gradient metasurface, we theoretically show that quantum interference and coherence and be induced in emitter transitions. 3. We investigate the magnetic interactions between light and meta-atoms that exhibit artificial optical magnetism, and perform the first demonstration that magnetic interactions can be applied to trap and manipulate nanoscopic particles.

Dedicated to my parents
Dong Ren and Yuanfang Sun

Dedicated to my husband
Haokun Li

# TABLE OF CONTENTS

## List of Figures and Tables

# Acknowledgement

My PhD journey at UC Berkeley is full of frustration and joy, hardship and excitement. It is a journey that is as rewarding as it is depressing. I am indebted to many people whose guidance and support enabled me to finish this journey. I could not have made it without all these people.

First of all, I want to express my sincere gratitude for my research advisor, Professor Xiang Zhang, who brought me to this amazing lab and trusted me with the freedom and resources to grow as a researcher. His guidance and support, both scientific and non-scientific, has been invaluable to me throughout the PhD process. His enthusiasm and curiosity for science, critical thinking ability, as well as confidence and passion in life will continue to guide and inspire me in my future career.

I'm also very grateful to all the other XLab members for creating such a creative, energetic environment and for the friendships we built over the years. I especially want to thank Dr. Yuan Wang, Dr. Sui Yang, Dr. Rongkuo Zhao, Dr. Joseph Smalley, Dr. Nir Shitrit, Dr. Pankaj Jha, Dr. Ying Wang and Dr. Xingjie Ni for the valuable discussions and collaborations. And also a special thank to Dr. Ying Wang for being a wonderful friend and the other female in XLab! I would also like to thank Professor David Attwood, Professor Jie Yao, Professor Boubacar Kante, Professor Hartmut Haeffner, Professor Junqiao Wu, Professor Feng Wang and Professor Norman Yao for serving my prelim, qualifying exam and dissertation committee. Their insights have been very important to my research.

Also, thank you my dear friends: Qian Zhong, Yi Chen, Xiaoya Qu and Siqi Wang for all the laughter and joy we shared together! Finally, I am very blessed for having my husband Haokun by my side throughout the whole PhD life. His love and support makes this tough journey sweet and joyful.

# Chapter 1

# Introduction

## 1.1 Introduction and motivation

Metamaterials are artificial materials that consist of subwavelength unit cells (meta-atoms). They attain their electromagnetic properties from the unit cell response rather than the constituent materials, and can be designed to exhibit properties that are not readily found in natural materials. Since Pendry and co-authors' proposal of using metallic wires [1] and split-ring resonators [2] to realize negative permittivity and negative permeability [3] respectively, metamaterials have gained monumental research interests. The study of metamaterials has opened up a route to many exciting applications, such as superresolution imaging [4,5] and invisibility cloaks [6].

In recent years, metasurfaces, which can be considered as two-dimensional metamaterials, have attracted intensive research interests. Due to their reduced dimensionality, metasurfaces are much easier to fabricate and yet offer a higher degree of freedom in molding the flow of waves (optical, acoustic), compared to bulk metamaterials. Being optically thin, metasurface have reduced absorptive loss and thus offer higher efficiency. Metasurfaces utilizes resonances to achieve abrupt phase shift on a subwavelength scale distances [7-9], in contrast to traditional optical devices that rely on propagation effect.

By carefully designing each meta-atom to locally control the phase shift, the so-called phase gradient metasurface can tailor wavefronts at will. Typical examples of meta-atoms include multi-resonance antennas [7,8], gap-plasmon resonators [10,11], Pancharatnam-Berry-phase structures [12], and Huygen's atoms [13]. The outstanding optical performance and design flexibility of phase gradient metasurface has led to the development of various planar optical devices, such as metasurface planar lens [14,15], meta-holograms [16,17], and multi-functional metasurfaces [18-19].

This dissertation focuses on the development of non-conventional metamaterials and metasurfaces that have unique physics beyond the classical regime. Instead of assuming negligible interactions between meta-atoms in classical metasurfaces, we show that the coupling can be utilized to manipulate light at the deep subwavelength scale. Observed

phenomena, such as enhanced quality factor and reduced detrimental crosstalk has been applied to the design of CMOS color detector with subwavelength pixel size.

Furthermore, by engineering the coupling between metasurfaces and classical/quantum emitters mediated by light, we theoretically show that emitter properties can be manipulated to induce quantum interference, entanglement and coherence between different transitions. Finally, we study the magnetic interactions between light and meta-atoms that exhibit artificial optical magnetism, and perform the first demonstration that magnetic interactions can be applied to trap and manipulate nanoscopic particles. We show that by elevating novel types of light-matter interactions mediated by metamaterials, we can open up new degrees of freedoms for precise controlling of light and matter at the nanoscale.

## 1.2 Dissertation Outline

The dissertation consists of three chapters (excluding the introduction and conclusion chapter), each of which describes an independent research project. Chapter 2 contains studies of new design principles of metasurface beyond the phase gradient regime. Conventional phase gradient metasurfaces work in the regime where the meta-atoms need to be well separated such that the interaction between neighboring meta-atoms is negligible. Previously it has been demonstrated that by precisely controlling the coupling efficiency of two closely spaced plasmonic nano-antennas, manipulation of light at the deep subwavelength scale can be realized [20]. Based on this principle, we designed a color sorting metasurface where the neighboring meta-atoms strongly couple to each other. By engineering the coupling between neighboring meta-atoms, we are able to design a visible color sensor with unprecedentedly small pixel size.

Chapter 3 brings the classical metasurfaces to the quantum regime. Although typically metasurface is used to control the wavefront of classical light, they can also be applied to interact with and manipulate quantum light. By using metasurface to engineer vacuum properties, we theoretical show that strong quantum interference (coherence) can be induced in three-level systems [21]. Metasurfaces interfaced with quantum emitters and 2D materials have the potential to opening up opportunities for on-chip quantum state engineering and material property engineering.

In Chapter 4, instead of manipulating light with light-matter interaction, we look at the reverse problem: optical manipulation of nanostructures' kinetic motion. Specifically, we are interested in optical trapping and manipulation of nanostructures with the magnetic part of light. In the absence of natural magnetism, optical trapping forces have previously been based purely on electric interactions. However, as the emergence of the metamaterial concept, several classes of nanostructures including plasmonic nanoclusters and high-index dielectric particles have been proposed and demonstrated to possess artificial optical magnetism. Here we demonstrate trapping and transport of high-index dielectric particles

with optical magnetism. Elevating magnetic interactions between light and particles can open up a new degree of freedom for optical manipulation of microscopic objects.

Finally, in Chapter 5, we measured the negative refractive index in a chiral metamaterials. Negative refractive index has traditionally been achieved by the simultaneous realization of negative permittivity and negative permeability [3]. Recently, an alternative route to realizing negative refraction has been proposed by utilizing chirality. Due to the cross coupling of electric and magnetic field in a chiral medium, the degeneracy of the two circularly polarized waves is broken, and the refractive index is increased for one circular polarization and reduced for the other. If the chirality $\kappa$ is strong enough, negative refraction may occur for one circularly polarized wave even when both permittivity and permeability are positive.

## References


[1] Pendry, John B., et al. "Extremely low frequency plasmons in metallic mesostructures." *Physical Review Letters* 76.25 (1996): 4773.

[2] Pendry, John B., et al. "Magnetism from conductors and enhanced nonlinear phenomena." *IEEE Transactions on Microwave Theory and Techniques* 47.11 (1999): 2075-2084.

[3] Veselago, Viktor G. "The electrodynamics of substances with simultaneously negative values of ε and μ." *Soviet Physics Uspekhi* 10.4 (1968): 509.

[4] Pendry, John Brian. "Negative refraction makes a perfect lens." *Physical Review Letters* 85.18 (2000): 3966.

[5] Fang, Nicholas, et al. "Sub–diffraction-limited optical imaging with a silver superlens." *Science* 308.5721 (2005): 534-537.

[6] Schurig, David, et al. "Metamaterial electromagnetic cloak at microwave frequencies." *Science* 314.5801 (2006): 977-980.

[7] Yu, Nanfang, et al. "Light propagation with phase discontinuities: generalized laws of reflection and refraction." *science* 334.6054 (2011): 333-337.

[8] Ni, Xingjie, et al. "Broadband light bending with plasmonic nanoantennas." *Science* 335.6067 (2012): 427-427.

[9] Sun, Shulin, et al. "Gradient-index meta-surfaces as a bridge linking propagating waves and surface waves." *Nature Materials* 11.5 (2012): 426-431.

[10] Sun, Shulin, et al. "High-efficiency broadband anomalous reflection by gradient meta-surfaces." *Nano letters* 12.12 (2012): 6223-6229.

[11] Pors, Anders, et al. "Gap plasmon-based metasurfaces for total control of reflected light." *Scientific reports* 3 (2013).

[12] Hasman, Erez, et al. "Polarization dependent focusing lens by use of quantized Pancharatnam–Berry phase diffractive optics." *Applied physics letters* 82.3 (2003): 328-330.

[13] Decker, Manuel, et al. "High‐efficiency dielectric Huygens' surfaces." *Advanced Optical Materials* 3.6 (2015): 813-820.

[14] Khorasaninejad, Mohammadreza, et al. "Metalenses at visible wavelengths: Diffraction-limited focusing and subwavelength resolution imaging." *Science* 352.6290 (2016): 1190-1194.

[15] Lin, Dianmin, et al. "Dielectric gradient metasurface optical elements." *Science* 345.6194 (2014): 298-302.

[16] Ni, Xingjie, et al. "Metasurface holograms for visible light." *Nature communications* 4 (2013): 2807.

[17] Zheng, Guoxing, *et al.* "Metasurface holograms reaching 80% efficiency." *Nature nanotechnology* 10.4 (2015): 308-312.

[18] Maguid, Elhanan, et al. "Photonic spin-controlled multifunctional shared-aperture antenna array." *Science*(2016): aaf3417.

[19] Arbabi, Amir, et al. "Dielectric metasurfaces for complete control of phase and polarization with subwavelength spatial resolution and high transmission." *Nature nanotechnology*10.11 (2015): 937-943.

[20] Zhang, Shuang, et al. "Anti-Hermitian plasmon coupling of an array of gold thin-film antennas for controlling light at the nanoscale." *Physical Review Letters* 109.19 (2012): 193902.
[21] Jha, Pankaj K., et al. "Spontaneous exciton valley coherence in transition metal dichalcogenide monolayers interfaced with an anisotropic metasurface." *Physical review letters* 121.11 (2018): 116102.

# Chapter 2

# Manipulating Light below Diffraction Limit with Non-Hermitian Metasurfaces

Classical metasurfaces work in the regime where the meta-atoms need to be well separated such that the interaction between neighboring meta-atoms is negligible [1,2]. Consequently, each meta-atom can be treated independently and the functionality of the whole metasurface is derived from individual meta-atoms. Recently, however, it has been shown that by tailoring the couplings between closely spaced plamonic nano-attennas, spatial manipulation of light at the deep subwavelength scales could be realized [3]. Here we develop novel type of metasurfaces, where the neighboring meta-atoms can be strongly coupled and the coupling efficiencies are uniquely engineered.

Specifically, we demonstrate that color sensing can be achieved in a with subwavelength pixel size based on an anti-Hermitian coupled silicon metasurface. Spectral filtering is achieved through structural color rather than transmissive filters, namely through Mie resonances in silicon nanoresonators, with carefully controlled separation distances, leading to simultaneously high color purity and quantum efficiency.

Our metasurface pixel array is the first demonstration of anti-Hermitian coupling in a CMOS compatible platform, sorting three colors over a 100 nm bandwidth in the visible regime, independently of the polarization of normally-incident light. The two-dimensional, 60 μm by 60 μm array, contains over 28,000 pixels, each with an area less than half a squared wavelength of the absorbed light. Furthermore, the quantum yield is comparable to commercial photodetectors, with a responsivity exceeding 0.3 A/W. Our demonstration lays the foundation for the realization of CMOS color and image sensors with revolutionarily small pixel sizes.

## 2.1 Non-Hermitian Coupled Meta-Atoms

Meta-atoms can be viewed as quasi-bound states, which interact with each other via direct near-field coupling as well as indirect coupling mediated by the open radiative channels. Indirect couplings in quasi-bound states have been widely studied in various open quantum systems, including nuclei, atoms, molecules, and quantum dots [4-6]. It has been shown that the indirect coupling gives rise to an imaginary, or anti-Hermitian coupling matrix in the system [4]. The original and unperturbed eigenstates in the system hybridize to form new eigenstates, and due to the anti-Hermitian coupling, some of the new eigenstates are decoupled from the decay channels, and have very long lifetimes; while others have enhanced decay rates and can radiate very strongly (superradiant state).

In plasmonic systems, anti-Hermitian couplings have played an important role in introducing interference among different excitation pathways. Aside from the well-studied plasmon induced transparency [7,8] and interacting dark resonance [9], which comes from destructive interference between isolated and continuum states, opposite phenomena, such as electromagnetically induced absorption and superscattering have also been demonstrated. Recently, it has been shown that the anti-Hermitian coupling could also be used to spatially manipulate light at the deep subwavelength scale [3]. By designing an anti-Hermitian coupling matrix, a system of plasmonic meta-atoms closely packed within only l/15 separations can be individually excited from the far field, which are otherwise indistinguishable from each other.

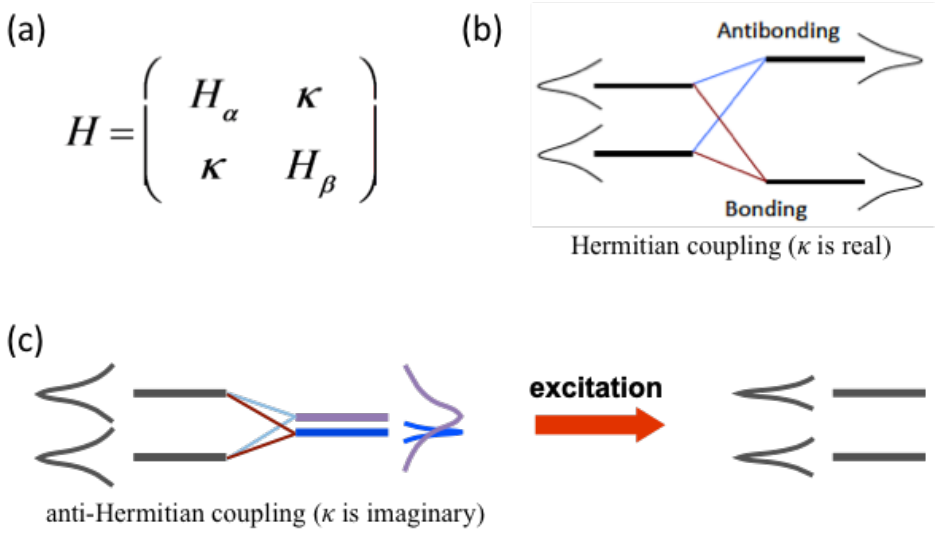


**Figure 2.1.1** Mechanism of Hermitian and anti-Hermitian coupling. (a) Hamiltonian of a system consists of two coupled resonators, where κ denotes the coupling constant. (b) A Hermitian coupled system forms two new eigenstates with increased energy difference and similar decay rates. (c) An anti-Hermitian coupled system forms two new eigenstates with similar energy but very different decay rates (one of them has an enhanced decay rate and the other has a decreased decay rate). When the system size is smaller than wavelength and under plane wave excitation,

two simultaneously excited eigenstates interfere constructively at one resonator and destructively at the other, leading to a highly localized state.

Recently, dielectric resonators have attracted growing interests as the building blocks for metasurface, since they have very low material loss comparing to the plasmonic structures [10,11]. However, the field confinement in dielectric structures cannot compare favorably with the plasmonic resonators, creating new problems such as radiation loss and detrimental cross talking between neighboring resonators. To address these problems, we use the theory of anti-Hermitian coupling to obtain greater control of the coupling among the resonators.

We study a system that consists of two closely spaced dielectric antennas, where the resonant wavelength of each antenna is slightly different (Fig. 2.1.2 left). Due to the strong coupling between the antennas, the eigenstates of the system become hybridized excitations of two resonators. Therefore, in general, under plane wave excitation, both antennas will be excited. However, we found that when the coupling is purely imaginary (anti-Hermitian), two simultaneously excited eigenstates interfere constructively at one resonator and destructively at the other, leading to a highly localized state.

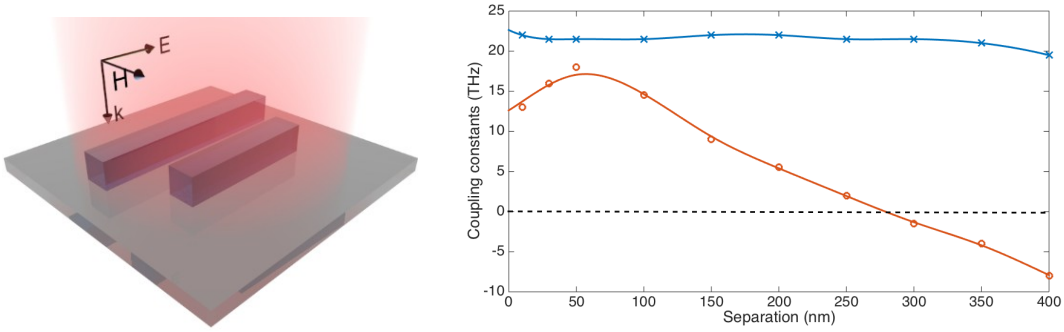


**Figure 2.1.2** Numerical retrieval of the indirect anti-Hermitian coupling between two dielectric nanoantennas. (Left panel) A photonic system consisting of two optical nanoantennas made of silicon. (Right panel) The retrieved real part (red circle) and imaginary part (blue cross) of optical coupling constant between the two antennas as a function of their edge-to-edge separation. The red and blue solid lines are the polynomial fittings for the real and imaginary parts, respectively.

The coupling between the two dielectric resonators consists of a direct near field coupling and an indirect far field coupling. Generally, the overall coupling coefficient is a complex number. However, by precisely choosing the antenna separation, the real part from the direct and indirect coupling exactly cancel each other, and anti-Hermitian coupling can be reached (Fig. 2.1.2 right). At small separations, the real (Hermitian) part of the coupling coefficient is dominated by the direct near-field coupling between the two antennas. With increasing distance, the near-field coupling decreases rapidly, and when

the direct near-field coupling is canceled by the real part of the indirect coupling among the bound states, the coupling between the two antennas become purely anti-Hermitian.

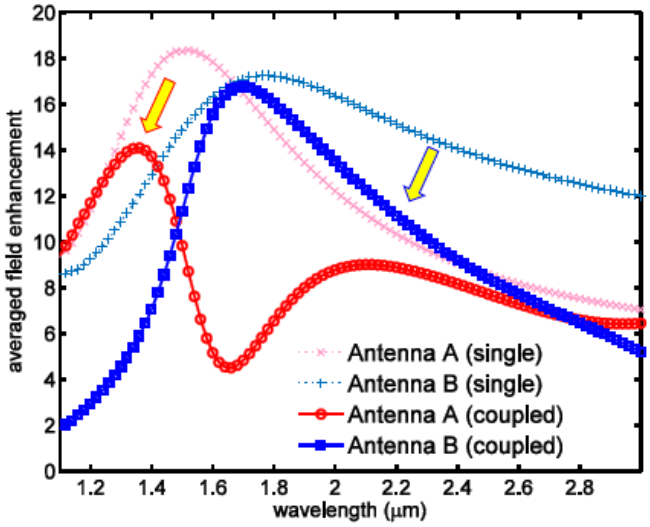


**Figure 2.1.3** Average field enhancement in a pair of dielectric antenna before and after anti-Hermitian coupling.

Figure 2.1.3 shows the average field enhancement in the two antennas without coupling and under anti-Hermitian coupling. It can be seen that with anti-Hermitian coupling, the quality factor of the two resonances increased by a factor a three, while the resonance positions remain approximately unchanged. This can be used as a treatment to reduce crosstalk between closely spaced resonators.

## 2.2 Color Sorting with Non-Hermitian Metasurface

As the form factor of optoelectronic systems becomes ever smaller, the specifications for color and image sensors become increasingly challenging to meet. The size of conventional pixels, which ultimately limits the image resolution for a given sensor area, or the sensor area for a specified resolution, cannot be continually decreased due to the fundamental constraints of light diffraction and charge carrier diffusion. For example, conventional pixel designs using transmissive filters and planar absorbing layers lead to optical and electrical crosstalk when the pixel dimension approaches wavelength scale, drastically reducing the signal-to-noise ratio of detectors [12,13].

Alternatively, optically thick plasmonic color filters have been realized [14-17], which can achieve pixel size down to a few microns. They are also superior to organic dyes regarding stability and design flexibility. However, the plasmonics color filters are still based on the conventional filtering scheme, which is intrinsically ineffective. Also, when further shrinking down the pixel size, the performance of the plasmonic color filters is limited by the detrimental color crosstalk between neighboring pixels [14].

In our work, we are designing an absorptive color sorting metasurface based on 3D silicon resonators. Comparing to the conventional filtering scheme, resonant absorptive color filters present the opportunity for very high photon efficiency [18,19]. From Mie theory, high-index dielectric or semiconductor particles support geometrical resonances, and the first and second orders of which are magnetic and electric dipole modes [20-23]. Upon excitation, the magnetic dipole mode can have a very strong field enhancement inside the particle. If the structure material is absorptive, then we expect strong selective color absorption from the magnetic dipole resonance. Here, we pattern silicon cylinder particles into hexagonal lattices. By varying the cylinder size, we are able to achieve chromatic light absorption at different wavelengths (Fig. 2.2.1).

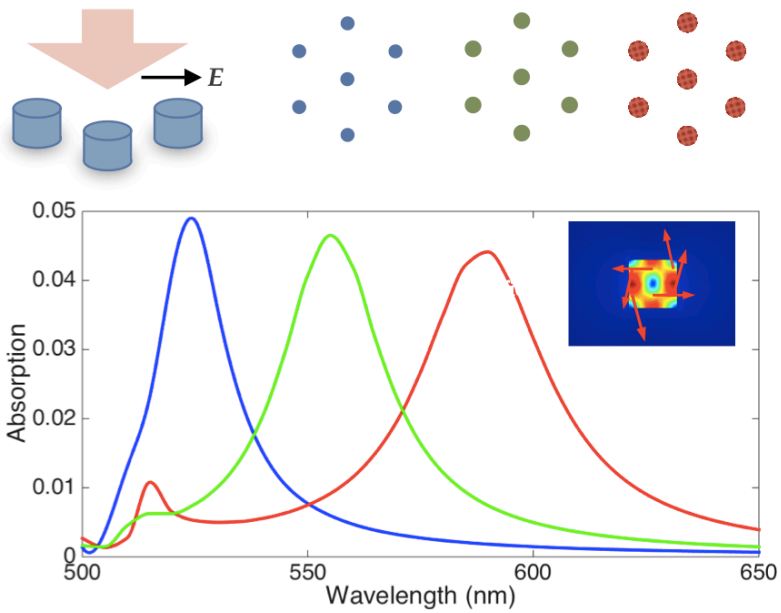


**Figure 2.2.1** Numerical simulation of the absorption spectra of the silicon cylinder lattices. Top panel: Top view of the three hexagonal silicon cylinder lattices. A beam is incident at normal direction onto the lattice. Bottom panel: Absorption spectra of three lattices with different cylinder size. The pitch of the hexagonal lattice is 1000 nm.

In the lattice designed above, each cylinder can be viewed as a single pixel, with sub-micron pixel size. However, for color imaging applications, we need to pattern the three lattices together, which will very likely induce color crosstalk among adjacent pixels (Fig. 2.2.2). Here, in order to solve this problem, we employs the concept of anti-Hermitian coupling to get better control of the mutual couplings among the lattices.

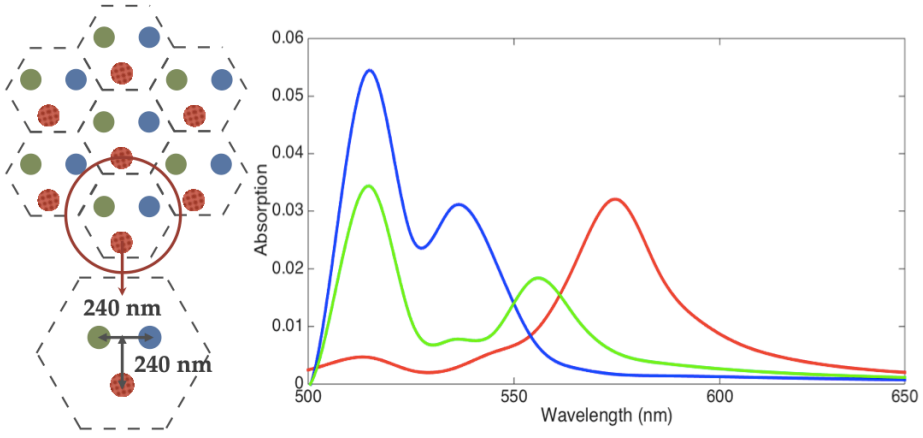


**Figure 2.2.2** Color crosstalk when patterning the three lattices together. Multiple peaks arise in a single resonator.

We calculated the coupling coefficients among the three sub-lattice modes with respect to their relative position shifts (figure 2.2.3). This is done by numerical simulation of the eigen-modes of two coupled lattices followed by numerical fitting according to the coupled mode theory. The coupling coefficient between two lattice modes is a function of their relative position shift $\boldsymbol{a_1}$ in a unit cell. When $\boldsymbol{a_1}$ is parallel to electric field direction (figure 2.2.4 middle), the coupling constant has an imaginary part that is only slightly smaller than the single lattice decay rate, which means that the two lattices primarily couple to a same decay channel. The imaginary part slowly decreases as the separation increases. The real part, on the other hand, crosses zero at around 10 nm separation. This is where the negative near field coupling exactly cancels with the indirect coupling and the anti-Hermitian coupling occurs. When there is a large angle between $\boldsymbol{a_1}$ and the electric field direction (figure 2.2.4 right), however, the indirect coupling between the two lattices becomes very small and the real part of the coupling coefficient is dominated by near field coupling. The anti-Hermitian point does not appear.

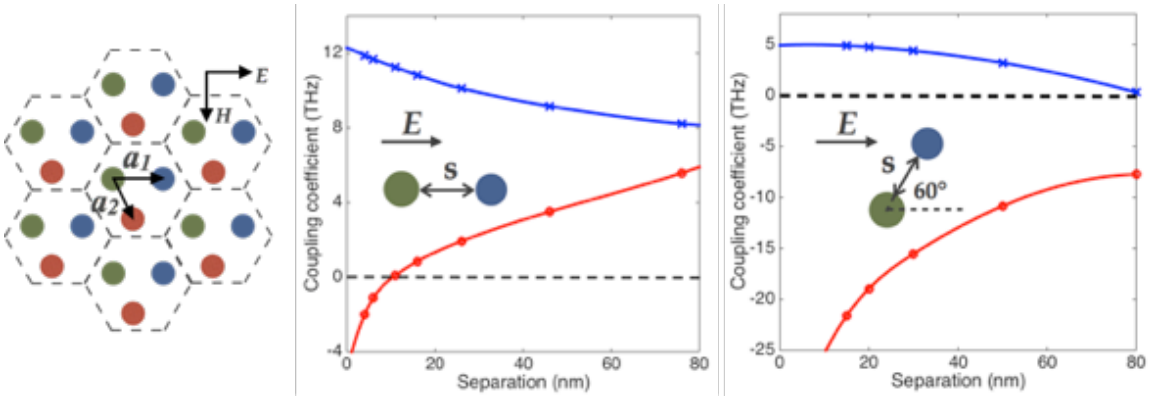


**Figure 2.2.3** Numerical retrieval of the coupling coefficient between the different lattices. (Left) Schematic view of the combined lattice consisting of three kinds of cylinder structures. We can vary the relative position shifts between the three lattices ($\mathbf{a_1}$, $\mathbf{a_2}$), until they reach the anti-Hermitian coupling point. (Middle and right) Numerically retrieved coupling coefficient between the blue and the green lattice with respect to their relative position shift. The x-axis of the plot is the separation between the two cylinders in the unit cell. Real part and imaginary part of the coupling coefficient are plotted in red and blue respectively. In the middle panel, $\mathbf{a_1}$ is parallel to the electric field. In the right panel, there is a 60-degree angle between $\mathbf{a_1}$ and electric field direction.

## Linear Design

Therefore, to maximize the indirect coupling and exploit the anti-Hermitian coupling, we pattern the three cylinders in a unit cell in a line parallel to electric field (Figure 2.2.4). In this way, both the coupling between blue and green, and green and red are anti-Hermitian. The coupling between blue and red is not, but since their resonance spectral

overlap is small, this has only a small effect over the performance of the system. From the simulation result of the coupled system (Fig. 2.2.4), we see that even at sub-micron pixel size, each chromatic pixel can be excited distinctively, and no harmful crosstalk appears. Note that the blue peak is significantly broader than predicted, which is because of the coupling between the blue mode and the electric dipole mode in the red and green lattice at around 520 nm wavelength.

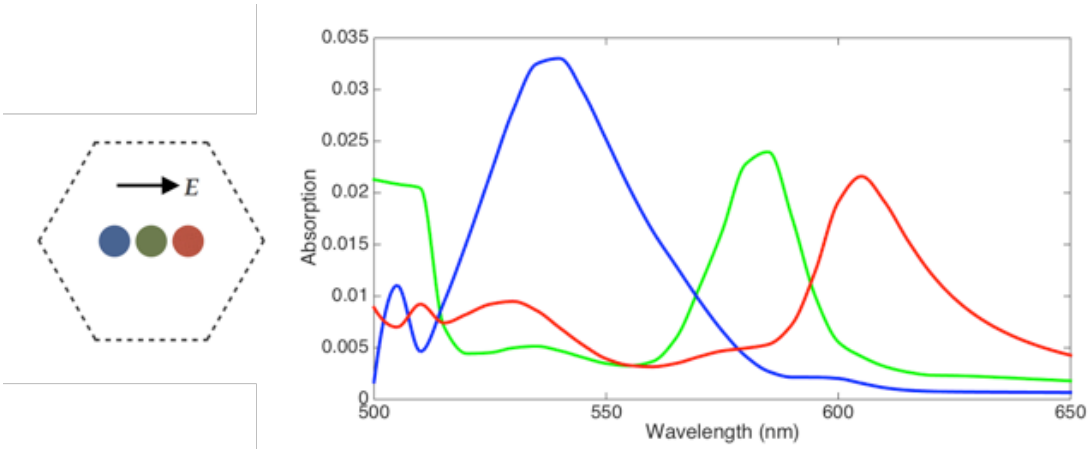


**Figure 2.2.4** Numerical simulation on the combined lattice with anti-Hermitian coupling between the sub-lattices. (Left) The unit cell of the combined lattice. (Right) Optical absorption spectrum of the combined lattice comprising of three kinds of cylinders. Selective excitation of a single sub-lattice can be seen from the spectrum.

## Isotropic Design

To maximize the use of incident light, we further developed an isotropic design to make the metasurface without polarization dependence. The scheme is shown in Figure 2.2.6. The three posts with different colors represent for three kinds of silicon cylinders with different absorption spectrum. The cylinders in one dash hexagon comprise a unit cell. To exploit the anti-Hermitian coupling, we first study the coupling between two combined lattices. We calculated the coupling coefficient between the blue and green lattices, the green and red lattices using numerical simulation. The corresponding anti-Hermitian coupling occurs at the separations of 53nm and 54nm, respectively. The coupling between the blue and red cylinders can be neglected, because the overlapping between their resonance spectrums is small and there's little crosstalk between the two lattices. By considering the overall coupling effect, we choose the lattice constant as 175nm, where the separations between the blue and the green lattices, and between the green and the red lattices are 63nm and 47nm, respectively. Both separations are close to the anti-Hermitian coupling condition so that there is still a good anti-Hermitian coupling effect.

The simulation results are shown in Fig. 2.2.5 (b) – (c). The blue, green and red solid lines in Figure 2.2.5 (b) are the absorption spectrums of the three different cylinders in the combined lattices. There is little crosstalk between the resonances. Figure 2.2.5 (c)

shows the electromagnetic energy density in one unit cell at the wavelengths corresponding to black dash lines in the absorption spectrum in Figure 2.2.5 (b), showing very high contrast between resonant cylinder and nearby non-resonant ones at different wavelength. Therefore, our current isotropic design can realize the color sorting at sub-micrometer pixel size (175nm) with little crosstalk and no polarization dependence. Besides, the separation between different nano-cylinders are much larger than the linear design (~50nm), allowing easier fabrication of the device.

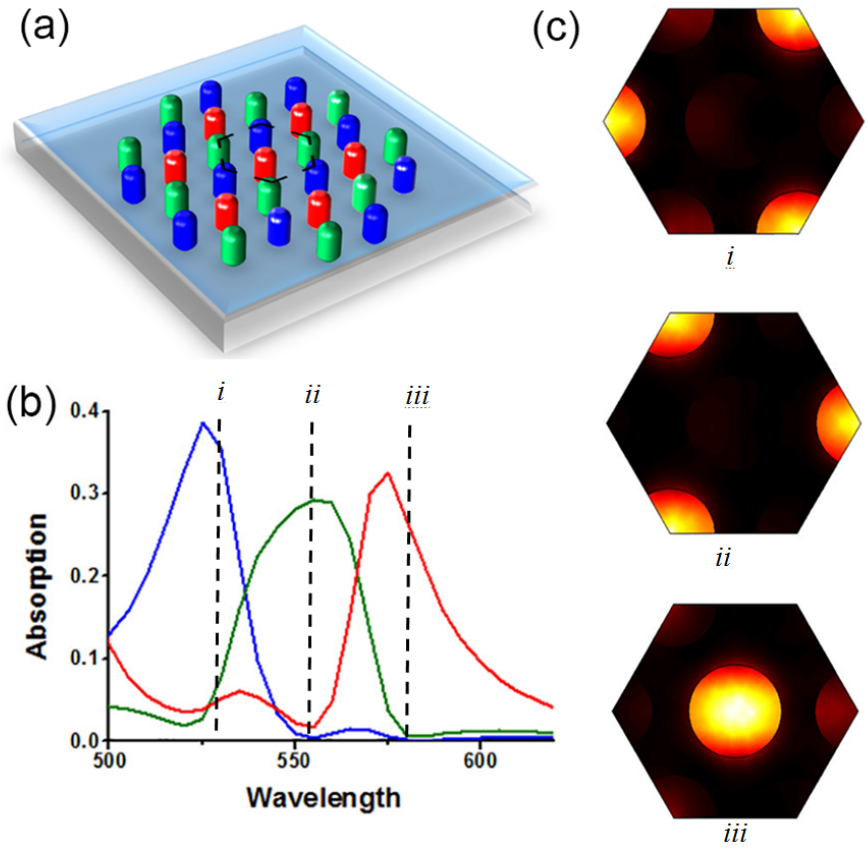


**Figure 2.2.5** Isotropic color sorting metasurface design for three colors. (a) Schematic of three color metasurface design. The three different kinds of cylinders in the black dashed hexagonal lattice constitute one pixel of the color sorting metasurface. The diameters of the blue, green and red cylinders are 104nm, 120nm and 136nm, with the height of 120nm. (b) Optical absorption spectrum calculated using numerical simulation of the combined isotropic lattice comprising of the three kinds of cylinders. The blue, green and red lines are the absorption spectrum of the blue, green and red cylinders in one unit cell. Selective excitation of a single sub-lattice can be seen from the spectrum. (c) Electromagnetic field energy density map at excitation wavelength of 530nm (i), 555nm (ii), and 580nm (iii).

## 2.3 Non-Hermitian Color Sorter Integrated with a CMOS Sensor

### 2.3.1 Device design

Based on the above anti-Hermitian metasurface color absorber, we now designed a sub-wavelength pixelated color image sensor in the visible wavelength, collaborating with Samsung device design and fabrication team. In our previous design, the metasurface is simply composed of silicon nano-cylinders in air or on top of silica substrate. In real applications, the structure needs to be integrated with photo-detection device in order to read out the absorption magnitude. The device we designed consists axial p-i-n silicon cylinders in between top and bottom electrodes (schematics shown in Fig. 2.3.1 (a)), and the absorption inside of the silicon cylinders will be converted into photo-voltage and read out from the electrodes. Our optimized design can detect light at red, orange and green colors respectively (Fig. 3b and c), and has pixel size as small as 220 nm.

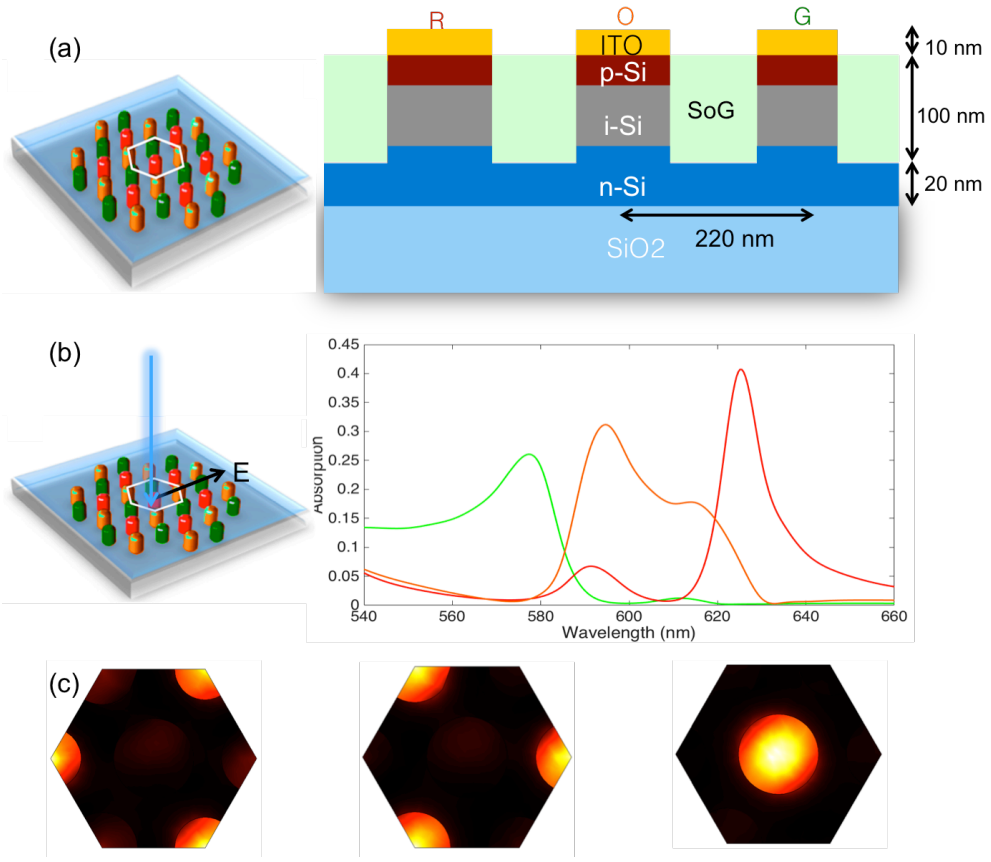


**Figure 2.3.1.** Sub-wavelength pixelated color image sensor based on anti-Hermitian metasurface. (a) Schematics of the design. Axial p-i-n silicon cylinders can be synthesized and transferred to p-type silicon substrate. Spin-on-glass is filled in between the silicon cylinders and a thin layer of ITO is sputtered on top. The cylinders have three different diameters: 136 nm, 122 nm and 104 nm, and can selectively absorb light at red, orange and green color, respectively. (b) Simulated

absorption spectra of three kinds of cylinders in the designed structure. Normal incidence is considered, the polarization of the electric field is as noted in the picture. (c) Electromagnetic field density inside of a structure unit cell (top view), when exited at 570 nm (green), 600 nm (orange) and 630 nm (red), respectively.

We also did full simulation to characterize the dependence of the device's performance on the polarization and angle of the incident light. We found that for normal incidence, the absorption spectrum presents a very good isotropic behavior and doesn't depend on the incident light polarization (Fig. 2.3.2 (a)). When the incidence is angled, the absorption spectrum is different for TE mode incidence (electric field parallel to the metasurface) and TM mode incidence (magnetic field parallel to the metasurface). For TE mode incidence, the color image sensor can accept a large incident angle up to +/- 30° and still has acceptable color sorting ability (Fig. 2.3.2 (b)). For TM mode incidence, however, the device can only tolerate +/- 5° incident angle with current design. This is because when the incident electric field has a component perpendicular to the metasurface, the optical modes that are excited become different, which leads to a big change in their coupling coefficient.

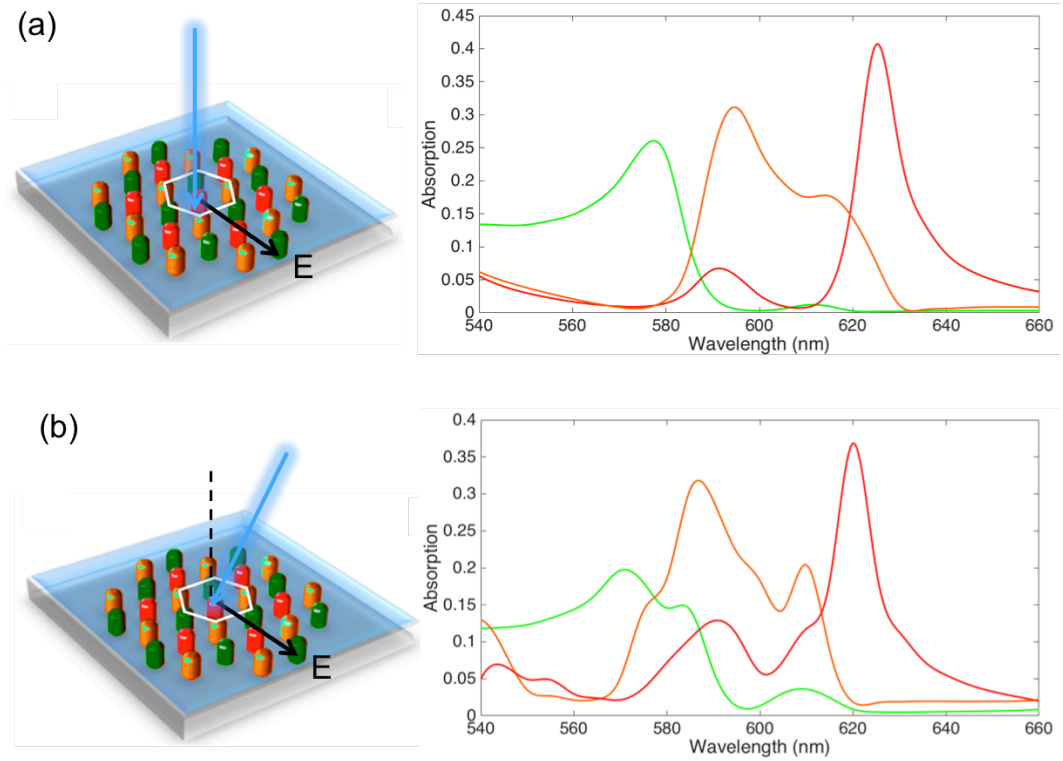


**Figure 2.3.2** Dependence of the device's performance on incident angle and polarization. (a) Simulated absorption spectra inside three kinds of cylinders under normal incidence but a different polarization from that in Fig. 2.3.1. It can be clearly seen that the spectra don't change. The device shows no polarization dependence at normal incidence. (b) Simulated absorption spectrum inside three kinds of cylinders under TE excitation at 30° incident angle. There is some crosstalk between different colors but still presents acceptable color sorting ability.

In the real device, N-type Si is in contact with top ITO electrode, which is connected to an Au pad (top pad). P-type Si acts as an electrical common ground and is connected to the other Au pad (bottom pad), see Fig 2.3.3. To reduce the fabrication and measurement difficulty, in each device, one of the three types of cylinders in a 60 μm × 60 μm square region are electrically connected and grouped into a single electrical readout.

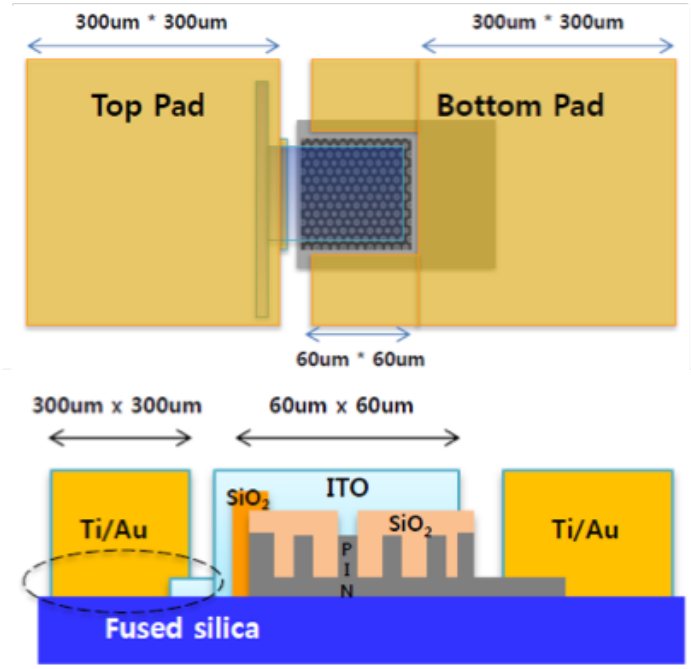


**Figure 2.3.3** Top and side view of the real device.

In the fabrication of the real device, there are inevitable fabrication errors in the cylinders' sizes, shapes and alignments. The fabricated cylinders have round corners at the bottoms, the diameters and alignment of the cylinders have below +/- 5 nm errors, and the thickness of the silicon substrate layers have around +/- 5 nm error. We did simulations according to these situations to determine how they affect the performance of the device. The results show that under all these errors, the couplings are still very close to anti-Hermitian (imaginary part of the coupling much larger than the real part), so that the device would still function well. The main effect caused by these errors is that there can be an up to 6 nm shift in the absorbers' central wavelength.

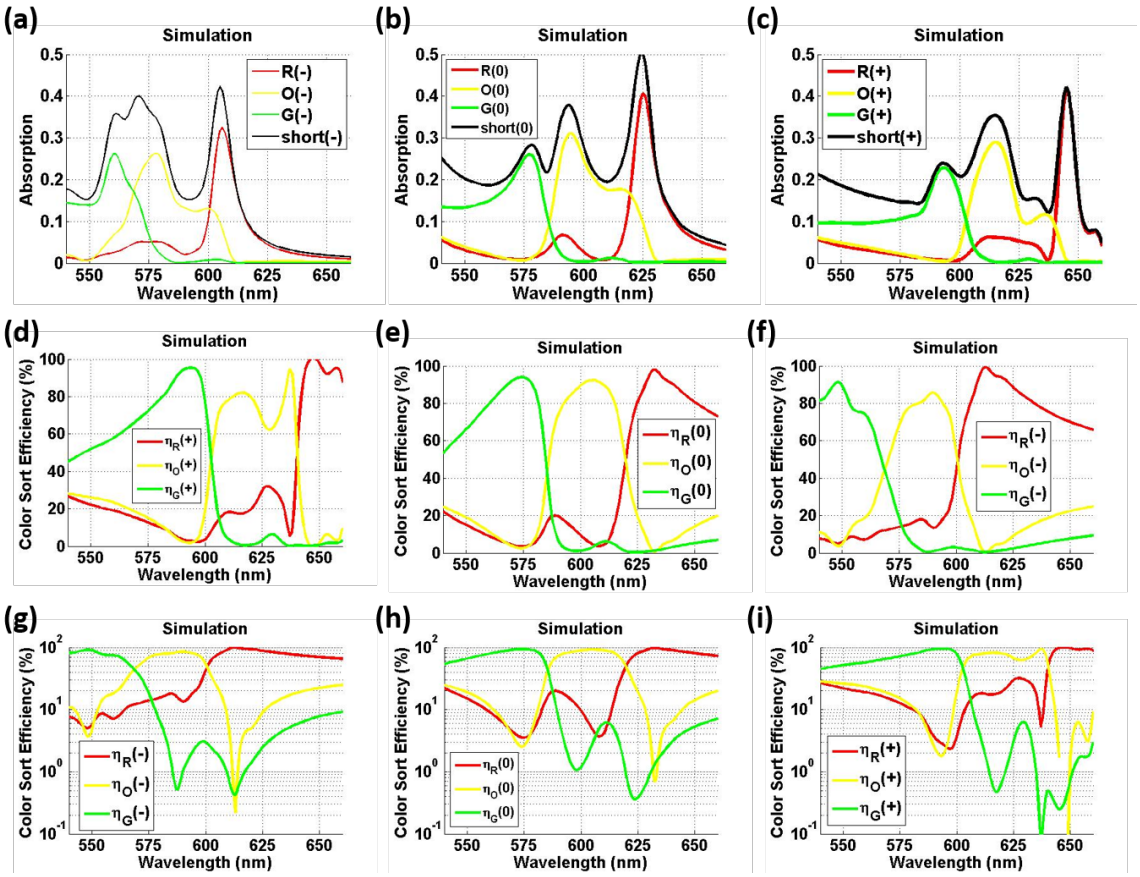


**Figure 2.3.4 Simulation of metasurface with varying diameter nanocylinders.** (a-c) Absorption spectra in the three color channels, for (a) small (all cylinder diameters are 5 nm smaller than the design), (b) standard, and (c) larger (all cylinder diameters are 5 nm larger than the design) diameter nanocylinders, with each array designed for AH coupling. (d-e) Corresponding color-sorting efficiency on linear (d-e) and logarithmic (g-i) scales.

## 2.3.2 Device fabrication

### 1. Vertical shallow junction of PIN poly Si

It is challenging to put vertically P-I-N Si into a 130nm thickness. PIN poly-Si prepared in this study is laminated p-type Si, intrinsic Si and n-type Si with thickness of 50~70nm, 30~70nm and 10~30nm, respectively. Poly-Si deposition and ion implantation are applied to forming vertical PIN junction as a mass productive method. Thermal diffusion of boron dopants is used to prevent native oxide at the interface between p-type Si and intrinsic Si. Boron ions are implanted on the surface, followed by the deposition of the poly-Si layer. Through rapid thermal processing (RTP) at 1000°C, boron dopants diffuse into poly-Si thin film and they are activated as acceptors for p-type Si. Such p-type Si depth is determined by RTP durations, i.e., 10seconds and 30seconds (10s+20s) durations correspond to 50nm and 70nm depth.

N-type Si is formed by implanting arsenic ions directly on top of poly-Si layer. The penetration depth of arsenic elements depends on the thickness of capping layer and ion implantation energy. Before arsenic ion implanting, $SiO_2$ is coated on poly-Si. The penetration depth of arsenic elements depends on the thickness of capping layer and ion implantation energy. The thickness of n-type Si varies by controlling implantation energies in this experiments, as $SiO_2$ is fixed 50nm-thick. The diffusion depths of n-type dopants (phosphorous, arsenic) into poly-Si are compared, keeping implantation energy of 3keV and RTP duration of 10seconds at 1000°C. Figure 2.3.5 (e) shows that phosphorous ions, atomic weight of 30.97, diffuse into all thickness ranges of 130nm, analyzed by secondary ion mass spectroscopy (SIMS). However, heavier ions of arsenic, atomic weight of 74.92, penetrate into 10~30nm depth at implantation energies of 3~10keV.

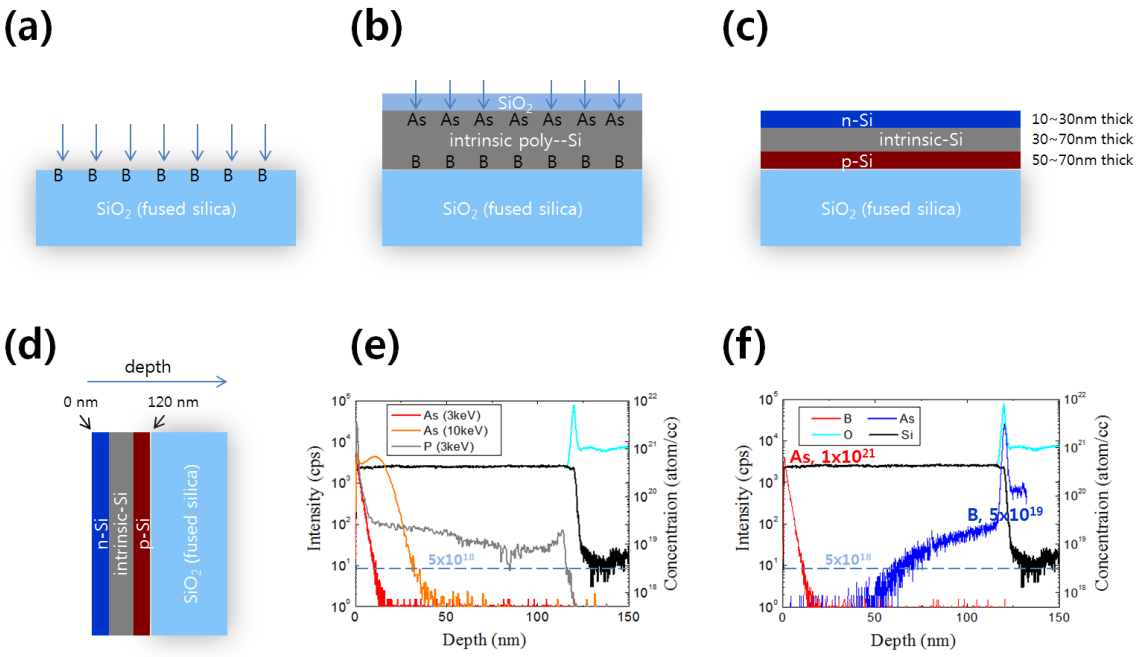

**Figure 2.3.5** Vertical shallow junction of PIN poly Si. (a) Boron ion implantation on fused silica substrate, implantation energy of 3keV, dose of $2x10^{16}cm^{-2}$. (b) 130nm-thick poly-Si + 50nm-thick $SiO_2$ coating + arsenic ions implantation; energy of 3~10keV, dose of $1x10^{16}cm^{-2}$. (c) PIN Si formation by RTP activation for 10seconds at 1000°C. $SiO_2$ capping layer is removed. (d) Schematic illustration of PIN Si. (e) The diffusion depths of n-type dopants, phosphorous and arsenic, into poly-Si, analyzed by secondary ion mass spectroscopy (SIMS). (f) Depth profile of PIN Si, having the thickness of 10nm, 50nm, 70nm for n-type, intrinsic, p-type Si respectively, analyzed by SIMS.

Modifying p-type and n-type Si depths by controlling implantation energy and RTP duration, various thickness of intrinsic Si (30~70nm) can be fabricated in the constraint of 130nm-thick poly-Si as shown in Table 2.3.1. N-type Si has arsenic concentration of $1x10^{21}$ atoms/cc as donors, which is 20 times higher than boron concentration of $5x10^{19}$ atoms/cc as acceptors in p-type Si. For balancing charge carrier concentration, p-type Si (50~70nm) is designed thicker than n-type Si (10 ~ 30nm). Figure 2.3.5 (f) shows the dopant profiles of SIMS analysis of "i-Si 30" in Table 1, having the thickness of 10nm, 50nm, 70nm for n-type, intrinsic, p-type Si respectively.

| Sample | Si thickness | | | Arsenic, implantation | Boron, RTP duration | Substrate |
|---|---|---|---|---|---|---|
| | N-type Si | Intrinsic Si | P-type Si | | | |
| i-Si 30 | 30nm | 30nm | 70nm | 10keV | 30 seconds | Fused silica |
| i-Si 50 | 10nm | 50nm | 70nm | 3keV | 30 seconds | Fused silica |
| i-Si 70 | 10nm | 70nm | 50nm | 3keV | 10 seconds | Fused silica |

**Table 2.3.1** Fabrication parameters and results of the thin PIN junction.

## 2. Nanoscale structuring of color sorting cylinders

Poly-Si nanostructure with $90^o$ side slope are defined by inductively coupled plasma (ICP) etching. The vertical sidewalls are an important characteristic for realizing nano-cylinders of 100 nm diameter, where $C_4F_8$ gas plays a role in side wall passivation during $SF_6$ plasma etching. The ICP-source and bias power are maximized to intensify the effect of vertical etching, within allowance of the etching rate and the e-beam resist's wearing rate. After nanoscale patterning, a low index material of $SiO_2$ (n ~ 1.45 at 550nm) are filled among Si rods. To fill the gap of 91nm, 50nm-thick $SiO_2$ is deposited in advance by plasma-enhanced chemical vapour deposition (PECVD) with tetraethyl orthosilicate (TEOS) source, and the protrusion edge of $SiO_2$ is removed by physical etching of Ar plasma. Afterward, $SiO_2$ using TEOS source is coated again more than 300nm thickness for keeping planarization and etched back until 30~50nm thickness is left over upper regions of nano-cylinders arrays.

## 3. Sample fabrication

Low pressure chemical vapour deposition (LPCVD) is used to deposit poly-Si on a fused silica substrate under $SiH_4$ flow at 60sccm and a pressure of 150mTorr. A 50nm thick $SiO_2$ is added on the poly-Si layer by PECVD at 250 °C. $SiH_4$ and $N_2O$ gas at flow rates of 20 and 1800sccm respectively, are used for the formation of capping $SiO_2$ thin films. After ion implanting at the energy of 3-10keV, the capping layer removed by etching with an aqueous mixture of hydrofluoric acid and ammonium fluoride (2.35% HF + 17% ($(NH_4)F$ + deionized water). Nano cylinder arrays with diameters of 100nm were defined by an e-beam lithography system (JBX-9500FS, JEOL Co., Japan). A positive e-beam resist (ZEP520A, Zeon, Japan) is spun on a PIN poly-Si film. The resist is developed in a 2.38% tetramethylammonium hydroxide (TMAH) solution. Using the e-beam resist's pattern as an etching block mask, nano rods for anti hermitian coupling principle are realized. High ICP source power of 2000W and a bias of 30W are enhanced in dry etching process. A gas mixture of $C_4F_8$, $SF_6$, and Ar with flow rates of 45, 39, and 10sccm respectively, is used at a chamber pressure of 10mTorr. A conformal $SiO_2$ deposition with $O_2$ and TEOS source is applied to narrow-gap filling, having power of 350W, gas flow rates of 220sccm, pressure of 7Torr and working temperature of 400$^oC$. A RIE etching with Ar plasma is assisted for void-free nano-gap filling, under a flow rate of 60sccm and RF power of 300W and pressure of 10mTorr.

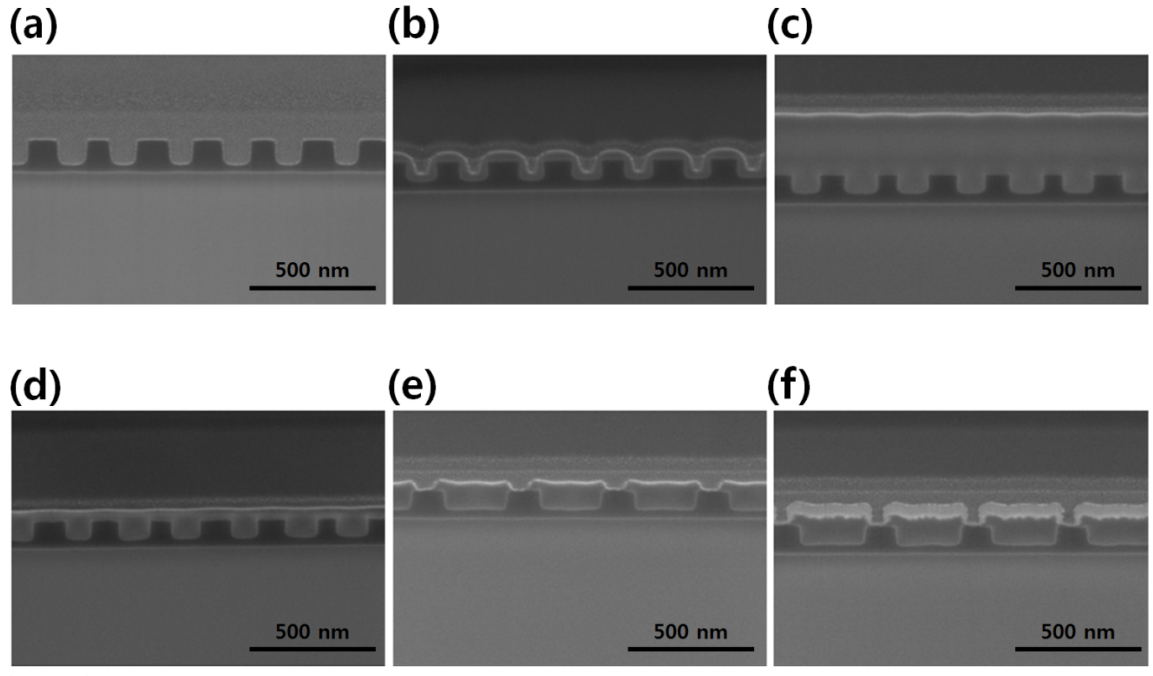


**Figure 2.3.6** Fabrication procedures of the anti-Hermitian color sensor. (a) Nano patterning of PIN poly-Si rods with 90$^o$ side slope. (b) Deposition of 50nm-thick $SiO_2$ and protrusion edge etching with Ar plasma. (c) Void-free nano gap-filling and surface planarization. (d) By etching back, 30~50nm thickness of $SiO_2$ is left over upper regions of nano-cylinder arrays. (e) Nano hole formation **(e)** ITO electrode deposition.

## 2.3.2 Device characterization

To understand the behavior of the fabricated devices, their electrical, optical, and optoelectronic properties were characterized according to standard methods. IV tests confirmed diode behavior; reflection spectroscopy confirmed geometry-dependent, resonant behavior independently of electrical transport properties; and photocurrent spectroscopy confirmed anti-Hermitian optoelectronic color-sorting.

As a reference against which anti-Hermitian (AH) devices could be compared, Test Element Group (TEG) devices were fabricated. The TEG devices use the same materials and process technology as the anti-Hermitian (AH) devices, with the exception that nano-cylinders are not formed. As such the TEG devices are not expected to exhibit large chromatic absorption and the photocurrent should not depend strongly on wavelength. In the following we summarize characterization of contact resistance, dark current, photocurrent, and noise properties of the TEG and AH devices.

### Sample Preparation

Devices were electrically connected to a carrier package with a WestBond wirebonding tool. The carrier package was then inserted into to an electrical breadboard, which also received the leads from the Keithely SourceMeter. An optical image of a wirebonded chip is shown in Fig. X0. Each chip contained 11 test structures, 9 of which were active photodiodes. The two structures at the bottom of the chip (next to the "B" in Fig. 2.3.7) were designed for testing the resistance of the top and bottom contacts. Initially, some degradation of the sample is apparent, likely due to the absorption of water vapor during testing. Later, all devices were held in an inert nitrogen box when not being tested.

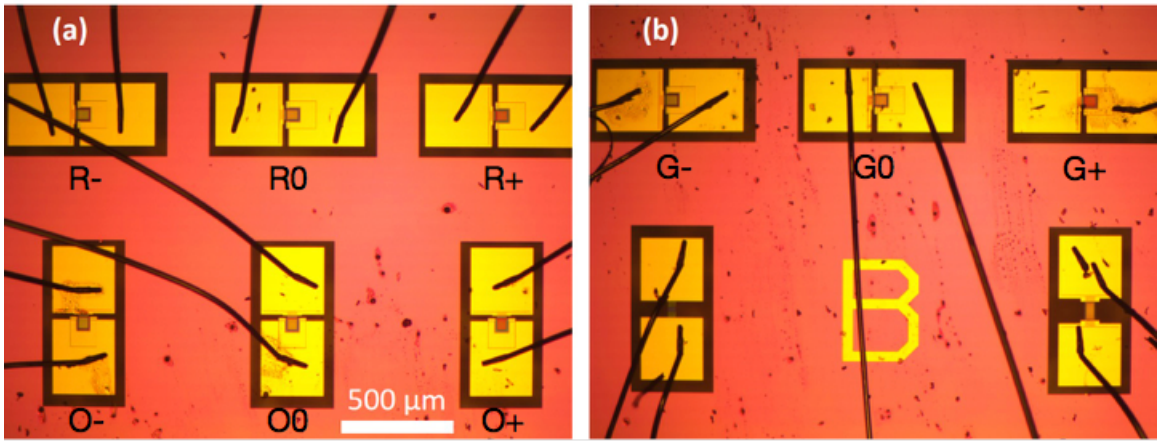


**Figure 2.3.7** Optical image of wire-bonded chip.

Closer visual inspection of photodiode devices with a high NA microscope objectives reveals the effects of nanostructuring. In Figure 2.3.8 (a) and (b), images of the top row of devices are shown using a 10x, 0.25 NA objective and a 100x, 0.60 NA objective,

respectively. Specified nano-cylinder diameters for red, orange, and green sub-pixels in the three devices are (a, d) 126 nm, 112 nm, and 94 nm, (b, e) 136 nm, 122 nm, and 104 nm, (c, f) 146 nm, 132 nm, and 114 nm, respectively. A clear color difference in reflected light is observed as the cylinder dimensions increase. The outer part of the nanostructured region reflects predominantly red and green light for the smallest and largest dimensions, respectively. In the section on photocurrent characterization, we will see that the photocurrent for the device with smallest and largest diameters, indeed preferentially *absorbs* green and red light, respectively.

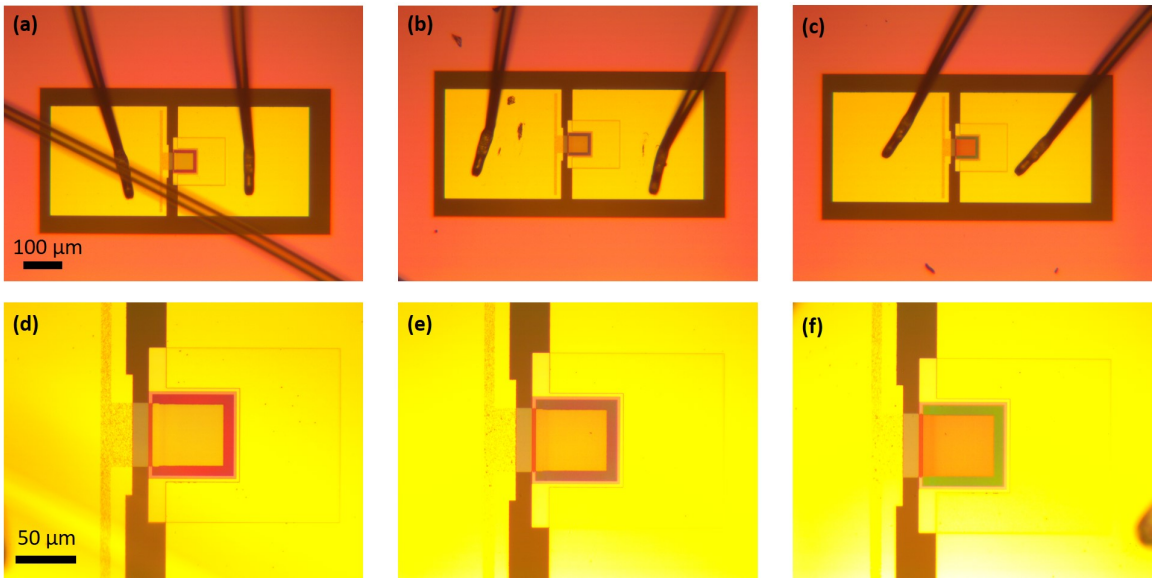


**Figure 2.3.8** Optical images of top row of devices in sample using (a-c) 10x, 0.25 NA and (d-f) 100x, 0.60 NA microscope objectives. Nano-cylinder diameters for red, orange, and green sub-pixels are (a,d) 126 nm, 112 nm, and 94 nm, (b,e) 136 nm, 122 nm, and 104 nm, (c,f) 146 nm, 132 nm, and 114 nm, respectively.

## Contact Characterization

Top and bottom contact resistance of test structures were measured by sweeping the source voltage from -0.5 V to +0.5 V and measuring the current using a Keithley 2401 SourceMeter in 4-wire sensing mode. In this configuration two leads are used for both high voltage and ground. A bias is sourced and current sensed. A LabView virtual instrument file was used to control the SourceMeter and record the data. For each contact, the results of 5 measurements were averaged. The test structures of all nine samples from Batch 2 of fabrication—4 TEG samples and 5 AH samples—were measured. The contact resistance was calculated as the voltage differential divided by the mean of the current differential. As shown in Fig. 2.3.9 (a), the bottom contacts exhibited a fairly uniform resistance on the order of 100 kΩ for both TEG and AH samples. While this value is not small, it is significantly improved from Batch 1 where bottom contact resistance for AH samples was in the 100 MΩ to GΩ range. Measured resistance in the top contacts exhibited greater variation and a larger magnitude, as shown

in Fig. 2.3.9 (b). It is concluded that the top contact structures most likely suffered from design or fabrication errors. Measurement of dark current in the photodiode devices, detailed in the following section indicates that device resistance is limited by contacts with resistance on the order of 100 kΩ. By comparison, the resistance of top contacts in Batch 1 was on the order of 100 Ω.

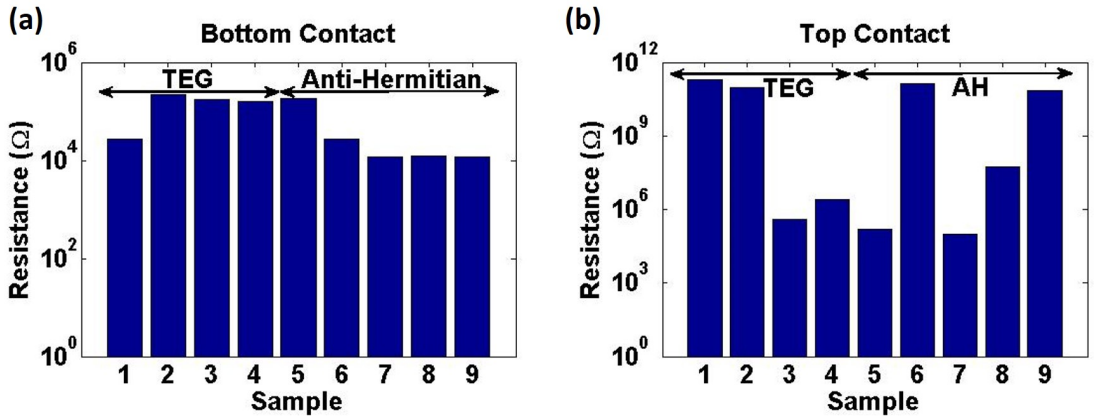


**Figure 2.3.9** Measured resistance in (a) bottom and (b) top contact structures for all TEG and AH samples of Batch 2.

## Photocurrent Characterization

Photocurrent of the TEG and AH devices was measured using the experimental setup illustrated in Fig. 2.3.10. The Chameleon Compact OPO served as a tunable visible light source capable of delivering average power up to 100 mW in a 10 nm spectral bandwidth. The Keithley 2401 served as voltage source and current meter. An oscilloscope is available, along with a chopper, for measuring temporal response of the photodiodes. A lock-in amplifier, in combination with the chopper, can be used to reduce noise, such as $1/f$ noise, during the measurement. However, for the results reported here, we used only the tunable light source and SourceMeter. A microscope enabled us to locate and focus light from the source onto the device under test. The PC serves to control the SourceMeter bias sweep and data collection via a LabView virtual instrument file. In all cases we define the photocurrent, $I_{ph}$, as the difference between the current measured with a non-zero illumination power and the current measured with zero illumination, i.e., $I_{ph}=I(P>0)-I(P=0)$, where $P$ is the illumination power. Throughout all measurements, the spot size of the illumination beam was twice the area of the device under illumination. Therefore the illumination area is a constant in our analysis, through which we can define an irradiance, $E_0$, which is $E_0=P/A_{spot}=P/(2A_{device})=P/(2*0.2\ mm^2)=2.5P\ W\ mm^{-2}$.

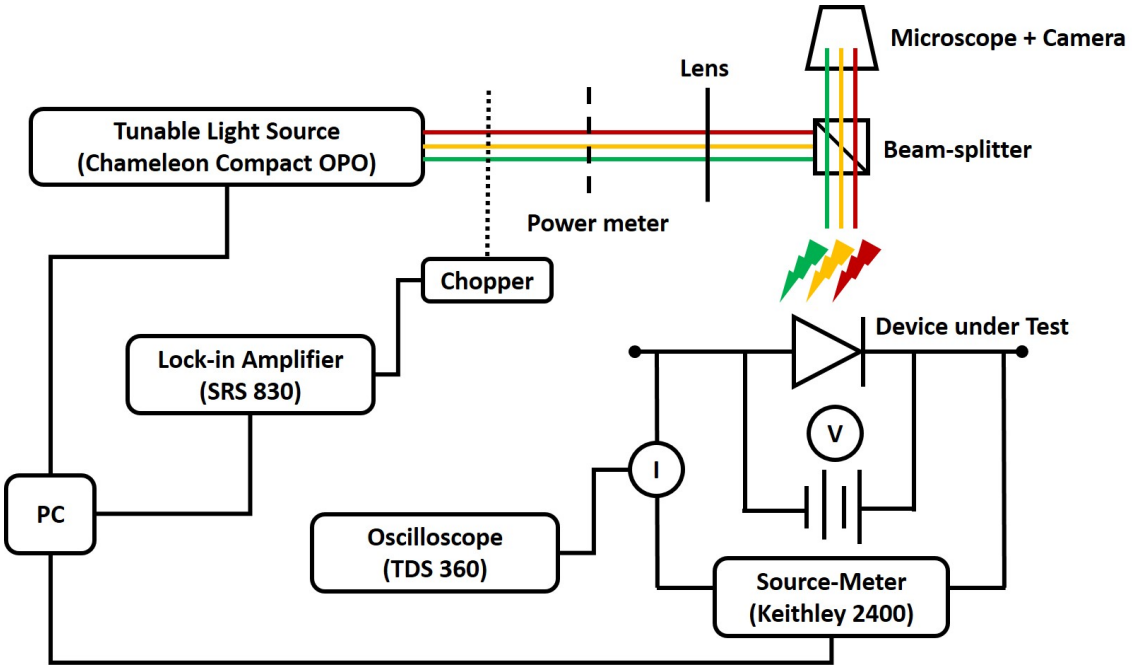


**Figure 2.3.10** Schematic of experimental setup for optoelectronic characterization.

### IV Behavior Characterization

Figure 2.3.11 compares the IV behavior of the AH and control, or test element group (TEG) devices, with illumination power as a parameter. Both sets of devices exhibited diode-behavior with large forward-bias currents and small reverse-bias currents. For a given bias voltage, the control devices yielded slightly higher current due to a broader active area for photon absorption and carrier transport, i.e., less electrical resistance. Both sets of devices exhibited increasing current with illumination power for a fixed reverse bias level, consistent with photodiode behavior.

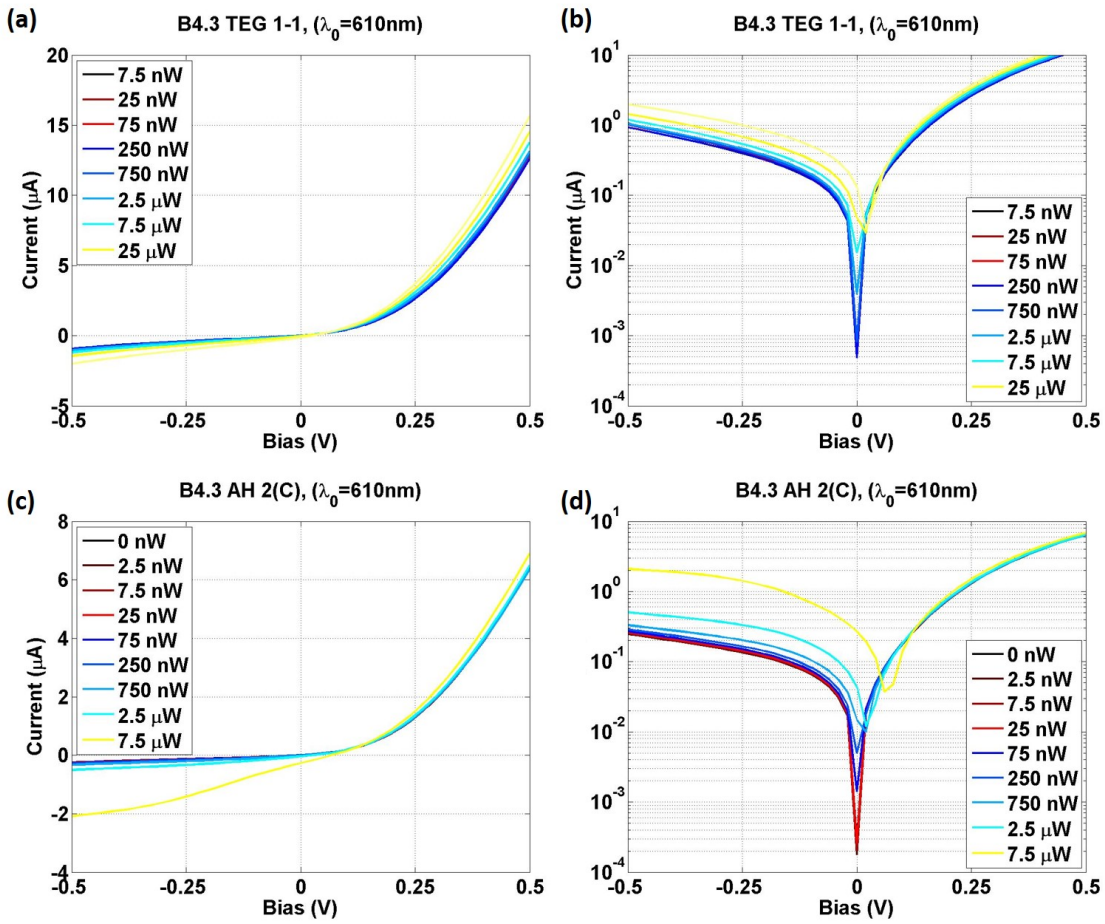


**Figure 2.3.11** Comparison of control test element group (TEG) and AH devices. (a,c) Linear and (b,d) logarithmic IV curves with illumination power as a parameter for representative (a-b) TEG and (c-d) AH devices at an illumination wavelength of 610 nm.

### Photocurrent vs illumination power

Photocurrent as a function of average illumination power is shown in Fig. 2.3.12 (a) for the AH device, at 550 nm and 650 nm illumination wavelength and bias of 0 V and -0.5 V. Figure 2.3.12 (b) shows the ratio of photocurrent to dark current as a function of illumination power under the same conditions. At zero bias, the illumination power was varied more than 4 orders of magnitude, from less than 10 μW to more than 100 mW. At illumination wavelengths of both 550 nm and 650 nm, the photocurrent increases linearly with illumination power with 40 dB of dynamic range, from 10 μW to 100 mW, as shown in Fig. 2.3.12 (a). For the same illumination wavelengths, the photocurrent increases at a slower rate with a bias of -0.5 V and the dynamic range of near-linear behavior is only 30 dB. It should be noted reaching 1 kW of average illumination power was not feasible due to the source power limitations. However, this 1 kW power translates to 2.5 kW $mm^{-2}$ average irradiance, which is beyond the expected operating condition of CMOS image sensors. For example, the daylight sun, which may be considered a "bright" source, has

an irradiance of approximately 1 W $m^{-2}$ $nm^{-1}$ at visible wavelengths [], which corresponds to just 100 μW $mm^{-2}$ for a 100 nm bandwidth.

The ratio of photocurrent to dark current for biases of 0 V and -0.5 V and illumination wavelengths of 550 nm and 650 nm is shown in Fig. 2.3.12 (b). Here the advantage of operating at zero bias becomes evident, as the ratio is 3 to 4 orders of magnitude higher compared to reverse bias operation.

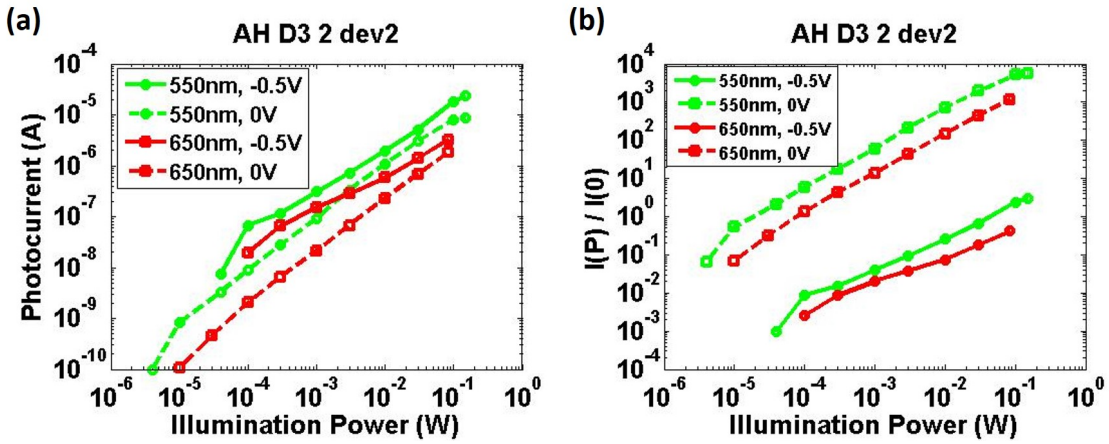


**Figure 2.3.12** Measured (a) photocurrent and (b) photocurrent-to-dark current ratio as a function of illumination power for same AH device at zero bias and reverse bias of -0.5 V and illumination wavelengths of 550 nm and 650 nm.

The photocurrent in the TEG devices is a monotonic function of illumination wavelength for a fixed illumination power. This is shown in Fig. 2.3.13, where the photocurrent of a TEG device is plotted as a function of bias voltage with illumination wavelength as a parameter for a constant illumination power of 10 mW. Two trends are readily observed. Firstly, in both forward and reverse bias, the magnitude of the photocurrent increases monotonically with illumination wavelength. Secondly, in the reverse bias regime, the magnitude of the photocurrent remains relatively flat between -0.2 V and -0.5 V for any particular wavelength. This behavior is desirable and characteristic of commercial photodiodes. The inset to Fig. 2.3.13 (a) shows photocurrent in the same TEG device explicitly as a function of illumination wavelength. Due to the lack of any resonant nanostructures, the photocurrent decreases monotonically with illumination wavelength.

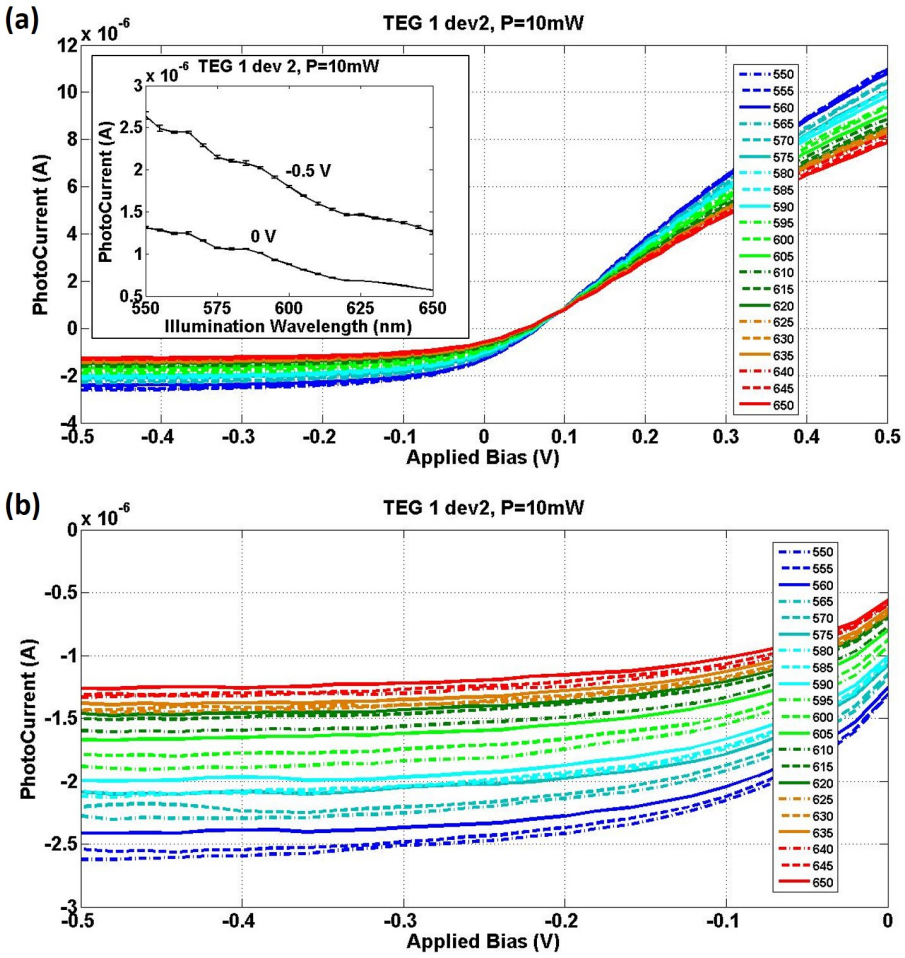


**Figure 2.3.13** Photocurrent in TEG device as a function of bias voltage plotted over bias range of (a) -0.5 V < V < 0.5 V and (b) -0.5 V < V < 0 V with illumination wavelength as a parameter. Inset to (a) shows photocurrent as a function of illumination wavelength for zero bias and bias of -0.5 V for same TEG device. Average illumination power is fixed at 10 mW.

## Reflection spectra

To separate the optical response of the AH devices from their electrical transport properties, reflection spectra were measured of AH devices of varying scale. Figure 2.3.14 (a) compares reflection spectra of AH metasurfaces with increasing scale of nanocylinders, along with the control devices. Whereas the control devices exhibit a single reflection dip, each AH metasurface shows three distinct reflection minima, which are associated with absorption maxima. Figure 2.3.14 (b) shows that the spectral location of the reflection minima is directly related to the resonator diameter of the AH devices, with the reflection minima red-shifting as the diameter increases, consistent with design expectations. From this result, it is evident that the AH behavior can occur over a range of resonator diameters for a given separation distance.

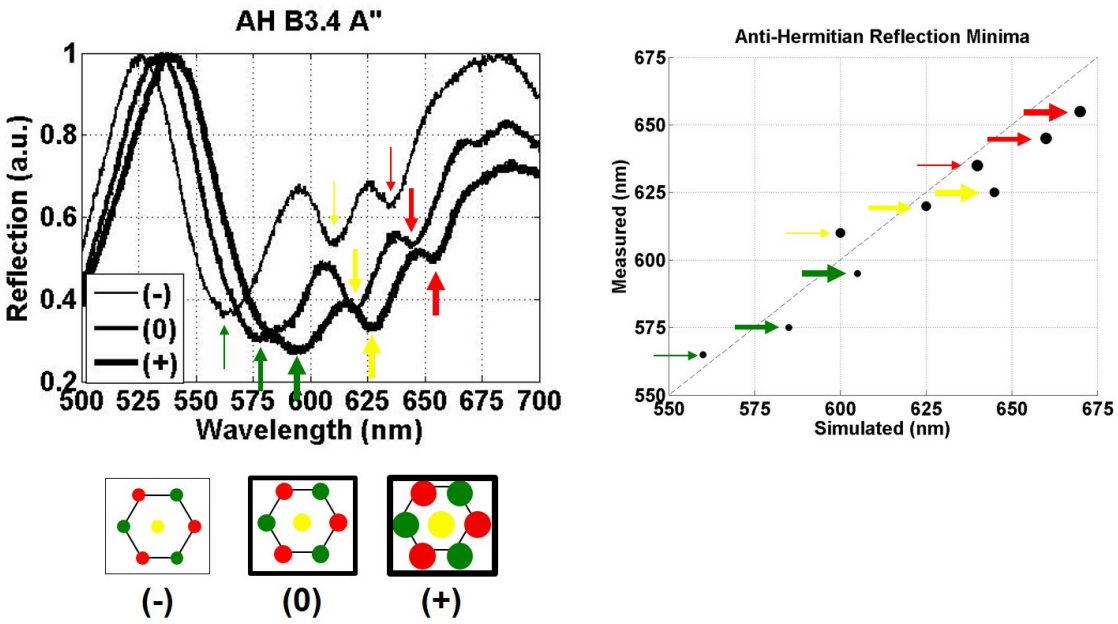


**Figure 2.3.14 Reflection spectra of AH metasurfaces.** (a) Measured reflection as a function of wavelength for three different AH metasurfaces, with nominally (-) small, (0) medium, and (+) large scales. For each metasurface, three reflection minima are clearly observed, associated with green, yellow, and red color channels. Each minima red-shifts as the scale factor increases, consistent with expectations based on numerical design. (b) Measured reflection minima versus simulated reflection minima.

### Three-channel color sorting in anti-Hermitian CMOS color sensors

Photocurrent as a function of illumination wavelength is shown in Fig. 2.3.15 for the ant-Hermitian device. The three color channels show strong chromatic electrical readouts at distinct wavelengths. The spectral locations of the peak photocurrent are in close agreement with our design. Through numerical simulation, green, orange, and red absorption was predicted to peak at 570 nm, 600 nm, and 630 nm. Experimentally, we observe resonant absorption at 565 nm, 590 nm, and 615 nm. The sharpness of the resonances may be quantified through the quality factor, defined as $Q=\lambda_{peak}/\Delta\lambda_{FWHM}$, where $\lambda_{peak}$ and $\Delta\lambda_{FWHM}$ are the wavelength at peak photocurrent and full-width-half-max of the resonance. Experimentally, we measured $Q$ factors ranging from 34 to 42, whereas simulations predict $Q$ factors in the range of 28 to 70. Note that in the figures, G(-), Y(-) and R(-) are devices that were fabricated with diameters intended to be 10 nm smaller than designed. But due to inevitable fabrication errors, SEM images show that these devices have actual cylinder diameters closest to our design.

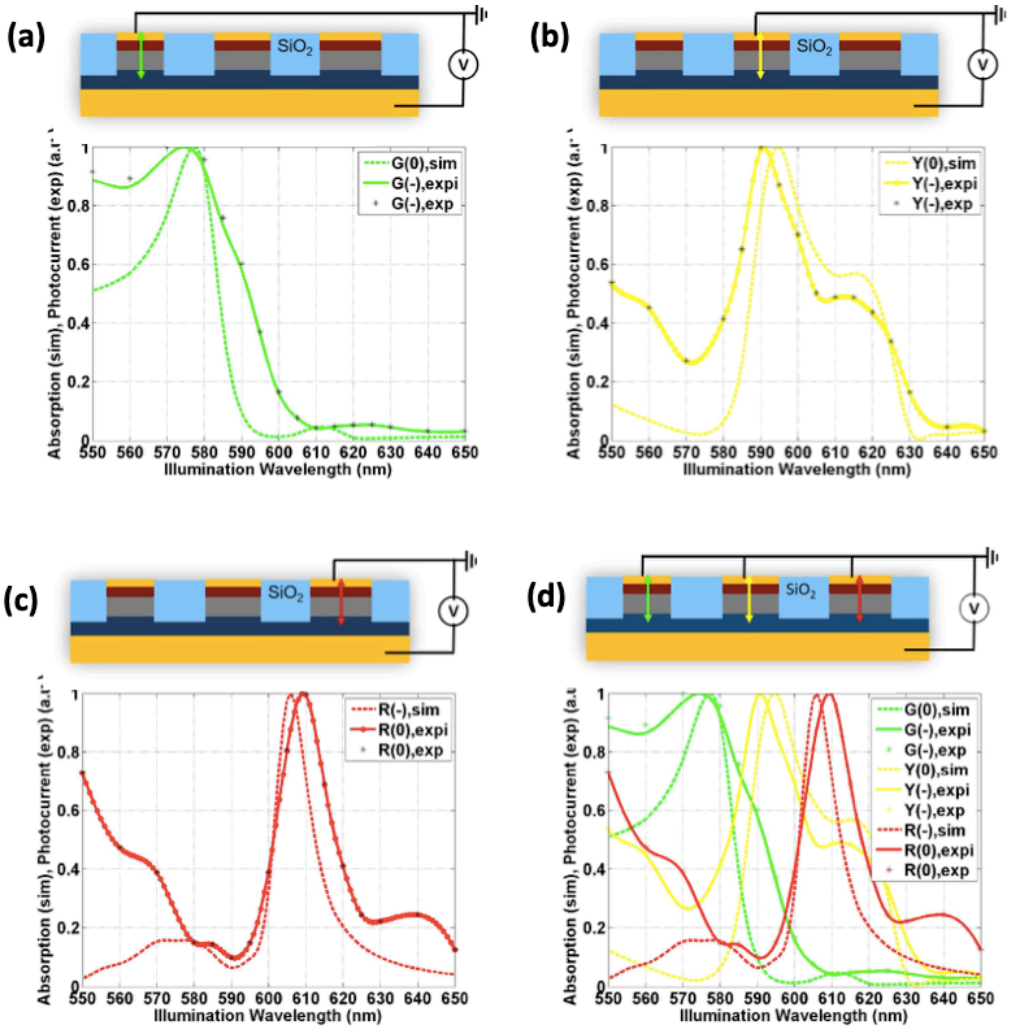


**Figure 2.3.15** Experimental and simulated three-channel color-sorting in anti-Hermitian PIN Si metasurface. Experimental photocurrent (solid curves) and simulated absorption (dashed curves) spectra of the AH PIN Si metasurface when electrical connection is made to (a) green, (b) yellow, and (c) red color channels. For clarity, all curves are normalized to their peak values. (d) Combined photocurrent and absorption spectra of all three channels.

### Responsivity measurement

The responsivity of a photodiode is the ratio of generated photocurrent and incident optical power determined in the linear region of response. It describes the photodiode's ability to convert light into electrons, and is one of the key parameters when characterizing a photodiode's performance. In Fig. 2.3.16 (a), we plot the spectral responsivity of the three color channels in the anti-Hermitian device, operating at a negative bias of -0.5 V. The peak responsivities of the green, yellow and red colors are 0.26 A/W, 0.31 A/W and 0.36 A/W, respectively. These correspond to quantum efficiencies ranging from 0.54 – 0.71.

Photocurrent as a function of bias and illumination power is shown in Fig. 2.3.16 (b) for the red device at a 630 nm illumination wavelength. It can be seen that the photocurrent increases linearly with illumination power in the measured range, and increases with higher negative bias. The large dark current is likely to occur through the poly silicon nano-cylinders, and replacing thin poly silicon by single crystalline silicon using wafer bonding process may potential reduces the dark current, but will hugely increases fabrication time and complexity.

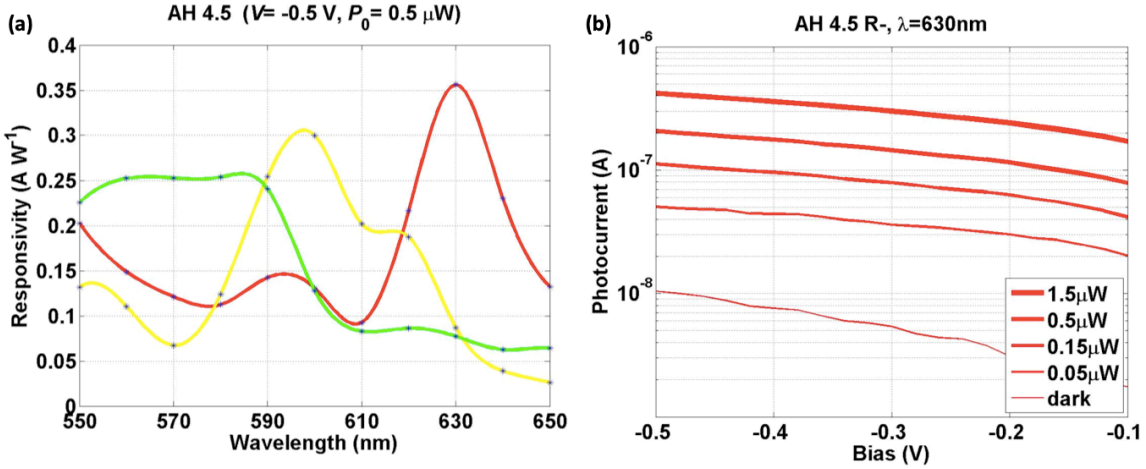


**Figure 2.3.16** Performance characteristics of CMOS color sensors based on anti-Hermitian metasurfaces. (d) Responsivity spectra measured at bias of -0.5 V. (b) Measured photocurrent at illumination wavelength of 630 nm as a function of bias voltage with illumination power as a parameter.

Overall we were able to demonstrate three color sorting in the visible regime from our anti-Hermitian CMOS color sensor. The device performance is independent to the polarization of normally-incident light. The quantum yield is comparable to commercial photodetectors, with a responsivity around 0.3 A/W.

### Responsivity v.s. p-i-n layers thickness

In each batch, the total thickness of the p-i-n junction remains to be the same (130 nm), but the individual thickness of p-i-n layers can be different. The layer thicknesses of batch 4.1, 4.4 and 4.5 are listed below in table 2.3.2.

| Batch | Thickness (nm) | | |
|---|---|---|---|
| | n-Si | i-Si | p-Si |
| **4.1** | 30 | 40 | 60 |
| **4.4** | 5 | 65 | 60 |
| **4.5** | 5 | 85 | 40 |

**Table 2.3.2** p-i-n layer thickness of three different batches.

For each batch, we measured the photocurrent as a function of bias for device R- under a constant illumination wavelength of 630 nm (absorption peak wavelength), plotted in Fig. 2.3.17. It can be seen that batch 4.5 has the largest responsivity, which is one order higher than 4.1 and 4.4. This can partly be explained by that batch 4.5 has the largest intrinsic region, and thus have a higher photon absorption.

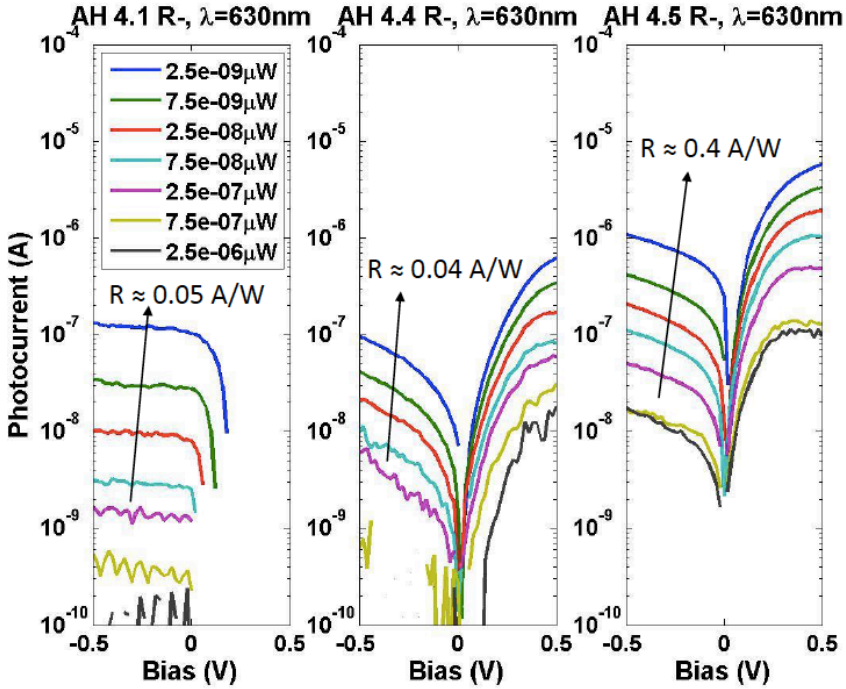


**Figure 2.3.3.17** Photocurrent as a function of bias under different illumination power for R- device in batch 4.1, 4.4 and 4.5. The illumination wavelength is fixed at 630 nm, which is the absorption peak position for device R-.

## 2.4 Summary

As the demand for smaller pixel size and higher resolution in imaging and display technologies increases, the need for tools to circumvent once-thought fundamental limits increases. Conventional color filters rely on the chromatic absorption in organic dyes. However, due to the low absorption index, organic dyes cannot be made thinner than a few hundred nanometers, which hindered the realization of small pixel sizes due to light propagation and diffraction. Also, the traditional filtering schemes are inherently inefficient due to the rejection of light.

Here, we demonstrated subwavelength scale pixels based on anti-Hermitian that circumvent the constraints of conventional pixels. Spectral filtering is achieved through structural color rather than transmissive filters, namely through Mie resonances in silicon nanoresonators, with carefully controlled separation distances, leading to simultaneously high color purity and quantum efficiency. Our metasurface pixel array is the first demonstration of anti-Hermitian coupling in a CMOS compatible platform, sorting three colors over a 100 nm bandwidth in the visible regime, independently of the polarization of normally-incident light. The two-dimensional, 60 μm by 60 μm array, contains over 28,000 pixels, each with an area less than half a squared wavelength of the absorbed light. Furthermore, the quantum yield is comparable to commercial photodetectors, with responsivity around 0.3 A/W. Our demonstration lays the foundation for the realization of CMOS color and image sensors with revolutionarily small pixel sizes.

## References


[1] Meinzer, Nina, William L. Barnes, and Ian R. Hooper. "Plasmonic meta-atoms and metasurfaces." Nature Photonics8.12 (2014): 889.

[2] Yu, Nanfang, and Federico Capasso. "Flat optics with designer metasurfaces." Nature materials 13.2 (2014): 139.

[3] Zhang, Shuang, et al. "Anti-Hermitian plasmon coupling of an array of gold thin-film antennas for controlling light at the nanoscale." Physical Review Letters 109.19 (2012): 193902.

[4] Okołowicz, Jacek, Marek Płoszajczak, and Ingrid Rotter. "Dynamics of quantum systems embedded in a continuum." Physics Reports 374.4 (2003): 271-383.

[5] Makhmetov, G. E., et al. "Interaction between overlapping quasi-stationary states: He Levels in Front of an Aluminium Surface." EPL (Europhysics Letters) 27.3 (1994): 247.

[6] Alhassid, Yoram. "The statistical theory of quantum dots." Reviews of Modern Physics 72.4 (2000): 895.

[7] Liu, Na, et al. "Plasmonic analogue of electromagnetically induced transparency at the Drude damping limit." Nature Materials 8.9 (2009): 758-762.

[8] Zhang, Shuang, et al. "Plasmon-induced transparency in metamaterials." Physical Review Letters 101.4 (2008): 047401.

[9] P. K. Jha, M. Mrejen, J. Kim, C. Wu, Y. Wang, X. Yin, and X. Zhang, "Interacting dark resonances with plasmonic meta-molecules", Appl. Phys. Lett. 105 (2014): 111109

[10] Jahani, Saman, and Zubin Jacob. "All-dielectric metamaterials." Nature nanotechnology 11.1 (2016): 23.

[11] Genevet, Patrice, et al. "Recent advances in planar optics: from plasmonic to dielectric metasurfaces." Optica 4.1 (2017): 139-152.

[12] Pyayt, Anna L., Gary K. Starkweather, and Michael J. Sinclair. "A high-efficiency display based on a telescopic pixel design." Nature Photonics 2.8 (2008): 492.

[13] Hsu, Tzu-Hsuan, et al. "Light guide for pixel crosstalk improvement in deep submicron CMOS image sensor." IEEE electron device letters 25.1 (2004): 22-24.

[14] Rajasekharan, Ranjith, et al. "Filling schemes at submicron scale: Development of submicron sized plasmonic colour filters." Scientific reports 4 (2014): 6435.

[15] Yokogawa, Sozo, Stanley P. Burgos, and Harry A. Atwater. "Plasmonic color filters for CMOS image sensor applications." Nano Letters 12.8 (2012): 4349-4354.

[16] Xu, Ting, et al. "Plasmonic nanoresonators for high-resolution colour filtering and spectral imaging." Nature communications1 (2010): 59.

[17] Laux, Eric, et al. "Plasmonic photon sorters for spectral and polarimetric imaging." Nature Photonics 2.3 (2008): 161.

[18] Park, Hyunsung, et al. "Filter-free image sensor pixels comprising silicon nanowires with selective color absorption." Nano letters 14.4 (2014): 1804-1809.

[19] Le Perchec, J., Y. Desieres, and R. Espiau de Lamaestre. "Plasmon-based photosensors comprising a very thin semiconducting region." Applied Physics Letters 94.18 (2009): 181104.

[20] Zhao, Qian, et al. "Mie resonance-based dielectric metamaterials." Materials today 12.12 (2009): 60-69.
[21] Stratton, J. A. “Electromagnetic Theory”. New York: McGraw-Hill (1941).
[22] Van de Groep, J., and A. Polman. "Designing dielectric resonators on substrates: Combining magnetic and electric resonances." Optics express 21.22 (2013): 26285-26302.
[23] Fu, Yuan Hsing, et al. "Directional visible light scattering by silicon nanoparticles." Nature communications 4 (2013): 1527.

# Chapter 3

# Manipulating Emitter Properties with Quantum Metasurface

Coherent superposition of states (i.e., quantum coherence) is a fundamental feature of quantum mechanics, marking its departure from the classical realm [1]. For elementary particles, such as atoms, ions, and photons, quantum coherence is an essential ingredient for a plethora of phenomena in quantum optics [2], quantum information science [3], and condensed matter physics [4]. In semiconductors, excitons (Coulomb-bound electron-hole pairs), which are the fundamental quasiparticles, also exhibit coherence. Excitonic coherence plays a crucial role in quantum dots [5], quantum-well structures [6], and light harvesting complexes [7]. Recently, atomically thin transition metal dichalcogenides (TMDCs) of the form MX2 have emerged as a new class of semiconductor materials for both fundamental physics exploration in two-dimensional systems and device applications [8–10].

Here we theoretically demonstrate spontaneous generation of quantum coherence in valley excitons in atomically thin transition metal dichalcogenides (TMDCs). We achieve this by manipulating the vacuum field in the vicinity of the monolayer TMDC with a designed polarization-dependent phase gradient metasurface. The phase gradient metasurface consists of gap plasmon resonators, and can locally tailor the wavefront with geometric phases. Acting as a focusing mirror with different phase shift for x and y polarizations, the metasurface is able to induce an anisotropic decay rate for in-plane excitonic dipoles. The spontaneous exciton valley coherence in TMDC monolayers opens a new paradigm in two-dimensional materials, exploiting quantum interference effects for optoelectronic applications and novel valleytronic devices.

## 3.1 Phase Gradient Metasurface

Conventional phase control devices, such as lenses, rely on the accumulated propagation phase in medium, so they are usually quite bulky. On the contrary, phase gradient metasurface allows abrupt phase control over a subwavelength distance. Moreover, other than phase, local polarization and amplitude can also be controlled, enabling full wavefront control at the subwavelength scale. Metasurface consists of many small unit cells, so called 'meta-atoms'. Each meta-atom is deep subwavelength in size, and can act as a local scatterer when light is incident upon it. The phase and polarization of the scattered light can be tailored by varying the shape of the meta-atoms. By designing each meta-atoms specifically, we can imprint any arbitrary phase and polarization profile across the metasurface.

### 3.1.1 Phase control from resonance

Here we design an anisotropic metasurface that acts as a polarization dependent focusing mirror. For x polarization, the metasurface works as a reflective focusing lens; for y polarization, the metasurface behaves like a regular mirror. The metasurface unit cell consists of a rectangular gold antenna on top of a gold reflection plane, spaced by a layer of magnesium fluoride. The structure supports gap plasmon resonances [11,12], where the electromagnetic field is concentrated in between the top and bottom gold. The local phase control is achieved by controlling the antenna sizes ($L_x$ and $L_y$).

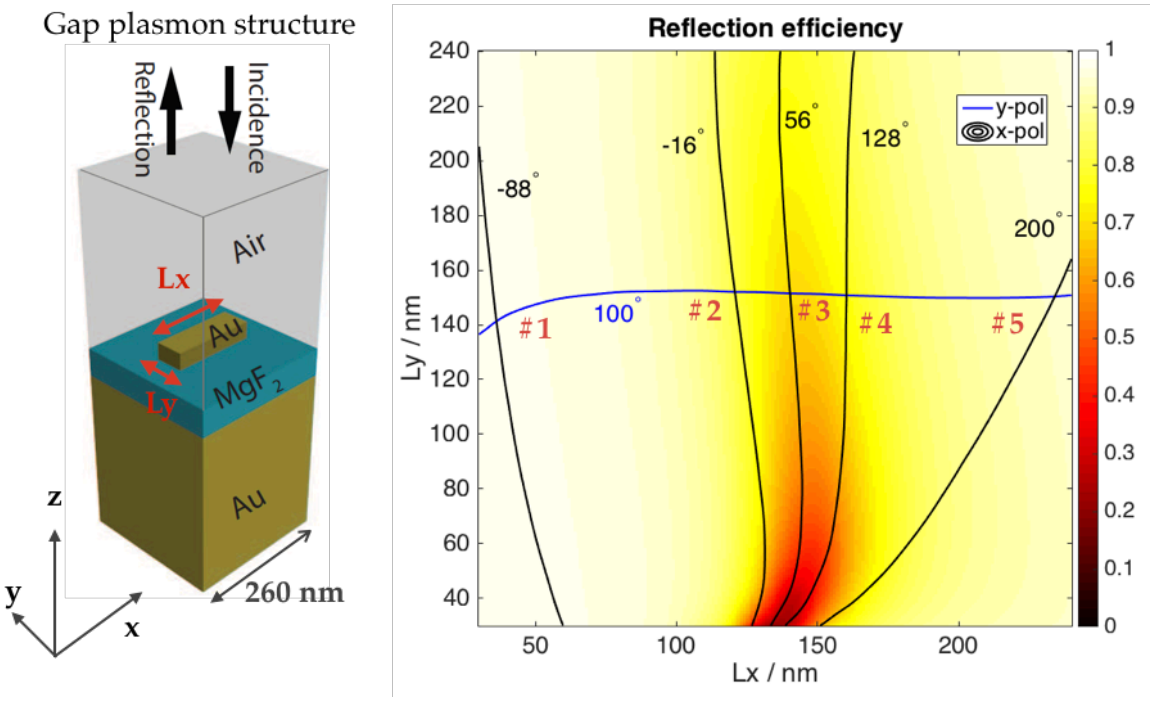

**Figure 3.1.1** Design of metasurface unit cell based on gap plasmon structure. Left: Schematics of a gap plasmon unit cell. Au rectangular nano-antenna is located on top of a Au substrate, spaced by a layer of MgF2. Right: The reflection efficiency and phase contour as a function of the dimension Lx and Ly of the nano-antenna. A gap plasmon resonance appears at around Lx = 140 nm.

When light is incident on the cell, the cell reflects it back with a phase shift. By changing the antenna size ($L_x$ and $L_y$), the phase shift can vary from 0 to almost 2pi. The phase shift for x and y polarization can be independently controlled. The contour lines are the phase shifts induced by the metasurface for x and y polarized incidence, respectively. The vertical lines are for x-pol, and the horizontal is for y-pol. The crossings give us 5 unit cell structures, which provide a constant phase shift for y-pol, and a phase shift that vary across 2pi. The 5 unit cells all have relatively high efficiency, with an average efficiency of above 80%.

We can pattern the 5 unit cells to construct the whole metasurface. For an x-pol dipole above the metasurface, we want the radiation to be focused back to the dipole with a pi phase shift. So the metasurface should provide a wavefront of the form below:

$$\phi(x,y) = 2k_0\sqrt{r^2+d^2} + C\ ,$$

where d is the distance between the dipole and the metasurface.

For the y-pol incidence, the metasurface provides a constant phase shift and acts like a flat mirror. We fabricated the metasurface using electron-beam lithography and lift-off technique, as the SEM image of the fabricated metasurface is shown in Fig. 3.1.2.

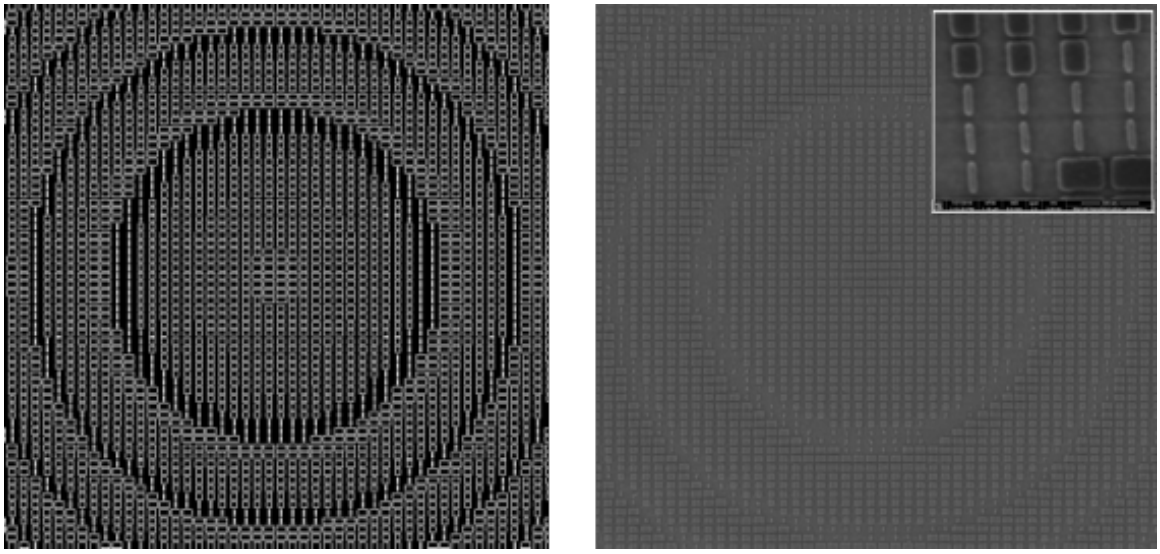

**Figure 3.1.2** Design and fabrication of the metasurface. Left: Top view of the metasurface design. Right: SEM image of the fabricated metasurface. The full metasurface is 50 by 50 micron in size and the images show only the middle part of the metasurface. The focusing distance d is 25 μm, which leads to a large NA of around 0.9.

We characterize the polarization dependent focusing behavior of the fabricated metasurface with the setup shown in Fig. 3.1.3. A laser beam is collimated, and the polarization of light beam is controlled by a half-wave plate and a polarizer. The objective lens in the microscope focuses the light at a distance above the metasurface and illuminate the metasurface. The reflected light is collected and makes an image on the CCD camera. The objective lens we use have an NA of 0.9, which makes sure that the whole metasurface can be illuminated

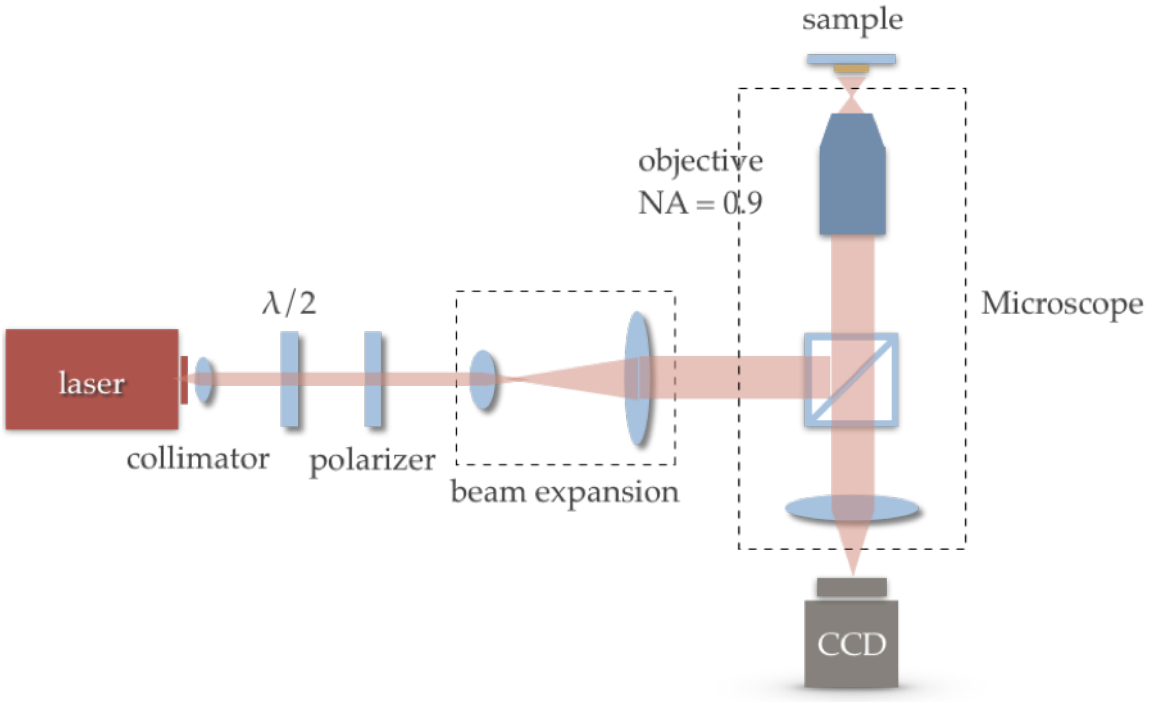


**Figure 3.1.3** Schematics of the experimental setup for metasurface characterization.

The focusing behavior of the metasurface is measured by scanning the position of metasurface on the z direction and imaging the reflected light on the image plane. When the distance of the objective lens and the metasurface equals to the focusing distance, the camera detects a spot for the x polarized light, which shows that the light is reflected back and focused at the focusing distance, while for y polarized light a focus spot does not exist.

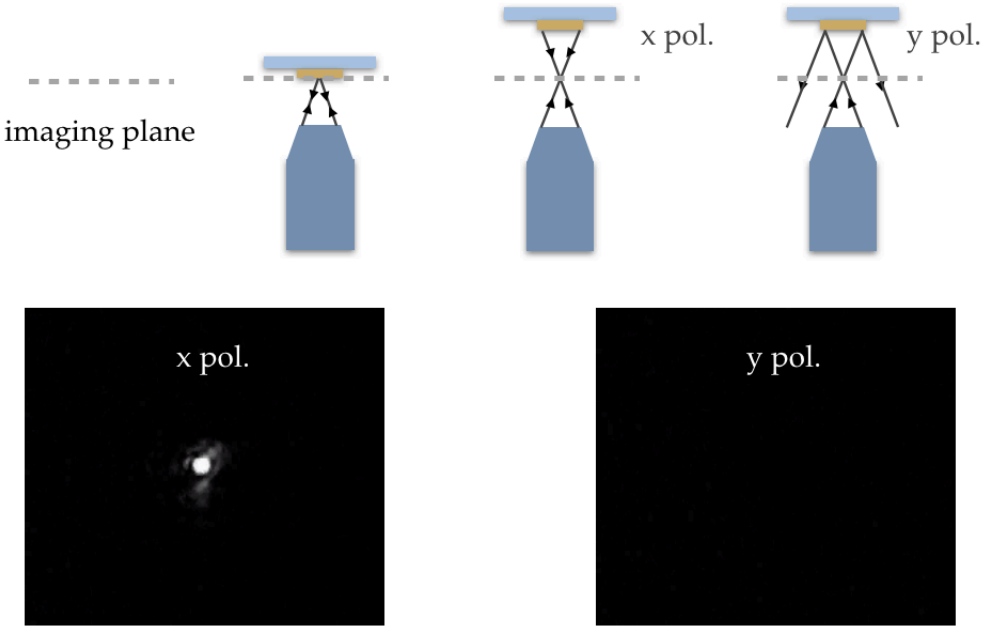


**Figure 3.1.4** Measurement of the metasurface focusing behavior for x and y polarized light. Top: scan the distance between the metasurface and the objective lens. Bottom left: the reflected light is focused for the x polarized light, and not focused for the y polarized light.

The focus spot size from the metasurface is extracted from a Gaussian fit of the focus spot intensity. The reflection efficiency is measured to be around 50% by comparing the integrated intensity of light collected from the reflection of a metasurface and the reflection of a commercial mirror.

## 3.1.2 Phase control with geometric phase

A polarization dependent metasurface can also be designed based on geometric phase. A geometric phase metasurface converts an incident circularly polarized light into a beam of opposite circular polarization, imprinted with a geometric Pancharatnam-Berry phase [13]

$$\phi(x,y) = 2\sigma_{\pm}\theta(x,y).$$

Here, $\sigma_{\pm} = \pm 1$ is the polarization helicity of the incident light corresponding to right and left circularly polarized light, respectively, $x$ and $y$ are the metasurface coordinates, and $\theta(x,y)$ is the on-demand space-variant orientation angle profile of the anisotropic nanoantennas [13-18]. The metasurface we designed can focus both $\sigma+$ and $\sigma-$ light but with different phase shift at the focus spot. Accordingly, the phase profile imprinted at the metasurface is:

$$\phi(x,y) = 2k\sigma_{\pm}\left(\sqrt{x^2+y^2+d^2}-\pi\right).$$

Here, $k = 2\pi/\lambda$ is the wavenumber, $\lambda$ is the working wavelength and $d/2$ is the focusing length of the metasurface. As the phase pickup in geometric phase metasurfaces is set by locally orienting the anisotropic antennas, this on-demand phase profile was realized by arranging the antennas according to the space-variant angle profile.

In order to achieve a highly efficient geometric phase metasurface, an individual antenna is designed to locally mimic a half-wave plate, which fully converts an incident circularly polarized light into a beam of opposite circular polarization. Here, we realized the individual antenna as a gap plasmon resonator nanoantenna consisting of metal-insulator-metal layers that enable high reflectivity by increasing the coupling between the free wave and the fundamental resonator mode. We designed the dimensions of the nanoantenna to locally mimic a half-wave plate for the reflected light, yielding highly efficient reflective GPMs by maximizing the cross-polarization reflectivity for the components flipping the polarization helicity of the incident wave while minimizing the co-polarization reflectivity for the components maintaining the polarization.

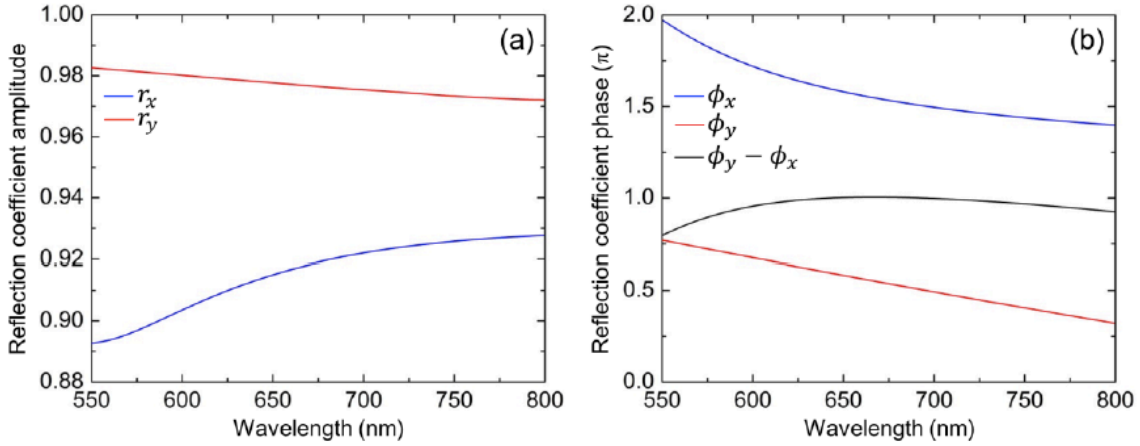


**Figure 3.1.5** Optical response of the individual anisotropic nanoantenna for designing an efficient metasurface. (a) (b) Simulated wavelength-dependent reflection coefficient amplitude and phase, respectively, for $x$- and $y$-polarized light excitations. The width ($x$ dimension) and length ($y$ dimension) of the individual nanorod antenna of the GPM are 200 and 80 nm, respectively, and the thickness is 30 nm. The individual antenna design relies on a gap plasmon resonator nanoantenna with a 30-nm-thick silver nanorod, a 110-nm-thick dielectric (MgF2) spacer layer, and a 130-nm-thick silver layer acting as a back reflector. $r_x$ and $r_y$ are the simulated reflection coefficient amplitudes for $x$- and $y$-polarized light excitations, respectively; $\phi_x$ and $\phi_y$ are the simulated reflection coefficient phases for $x$- and $y$-polarized light excitations, respectively. Over a large bandwidth of ~200 nm, we obtained the desired $\pi$-phase difference between the reflection coefficient phases corresponding to $y$- and $x$-polarized light excitations, such that the individual nanorod antenna locally mimics a half-wave plate for the reflected light. This enables highly efficient reflective GPMs by maximizing the cross-polarization reflectivity for the components

flipping the polarization helicity of the incident wave while minimizing the co-polarization reflectivity for the components maintaining the polarization.

As the individual anisotropic antenna of the GPM, we considered a nanorod in which the width ($x$ dimension) and length ($y$ dimension) are 200 and 80 nm, respectively, and the thickness is 30 nm. The individual antenna design relies on a gap plasmon resonator nanoantenna with a 30-nm-thick silver nanorod, a 110-nm-thick dielectric (MgF2) spacer layer, and a 130-nm-thick silver layer acting as a back reflector. The cross-polarization reflectivity is maximized (~90%) while the co-polarization reflectivity is minimized (~0.1%) over a large bandwidth of ~200 nm. Such a robust response of the cross-polarization and co-polarization reflectivities mainly stems from the $\pi$-phase difference between the reflection coefficient phases corresponding to $y$- and $x$- polarizations of the light excitations.

We used a set of 16 nanoantenna orientations mimicking phase shifters with a $\pi/8$ phase increment to construct the GPM according to the on-demand phase profile. It is worth mentioning that as the continuous phase profile is mimicked by a finite set of nanoantenna phase shifters, the overall cross-polarization reflectivity of the constructed metasurface is given by

$$\eta = \eta_0 \sin^2(\pi N)/(\pi N)^2,$$

where $\eta_0$ is the cross-polarization reflectivity of the individual antenna and $N$ is the number of levels used for the phase discretization []. Therefore, the realization of the desired metasurface with $N$ = 16 yields an overall cross-polarization reflectivity of ~89%, revealing that the phase discretization loss is minor.

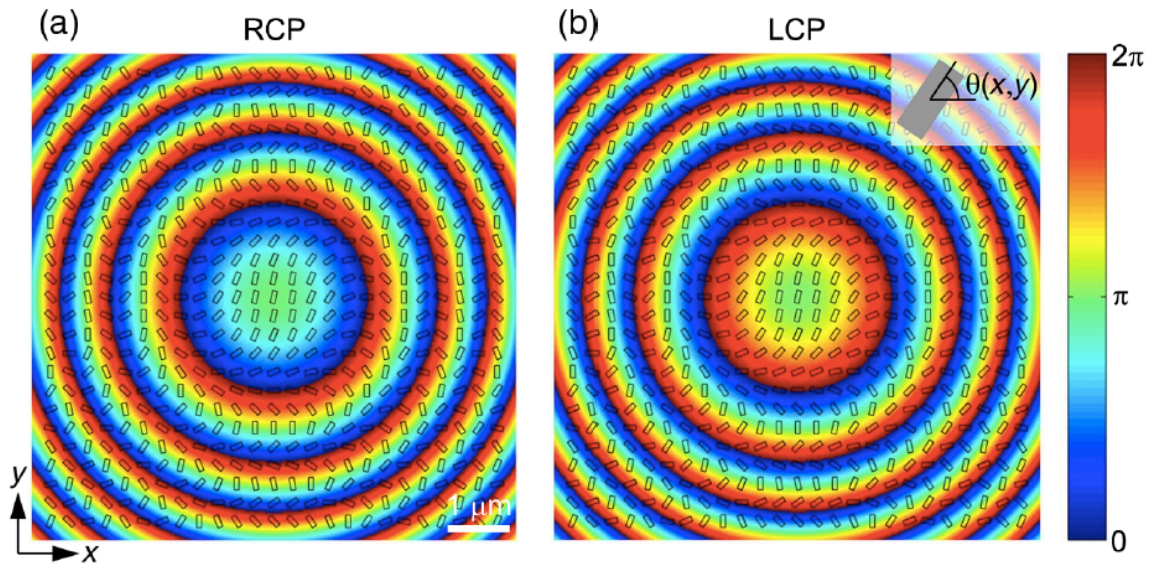


**Figure 3.1.6** Geometric phase-based metasurface for an anisotropic quantum vacuum. The colors represent the phase profiles for molding the incident light with right circular polarization (RCP) and left circular polarization (LCP), respectively, at a free-space wavelength of 670 nm and a

height of the dipole from the metasurface of d = 10 λ. The corresponding metasurface realization, i.e., a nanorod antenna array with space-variant orientations is shown on top. The width (x dimension) and length (y dimension) of each nanorod are 200 and 80 nm, respectively, and the thickness is 30 nm. The individual antenna design relies on a gap plasmon resonator nanoantenna with a 30-nm-thick silver nanorod, a 110-nm-thick dielectric (MgF2) spacer layer, and a 130-nm-thick silver layer acting as a back reflector. We used a set of 16 nanoantenna orientations mimicking phase shifters with a π=8 phase increment.

## 3.2 Quantum Interference in Three-Level Systems

Quantum interference appears in one form or another in almost all quantum mechanics phenomena. In classical theory, interference between lights is from its wave light nature. However, in quantum picture, interference arises from the indistinguishability of photon paths, and is explained by the superposition of probability amplitudes. Interference is not only associated with light, it has been observed in many other material particles such as electrons [19], atoms [20] and BECs [21].

Hong-Ou-Mandel experiment is a classical example of quantum interference [22]. When two identical photons are incident on a beam splitter from two sides, they always come out from the same port. So the photon coincidence on the two detectors is zero. This cannot be explained by a classical view. Quantum entanglement is also closely related to quantum interference effect [23]. In quantum entanglement, a group of particles interact in a way such that their quantum state cannot be described independently.

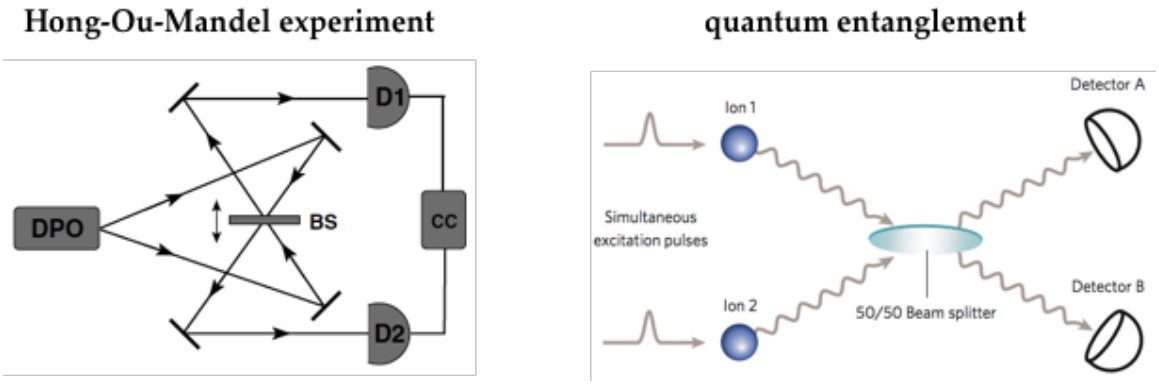


**Figure 3.2.1** Quantum interference effects. Left: Hong-Ou-Mandel experiment. Two identical photons are incident on a beam splitter from two sides, and two detectors at the two output ports measure the photon concurrence. Right: quantum entanglement. The entanglement between two ions are induced by quantum interference at the beamsplitter. (Figure Adapted from ref. [22, 23].)

Quantum interference can also appear between two transitions in a quantum emitter. Consider a single quantum emitter, which has a V-type level structure. And these are the two allowed transitions. Even without external drive, interference can happen between the two transitions since they both couple to vacuum. However, the necessary conditions for the interference is that: first, they should be nearly degenerate, such that the energy spacing Delta is smaller than decay rate. Second, the two transitions should be non-orthogonal to each other in terms of polarization.

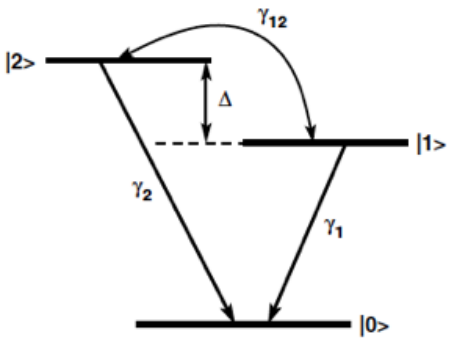


**Figure 3.2.2** A V-type three level system. The two upper states have decay rate $\gamma_1$ and $\gamma_2$ respectively. The energy difference between the upper two states is $\Delta$. When the two transitions are not orthogonal to each other, a cross-damping term $\gamma_{12}$ can be induced.

When the system satisfies these two conditions, the quantum interference induces two new eigenstates -- a symmetric state and a asymmetric state:

$$|s\rangle = \frac{\sqrt{\gamma_1}\,|1\rangle + \sqrt{\gamma_2}\,|2\rangle}{\sqrt{\gamma_1+\gamma_2}}$$
$$|a\rangle = \frac{\sqrt{\gamma_2}\,|1\rangle - \sqrt{\gamma_1}\,|2\rangle}{\sqrt{\gamma_1+\gamma_2}}$$

Then the master equation of the system writes:

$$\dot{\varrho}_{ss} = -\frac{1}{2}(\gamma+\gamma_{12})\,\varrho_{ss} - \frac{1}{2}\mathrm{i}\Delta\,(\varrho_{sa}-\varrho_{as})$$
$$\dot{\varrho}_{aa} = -\frac{1}{2}(\gamma-\gamma_{12})\,\varrho_{aa} + \frac{1}{2}\mathrm{i}\Delta\,(\varrho_{sa}-\varrho_{as})$$

Quantum interference in this kind of system can be utilized to control the decoherence of the excited states. For example, when quantum interference is present, the anti-symmetric excited state, which is a superposition of state 1 and state 2, can have reduced spontaneous emission rate, which is interesting for applications like quantum information processing. Other features of the system includes like ultra-narrow fluorescent spectral lines, which is also a consequence of quantum interference.

## 3.3 Metasurface Enabled Valley Coherence in TMDCs

Recently, atomically thin transition metal dichalcogenides (TMDCs) of the form MX2 (M: Mo, W; X: S, Se, Te) have emerged as a new class of semiconductor materials for both fundamental physics exploration in two-dimensional systems and device applications. These monolayer semiconductors are manifested by a direct band gap between the extrema of valence and conduction bands residing at the energy-degenerate K and K points of the Brillouin zone. Owing to the broken inversion symmetry in monolayer TMDCs, excitons exhibit valley-dependent optical selection rule [24,25]. More specifically, excitons in the K and K' valleys are coupled to photons with the same energy but mutually orthogonal polarization helicities $\sigma_{\pm}$, respectively.

Harnessing the valley degree of freedom in TMDC monolayers for quantum information processing requires coherent manipulation of excitons in the K and K0 valleys, in addition to the inherent selective excitation. The coherence among the valleys (optical alignment of excitons), i.e., valley coherence, was revealed by the observation of a linearly polarized emission (coherent superposition of σ photons) from a TMDC monolayer optically excited by a linearly polarized light [26].

However, all previous approaches to generate valley coherence require the presence of an external coherent field [26-32]. We theoretically demonstrate that intervalley coherence can be spontaneously generated in TMDC monolayers without any external field. We achieve this neutral exciton intervalley coherence by manipulating the vacuum field in the vicinity of the TMDC monolayer with a designed light-molding interface (metasurface), exhibiting an in-plane polarization dependent response.

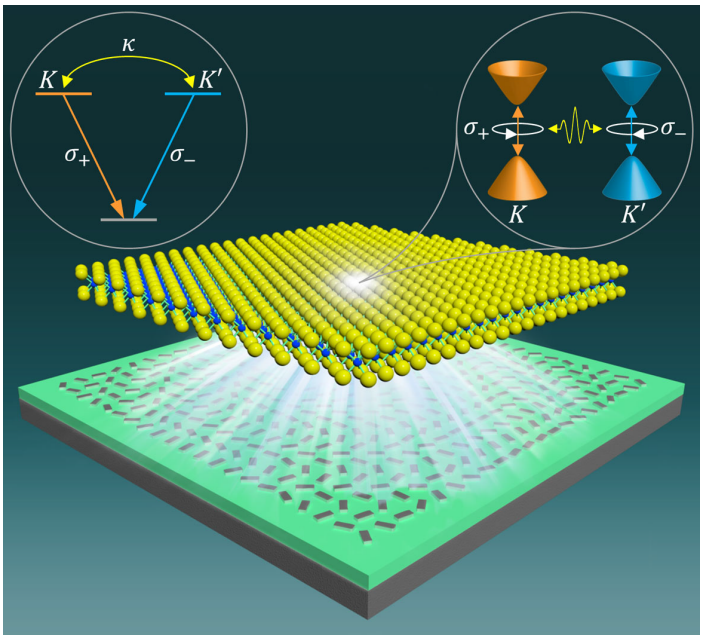

**Figure 3.3.1** Vacuum-induced valley coherence in TMDC monolayers. We considered a monolayer of MX2, positioned at a distant height from the metasurface. We designed a metasurface such that the spontaneous emission from the locally excited TMDC monolayer is efficiently focused back towards the source at the single photon level. Moreover, we engineered the polarization-dependent response of the metasurface to achieve an anisotropic scattered field. The interaction between the suspended TMDC monolayer and the custom designed metasurface yields an anisotropic quantum vacuum. In an ordinary vacuum such as free space, the emission from the K valley with σ+ polarization cannot radiatively excite the orthogonal K' valley with σ− polarization. However, by breaking the isotropic nature of the quantum vacuum in the vicinity of the monolayer via a metasurface, one can remarkably excite the K' valley with an emission from the K valley. Such interaction leads to spontaneous generation of valley coherence and yields quantum interference among their emissions.

We considered an atomically thin layer (monolayer) of TMDC of type MX2 interfaced with a two-dimensional array of subwavelength-spaced optical nanoantenna phase shifters—a metasurface (Fig. 3.3.1). Photonic metasurfaces enable a custom-tailored electromagnetic response with unprecedented control over the fundamental properties of light, i.e., phase, amplitude, and polarization. We assumed that initially one electron is excited to the lowest level of the conduction band of the K valley ($|c_k\rangle$). In free space, which is a homogeneous, isotropic, and linear medium, this excited electron returns to the ground state (i.e., highest level of the valence band $|v_k\rangle$) by emitting a photon with an energy corresponding to the $|c_k\rangle \leftrightarrow |v_k\rangle$ transition. The transient response of the population is $e^{-\gamma Kt}$ and the emission cannot excite the orthogonal K' valley electron. However, by breaking the isotropic nature of the quantum vacuum in the vicinity of the TMDC monolayer, the emission from the K valley can radiatively excite the electron in the K0 valley and vice versa.

We engineer an anisotropic quantum vacuum by introducing a designed interface that its role is to refocus the emitted light from the excitonic dipole to itself for both x and y polarizations of the dipole; however, the scattered field at the location of the dipole for these polarizations reverses sign (i.e., π-phase shifted). Such a polarization dependent response of the metasurface gives rise to an anisotropic decay rate, in which, for one polarization of the dipole, the decay rate is enhanced, while for the second polarization, the decay rate is symmetrically suppressed.

The required anisotropic response was realized by the geometric phase based metasurface introduced in Chapter 3.1. By applying the method of dipole-metasurface interaction [], we obtained the distribution of the scattered field intensity for x- or y-polarized source dipoles, where the efficient light focused back via the metasurface to the quantum emitter is evident (Fig. 3.3.2 (a)). We also calculated the imaginary part of the scattered field at varying x positions to reveal that the metasurface-governed scattered field at the position of the dipole is minimized for an x-polarized dipole while symmetrically maximized for a y-polarized dipole (Fig. 3.3.2(b)). Note that we designed the phase profile of the metasurface such that the imaginary part of the scattered field is predominant, while the real part is suppressed. By considering a finite size metasurface, the Ohmic loss due to the metal, and the phase discretization loss, we achieved that ~47% of the dipole source

field emission is focused back to the dipole. Such a polarization-dependent scattered field Es results in an engineered anisotropic decay rate γ of the quantum emitter as

$$\frac{\gamma(r_1)}{\gamma_0} = 1 + \frac{6\pi\varepsilon_0}{|\wp|^2}\frac{1}{k^3}\mathrm{Im}[\wp^* \cdot E_s(r_1, r_1, \omega)].$$

Here, $\gamma_0$ is the vacuum spontaneous emission decay rate, r1 is the position vector of the dipole, $\varepsilon_0$ is the vacuum permittivity, and $\wp$ is the transition dipole moment of the excitonic dipole. Therefore, the reversed sign of the scattered field at the location of the dipole for x- and y-polarized dipoles gives rise to an anisotropic quantum vacuum, where the engineered normalized decay rate is suppressed (0.53) and symmetrically enhanced (1.47) for x- and y-polarized dipoles, respectively (Fig. 3.3.2(c)). Note that, in the ideal limit of a lossless and infinitely large GPM, the change in the normalized decay rate is 0.5.

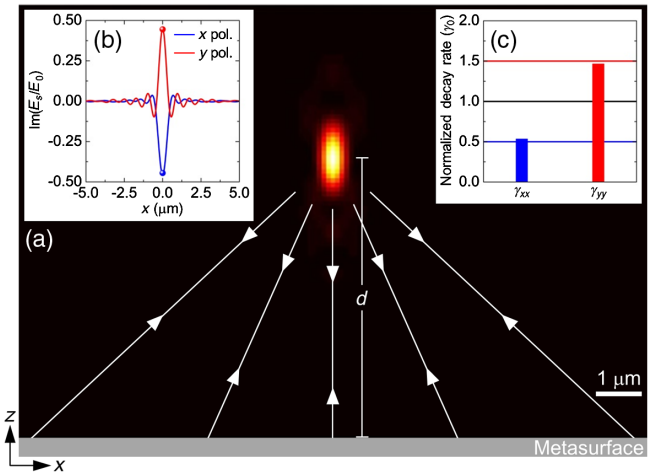


**Figure. 3.3.2** Metasurface-induced anisotropic decay rate. (a) Simulated scattered field intensity distribution for the excitonic dipole source oriented along the x axis. With an optimized design, we achieved ~47% reflection of the incident field focused back towards the on-demand location of the dipole (50% is the upper limit). The scattered field intensity distribution for a y-polarized dipole is identical. (b) Non-degenerate imaginary part of the scattered field. At the position of the dipole, for x- and y-polarized dipoles, the imaginary part of the scattered field is π-phase shifted, i.e., minimized for an x-polarized dipole while symmetrically maximized for a y-polarized dipole. The upper limit for the scattered field is E0, which is the imaginary part of the field induced by the dipole at its position. (c) An anisotropic decay rate is enabled by the metasurface, where the normalized decay rate for x- and y-polarized dipoles is suppressed (0.53) and symmetrically enhanced (1.47), respectively.

The interaction between the quantum vacuum field (i.e., quantum state with the lowest possible energy in the absence of excitations) and the exciton in the TMDC monolayer gives rise to the emergence of intervalley coherence. We consider an exciton in the lowest energy of the valley K initially prepared by resonant optical excitation, we

obtained the excitonic density matrix element, which represents the exciton intervalley coherence, at $t \approx 0$, as

$$\frac{\partial}{\partial t}\left\langle c_{K'}\right|\rho\left|c_{K}\right\rangle = -\frac{1}{2}(\kappa + i\Omega)$$

Here, $\kappa$ and $\Omega$ are the vacuum field mediated coupling and frequency shift, respectively, associated with the imaginary and real parts of the scattered field, respectively.

Note that we designed the phase profile of the metasurface such that the imaginary part of the scattered field is enhanced, while the real part is suppressed, giving rise to predominant $\kappa$ ($-1 \leq \kappa \leq 1$) and negligible $\Omega$ ($\Omega \approx 0$). Only in the presence of the vacuum field mediated parameters, nonzero exciton valley coherence emerges. For a circularly polarized dipole, the coupling term is given by

$$\kappa = (\gamma_{xx} - \gamma_{yy})/2,$$

where $\gamma_{xx}$ ($\gamma_{yy}$) represents the decay rate of a dipole oriented along the x (y) axis. For $\kappa \neq 0$, we need $\gamma_{xx} \neq \gamma_{yy}$, i.e., a structured environment, where different in-plane dipoles decay at different rates. We designed a metasurface that breaks the in-plane isotropic nature of the vacuum at the location of the exciton such that the emission rate for an x-polarized dipole is suppressed, while the decay rate for a y-polarized dipole is symmetrically enhanced. Note that such an engineered anisotropic vacuum increases the contrast between the in-plane decay rates, which enables to maximize the vacuum field mediated coupling. Taking into account all loss channels, we obtained $\gamma_{xx} = 0.53$ and $\gamma_{yy} = 1.47$, which yields $\kappa = -0.47$.

Figure 3.3.3 shows the temporal evolution of the exciton valley coherence. In the presence of a metasurface, a finite exciton valley coherence emerges that reaches its maximum value of ~0.09 and then dies gradually. However, in free space (or any other interface that does not break the in-plane isotropic response, e.g., a mirror), and thus, excitonic valley coherence does not emerge and remains zero, as shown by the dashed line in Fig. 4(b). Moreover, this spontaneously generated intervalley coherence survives in the presence of dominant intervalley scattering, even when it is 1000-fold stronger than the spontaneous decay rate.

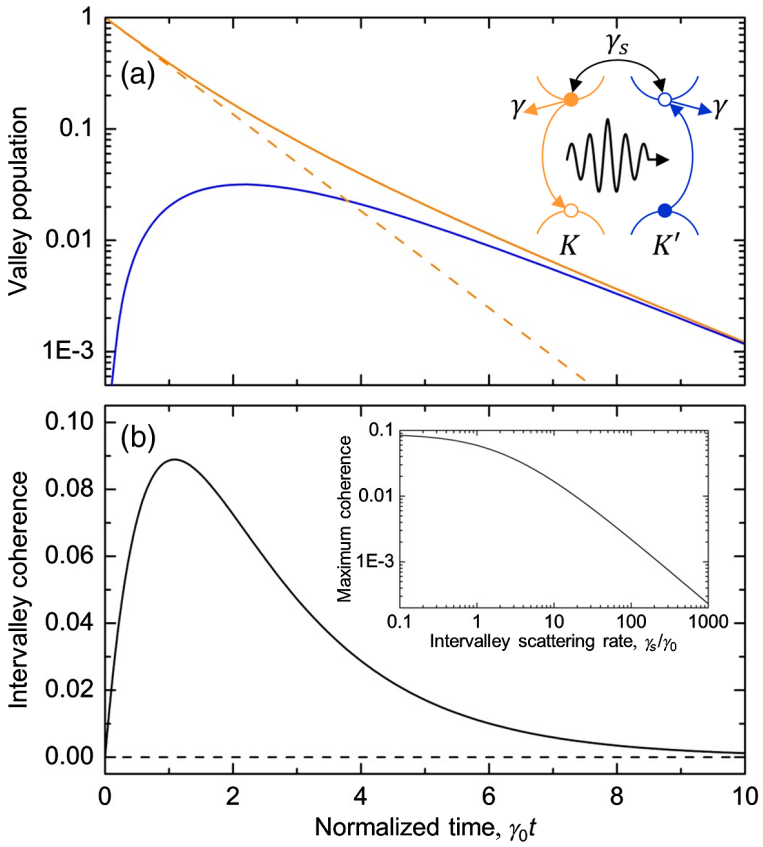


**Figure 3.3.3** Noise-induced valley population-coherence coupling. (a) Temporal evolution of the population of mutually orthogonal valleys (K and K') in the presence (solid lines) and absence (dashed line) of the metasurface. In the presence of the metasurface, the decay rate of the K valley population is reduced along with a finite excitation of the K0 valley. (b) Temporal evolution of intervalley coherence. A nonzero intervalley coherence, indicating coherent excitation of the K0 valley with a photon emitted from the K valley, is evident. This excitation is forbidden in free space (dashed line) due to an optical selection rule. (Inset) Dependence of the maximum intervalley coherence on the intervalley scattering rate, revealing that the generated coherence survives even when the intervalley scattering rate is 1000-fold stronger than the spontaneous decay rate.

## 3.4 Summary

We designed and fabricated metasurfaces based on gap plamon nanostructures. The metasurface posses different phase profile and functionality for different polarizations. By tuning a size of nano-antennas, we realized a metasurface that functions as a reflective focusing lens for x polarization, and a flat mirror for y polarization. And by rotating the nano-antennas, we designed a geometric phase metasurface that works as reflective focusing lens for both x and y polarization but induce different phase shift at the focusing position.

Based on the anisotropic metasurface we designed, we further theoretically demonstrate a spontaneous generation of intervalley coherence in TMDCs by interfacing the metasurface with a MoS2 monolayer. Although we considered the MoS2 monolayer, this proposal is general and can be implemented in different two-dimensional material systems. The metasurface-enabled unprecedented control over the polarization of light gives rise to an anisotropic quantum vacuum in the vicinity of the TMDC monolayer. While intervalley coherence via a vacuum field mediated coupling is forbidden in free space, metasurfaces offer a route to lift the degeneracy in the optical response of in-plane exitonic dipoles. The reported concept of metaphotonics-enabled quantum coherence and interference effects in TMDC monolayers may pave the way for the integration of designer metasurfaces with two dimensional materials for quantum valleytronic metadevices.

## References


[1] A. Streltsov, G. Adesso, and M. B. Plenio, Colloquium: Quantum coherence as a resource, Rev. Mod. Phys. 89, 041003 (2017).

[2] L. Mandel and E. Wolf, Optical Coherence and Quantum Optics (Cambridge University Press, Cambridge, England, 1995).

[3] Q. H. Wang, K. Kalantar-Zadeh, A. Kis, J. N. Coleman, and M. S. Strano, Electronics and optoelectronics of two-dimensional transition metal dichalcogenides, Nat. Nanotechnol. 7, 699 (2012).

[4] Z. Ye, T. Cao, K. O'Brien, H. Zhu, X. Yin, Y. Wang, S. G. Louie, and X. Zhang, Probing excitonic dark states in single-layer tungsten disulphide, Nature (London) 513, 214 (2014).

[5] H. Zeng, J. Dai, W. Yao, D. Xiao, and X. Cui, Valley polarization in MoS2 monolayers by optical pumping, Nat. Nanotechnol. 7, 490 (2012).

[6] K. F. Mak, K. He, J. Shan, and T. F. Heinz, Control of valley polarization in monolayer MoS2 by optical helicity, Nat. Nanotechnol. 7, 494 (2012).

[7] A. M. Jones, H. Yu, N. J. Ghimire, S. Wu, G. Aivazian, J. S. Ross, B. Zhao, J. Yan, D. G. Mandrus, and D. Xiao et al., Optical generation of excitonic valley coherence in monolayer WSe2 , Nat. Nanotechnol. 8, 634 (2013).

[8] M. Tokman, Y. Wang, and A. Belyanin, Valley entanglement of excitons in monolayers of transition-metal dichalcogenides, Phys. Rev. B 92, 075409 (2015).

[9] K. Hao, G. Moody, F. Wu, C. K. Dass, L. Xu, C.-H. Chen, L. Sun, M.-Y. Li, L.-J. Li, and A. H. MacDonald et al., Direct measurement of exciton valley coherence in monolayer WSe2 , Nat. Phys. 12, 677 (2016).

[10] R. Schmidt, A. Arora, G. Plechinger, P. Nagler, A. G. del Águila, M. V. Ballottin, P. C. M. Christianen, S. M. de Vasconcellos, C. Schüller, and T. Korn et al., Magnetic-Field-Induced Rotation of Polarized Light Emission from Monolayer WS2 , Phys. Rev. Lett. 117, 077402 (2016).

[11] Sun, Shulin, et al. "High-efficiency broadband anomalous reflection by gradient meta-surfaces." Nano letters 12.12 (2012): 6223-6229.

[12] Pors, Anders, et al. "Gap plasmon-based metasurfaces for total control of reflected light." Scientific reports 3 (2013): 2155.

[13] Z. Bomzon, G. Biener, V. Kleiner, and E. Hasman, Space-variant Pancharatnam-Berry phase optical elements with computer-generated subwavelength gratings, Opt. Lett. 27, 1141 (2002).

[14] E. Hasman, Z. Bomzon, A. Niv, G. Biener, and V. Kleiner, Polarization Beam-Splitters and Optical Switches Based on Space-Variant Computer-Generated Subwavelength Quasi-Periodic Structures, Opt. Commun. **209**, 45 (2002).

[15] N. Shitrit, I. Bretner, Y. Gorodetski, V. Kleiner, and E. Hasman, Optical Spin Hall Effects in Plasmonic Chains, Nano Lett. **11**, 2038 (2011).

[16] D. Lin, P. Fan, E. Hasman, and M. L. Brongersma, Dielectric Gradient Metasurface Optical Elements, Science **345**, 298 (2014).

[17] G. Zheng, H. Mühlenbernd, M. Kenney, G. Li, T. Zentgraf, and S. Zhang, Metasurface Holograms Reaching 80% Efficiency, Nat. Nanotechnol. **10**, 308 (2015).

[18] M. Khorasaninejad, W. T. Chen, R. C. Devlin, J. Oh, A. Y. Zhu, and F. Capasso, Metalenses at Visible Wavelengths: Diffraction-Limited Focusing and Subwavelength Resolution Imaging, Science **352**, 1190 (2016).
[19] Liu, R. C., et al. "Quantum interference in electron collision." Nature 391.6664 (1998): 263.
[20] Anderson, Brian P., and Ma A. Kasevich. "Macroscopic quantum interference from atomic tunnel arrays." Science282.5394 (1998): 1686-1689.
[21] Andrews, M. R., et al. "Observation of interference between two Bose condensates." Science 275.5300 (1997): 637-641.
[22] Hong, Chong-Ki, Zhe-Yu Ou, and Leonard Mandel. "Measurement of subpicosecond time intervals between two photons by interference." Physical review letters 59.18 (1987): 2044.
[23] Horodecki, Ryszard, et al. "Quantum entanglement." Reviews of modern physics 81.2 (2009): 865.
[24] H. Zeng, J. Dai, W. Yao, D. Xiao, and X. Cui, Valley polarization in MoS2 monolayers by optical pumping, Nat. Nanotechnol. 7, 490 (2012).
[25] K. F. Mak, K. He, J. Shan, and T. F. Heinz, Control of valley polarization in monolayer MoS2 by optical helicity, Nat. Nanotechnol. 7, 494 (2012).
[26] A. M. Jones, H. Yu, N. J. Ghimire, S. Wu, G. Aivazian, J. S. Ross, B. Zhao, J. Yan, D. G. Mandrus, D. Xiao et al., Optical generation of excitonic valley coherence in monolayer WSe2, Nat. Nanotechnol. 8, 634 (2013).
[27] C. R. Zhu, K. Zhang, M. Glazov, B. Urbaszek, T. Amand, Z.W. Ji, B. L. Liu, and X. Marie, Exciton valley dynamics probed by Kerr rotation in WSe2 monolayers, Phys. Rev. B 90, 161302 (2014).
[28] M. Tokman, Y. Wang, and A. Belyanin, Valley entanglement of excitons in monolayers of transition-metal dichalcogenides, Phys. Rev. B 92, 075409 (2015).
[29] K. Hao, G. Moody, F. Wu, C. K. Dass, L. Xu, C.-H. Chen, L. Sun, M.-Y. Li, L.-J. Li, A. H. MacDonald et al., Direct measurement of exciton valley coherence in monolayer WSe2, Nat. Phys. 12, 677 (2016).
[30] R. Schmidt, A. Arora, G. Plechinger, P. Nagler, A. G. del Águila, M. V. Ballottin, P. C. M. Christianen, S. M. de Vasconcellos, C. Schüller, T. Korn et al., Magnetic-Field-Induced Rotation of Polarized Light Emission from Monolayer WS2, Phys. Rev. Lett. 117, 077402 (2016).
[31] G. Wang, X. Marie, B. L. Liu, T. Amand, C. Robert, F. Cadiz, P. Renucci, and B. Urbaszek, Control of Exciton Valley Coherence in Transition Metal Dichalcogenide Monolayers, Phys. Rev. Lett. 117, 187401 (2016).
[32] Z. Ye, D. Sun, and T. F. Heinz, Optical manipulation of valley pseudospin, Nat. Phys. 13, 26 (2017).

# Chapter 4

# Manipulating the Kinetic Motions of Meta-Atoms with Artificial Optical Magnetism

Light-matter interactions in the context of optical trapping have attracted great interests and fostered wide-reaching scientific innovations ranging from biology to physics. Fundamentally, optical trapping and manipulation of objects in space exploit the momentum of light, which relies on strong field gradient. However, optical trapping forces have so far been based purely on electric interactions of light due to the absence of natural optical magnetism.

In the last decades, however, the emergence of the metamaterials concept has motivated intense research efforts in the development of subwavelength structures that support artificial optical magnetism, which provides possibilities to the realization of various novel applications, including negative refractive index, cloaking and Huygen's metasurfac. Recently, high-index dielectric particles have seen growing attention for achieving artificial optical magnetism. According to the Mie theory, they can exhibit strong magnetic resonances without the high dissipation that is inherent to metal structures. The high quality resonance and small footprint also make them good candidate as non-invasive probes for nanosensing and imaging, which has attracted interests in the optical trapping research.

Here we demonstrate trapping and manipulation of high-index dielectric nanoparticles by utilizing the magnetic properties of light. By uniquely developing a periodical magnetic light-field geometry, we show that silicon nanospheres can be selectively trapped and deflected based on the strength of their magnetic polarizability. Elevating magnetic interactions between light and particles can open up a new degree of freedom for optical manipulation of microscopic objects.

## 4.1 Optical Trapping with Electric Interaction

Optical forces can be used to trap and manipulate microscopic objects [1,2], which forms the foundation for broad-reaching applications in biology and physics. In physics, laser cooling of atoms paved the way to modern ultra-cold atom technology [3]. In biology, optical tweezers opened the platform to noncontact trapping and manipulation of living cells and biological molecules [4,5], as well as noncontact force transducer with sensitivity on the order of pico-newtons [6,7]. Combining optical lattices with microfluidics, optical forces have also enabled sorting and fractionation of microscopic particles based on their refractive indices [8-12], and has been applied to colloidal, moleculer and biology research.

The force exerted by light on a particle can be understood in terms of changes in the momentum flux of the trapping beam. The momentum flux of a light beam can be written as

$$p = nP/c.$$

Here, p is the magnitude of the momentum flux, P is the power of the light beam and n is the refractive index of the medium. The direction of the momentum flux is the same with the propagation direction (k vector) of the light beam.

For a particle in the focused laser beam, the force it experience consists an axial force that is along the light propagation axis, and a radial force that is perpendicular to the light propagation axis. The axial force acting on the particle results from the changes in the convergence or divergence of the beam. The radial force, on the other hand, comes from the change of the propagation direction of the beam. Consider when the beam is deflected by the particle in one direction, its momentum flux increases in that direction, resulting a force on the particle in the opposite direction.

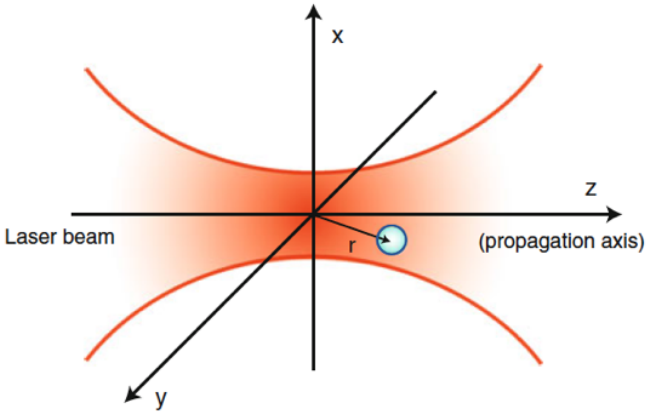


**Figure 4.1.1** An object trapped in a focused laser beam.

When the particle size is small compared to wavelength, an analytical solution to the

optical forces can be achieved under Rayleigh approximation. Treating the particle as a point electric dipole, the optical forces acting on a particle in a light field can be computed. The optical forces can further be decomposed into two types: an optical gradient force and an optical scattering force. In a focused laser beam, the gradient force is perpendicular to the light propagation axis (equivalent to the radial force discussed above) and the scattering force is along the propagation axis (equivalent to the axial force discussed above). Analytical, the optical gradient force can be expressed with the following formula:

$$F_{grad} = \frac{1}{2}\mathrm{Re}(\alpha_E)\nabla E(\vec{r})^2,$$

where $\alpha_E$ is the electric polarizability of the particle. It can be seen that the optical gradient force is proportional to the real part of the particle's electric polarizability and the gradient of the electric field intensity. For a particle with refractive index larger than the surrounding environment, the gradient force acts as a trapping force that pulls the particle towards the center of the beam.

The scattering force is proportional to the imaginary part of the electric polarizability and the intensity of the electric field:

$$F_{scat} = \sigma_{scat}\frac{I(\vec{r})}{c}\vec{z},$$

where $\sigma_{scat}$ is the scattering cross-section of the particle. The scattering force pushes the particle outside the focus spot along the beam propagating direction.

A particle can only be stably trapped when the gradient force is larger than the scattering force. For a non-resonating dielectric sphere, the gradient force is proportional to the volume of the sphere (i.e. proportional to $r^3$), and the scattering force is proportional to the square of the sphere volume (proportional to $r^6$). For very small particles, the scattering force is negligible comparing to the gradient force. However, as the size of the particle increases, the scattering force increases rapidly, which places an upper bound on the size of particles that can be trapped.

The lower bound of the particle size that can be trapped comes from the competition between the gradient force and the Brownian motion of particles. Since the gradient force decreases with the volume of the particle, nanoparticles are usually hard to be trapped since the gradient force cannot overcome the Brownian motion of the nanoparticles. For an absorbing particle, the laser beam can induce heating of the particle, which increases the kinetic energy and Brownian motion of the particle and make the particle harder to be trapped.

Due to the reasons above, the use of optical tweezers has mainly been focused on the manipulation of microscopic particles. It has been demonstrated that the trap stiffness can be maximized when the particle radius is approximately equal to the beam waist [13]. In recent years, however, new approaches have been developed to stably trap and

manipulate nanoparticles, which includes trapping metallic nanoparticles using the plasmonic resonances enhanced trapping force [14-16], trapping CNTs and nanowires using their highly anisotropic geometries [17-19], and trapping particles with enhanced field near plasmonic structures [20-22].

Note that in the all of the analysis above, we assume that the optical forces arise only from the interaction between the electric field of light and the induced electric dipoles in the objects. The magnetic interaction is neglected since the magnetic response of natural materials is usually very weak in the optical spectral range.

## Trapping high-index particles

Now we look at how the gradient force and scattering force depends on the refractive index of the particle. For a non-resonant dielectric sphere, the gradient force is

$$F_{grad} \propto \Delta n \frac{n_p + n_m}{n_p^2 + 2n_m^2}.$$

And the scattering force is

$$F_{scat} \propto (\Delta n)^2 (\frac{n_p + n_m}{n_p^2 + 2n_m^2})^2.$$

Here, $n_p$ is the refractive index of the particle, $n_m$ is the refractive index of the medium, and $\Delta n = n_p - n_m$ is the refractive index difference. From the equations above, it can be seen that as the refractive index of the particle increases, the scattering force grows faster than the gradient force. Therefore it is hard to trap high refractive index particles with a single laser beam since the scattering force dominates.

Counter propagating beams setup has been used to trap high-index particles. By counter propagating two focused laser beam, the scattering force can be cancelled and titanium particles with refractive index 2.4 and diameter 1.1 μm have been trapped [23]. However, in this case, the total trapping force is smaller than that in a single trapping beam.

Another method to trap high index particles is to apply an anti-reflection coating on the particles. The simplest type of anti-reflection coating is a thin layer of material with refractive index that is equal to the geometric mean of the particle and the medium. By coating polystyrene particles with a thin layer of silica, the trapping force has been enhanced by 2 – 3 folds [24]. And by coating titania particles with an anti-reflective shell, they can be stably trapped with a single laser beam [25], and the trapping stiffness is 3 orders larger than the typical optical tweezers.

## 4.2 Artificial Optical Magnetism

In the optical spectral range, the magnetic response of natural materials is generally very weak [26]. The magnetic permeability μ is usually very close to 1, while the electric permittivity ε has a much greater diversity, which can range from large negative values to large positive values. This difference comes from the intrinsic asymmetry between the electric and magnetic effect. Due to the lack of magnetic monopoles, materials are hard to couple with oscillating magnetic field. For example, for single atoms, the direct coupling with magnetic field is 137 times smaller than that with the electric field.

In the last decades, however, the emergence of the metamaterials concept has motivated intense research efforts in the development of subwavelength structures that support artificial optical magnetism, which provides possibilities to the realization of various novel applications, including negative refractive index, invisibility cloaking and superlenses. One of the basic building blocks of metamaterials – split ring resonators (SRR) [27,28], can function as an artificial magnetic dipole and produce strong magnetic coupling to an electromagnetic field. SRRs can generate the desired magnetic susceptibility for wavelength up to a few hundred THz. However, for shorter wavelengths down to the optical spectral range, SRRs fails because of the high metal loss and the difficulties in the fabrication of small split ring nanostructures.

In the optical frequency range, plasmonic nanoclusters [29,30] have been engineered to produce artificial optical magnetism. The response of plasmonic nanoclusters can be understood by analyzing the hybridization of modes in each plasmonic nanoparticles. When the individual nanoparticles are brought very close to each other, strong couplings arises between the individual electric dipolar plasmon, which gives rise to hybridized collective modes, and effectively generate a magnetic dipole response. However, plasmonic nanostructures still suffer from losses inherent to metals at visible frequencies, which hinders the realization of high photon efficiency.

Recently, high-index dielectric particles have seen growing attention for achieving artificial optical magnetism [31,32]. According to the Mie theory, high-index dielectric particles can exhibit strong magnetic resonances without the high dissipation that is inherent to metal structures. The high quality resonance and small footprint also make them good candidate as non-invasive probes for nanosensing and imaging, which has attracted interests in the optical trapping research [33-35].

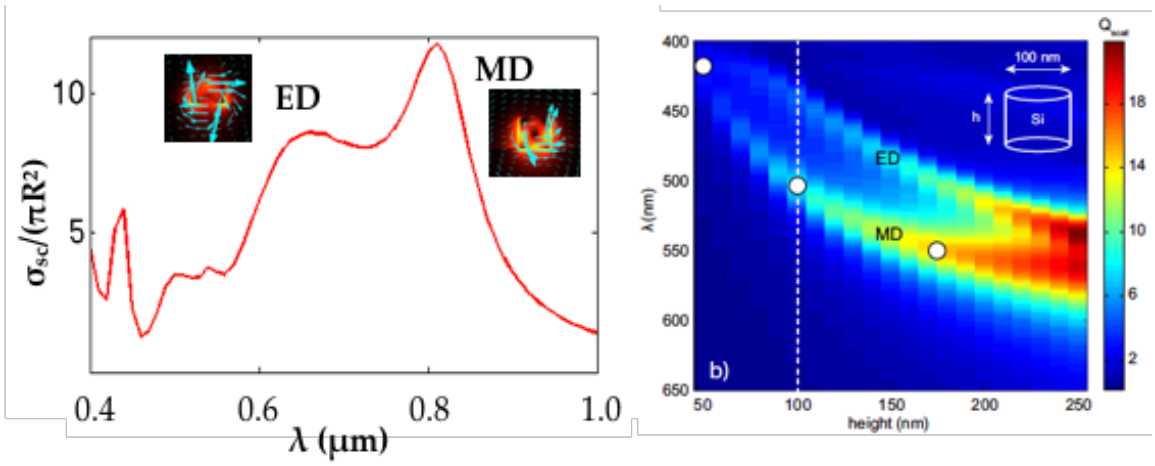


**Figure 4.2.1** Magnetic and electric dipole resonances of a silicon nano-cylinder in the visible regime. Left: The scattering cross section spectrum of silicon cylinder (The diameter and the height of the cylinder are both 150 nm). The two peaks correspond to the electric dipole resonance and the magnetic dipole resonance, respectively. The insets show the electric field distribution at the resonances. Right: (figure reprinted from ref. []) The scattering cross section of a silicon cylinder as the function of cylinder height and wavelength. The cylinder diameter is fixed at 100 nm.

## 4.3 Optical Trapping with Magnetic Interaction

In this work, we experimentally demonstrate that optical magnetism can be utilized for trapping and manipulation of high-index dielectric particles. The optical forces arising from magnetic interaction have the potential for offering invaluable control parameters for fine contact-free manipulation of micro- or nano-scopic objects.

### 4.3.1 Experimental design

To demonstrate manipulation with only the magnetic part of light, we study the transport of submicron colloidal silicon spheres flowing past a periodic magnetic landscape (Fig. 4.3.1). A particle inside the periodic landscape experiences a competition between an optical trapping (gradient) force exerted by the magnetic field arrays and a uniform dragging force applied by the flow. If the optical trapping force is sufficiently stronger than the dragging force, the particle can be trapped into a plane of magnetic field maximum and it's trajectory will be deflected and align with the direction of the magnetic arrays.

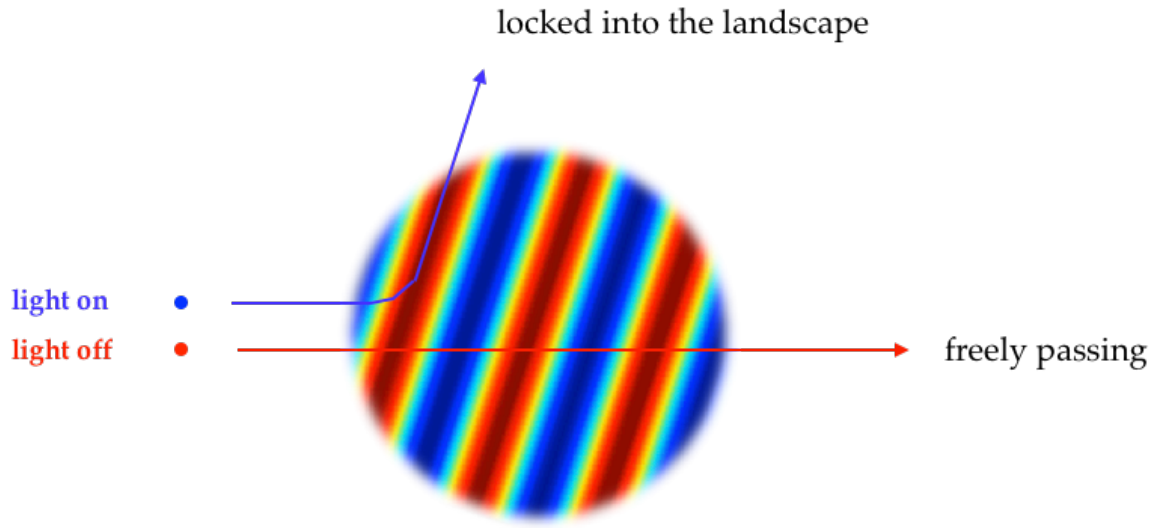


**Figure 4.3.1** Transport of a magnetic dipole particle inside of a periodic magnetic landscape. Left: Schematics of the experimental setup. The silicon particles are confined in a microfluidic channel. Two perpendicular light beams are focused and interfere inside the channel. (b) The interfered light field forms a periodic magnetic landscape. The particle is carried by a microfluidic flow.

The periodic magnetic landscape can be created by interfering two plane waves traveling

at perpendicular directions. When the two beams are p-polarized, the electric fields in the two beams are perpendicular to each other, and thus creating a uniform electric field. The magnetic fields in the two beams are parallel to each other, and thus creating a periodic sinusoidal landscape, with periodicity $= \lambda / \sqrt{2}$.

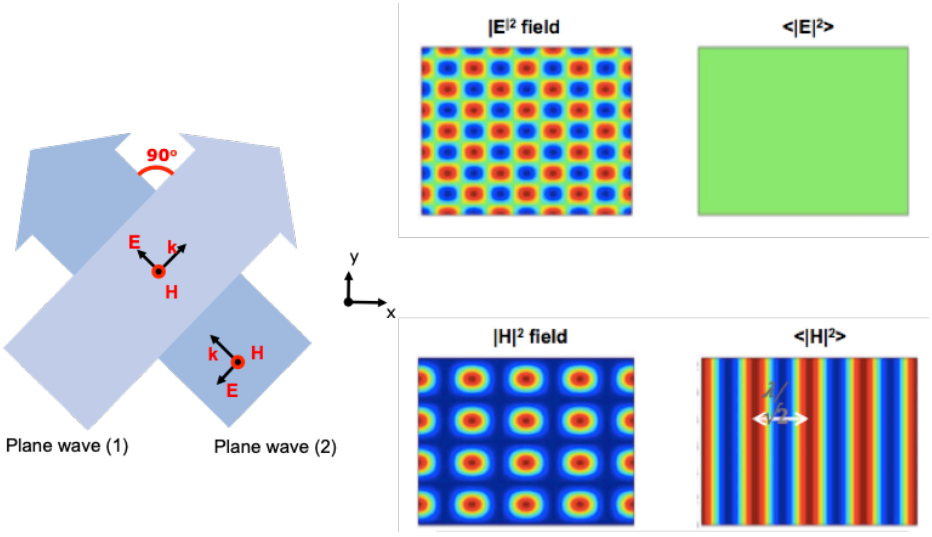


**Figure 4.3.2** Creation of the periodic magnetic landscape with a uniform electric landscape, by interfering two p-polarized perpendicular travelling light beam. The center figures are the instant $|E|^2$ and $|H|^2$ at a certain time. The right figures are the time average electric and magnetic field intensity.

The schematics of the experimental setup is illustrated in Fig. 4.3.3. We confine the silicon colloids in a microfluidic channel. The silicon particles can be driven by the flow inside the microfluidic channel. A single mode laser beam is splitted by a beamsplitter and then focused into the microfluidic channel from the top. The polarizations of the laser beams are controlled by a half-wave plate and a linear polarizer. When the two beams are both p-polarized, their interference creates a periodic sinusoidal magnetic landscape inside the microfluidic channel. A microscope is placed below the microfluidic channel to image the silicon particles and the electromagnetic landscape. An IR camera is used to image the electromagnetic landscape created by the laser, and a visible camera is used to image the silicon particles under white light illumination.

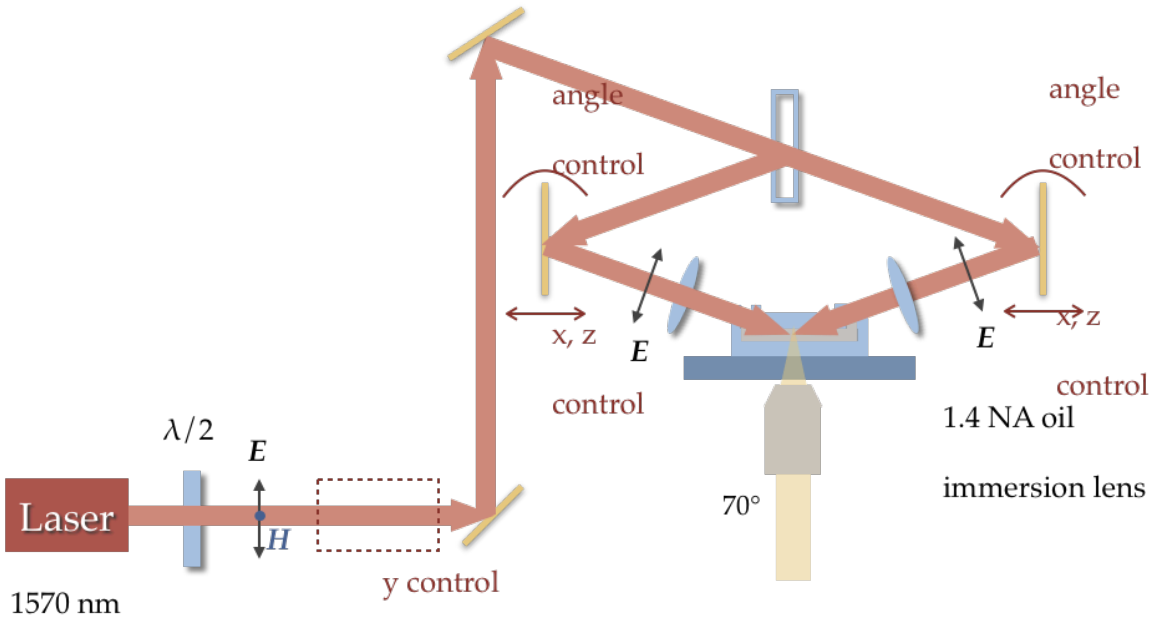


**Figure 4.3.3** Schematics of the experimental setup. The laser is tunable from 1530 nm to 1570 nm, and the power can be enhanced by an erbium-doped fiber amplifier (EDFA) to up to 100 mW. The output is coupled through a single mode fiber. The polarization the laser beam is controlled by a half waveplate and a linear polarizer. The goal of the alignment is to overlap the three focus spot inside the microfluidic channel. Two of the focus spots are from the two top beams that creates the magnetic periodic landscape, the other focus spot is from the 1.4 NA oil immersion objective lens that is used to image the silicon particles and the electromagnetic lanscape. The two mirrors' angles can be adjusted to make sure that the two top beams travels at exactly 90 degrees to each other inside the microfluidic channel.

The schematics of the microfluidic channel is shown in Fig. 4.3.4. The microfluidic channel is 4 μm deep, created by a 1 mm PDMS layer on top of a cover glass. The microfluidic channel is filled with 1:1 water/TDE mix, so that the liquid refractive index matches the refractive index of the PDMS (1.4), minimizing the reflection at the PDMS/liquid interface. The flow velocity inside the microfluidic channel can be controlled by the pressure difference or applied voltage difference at the two reservoir.

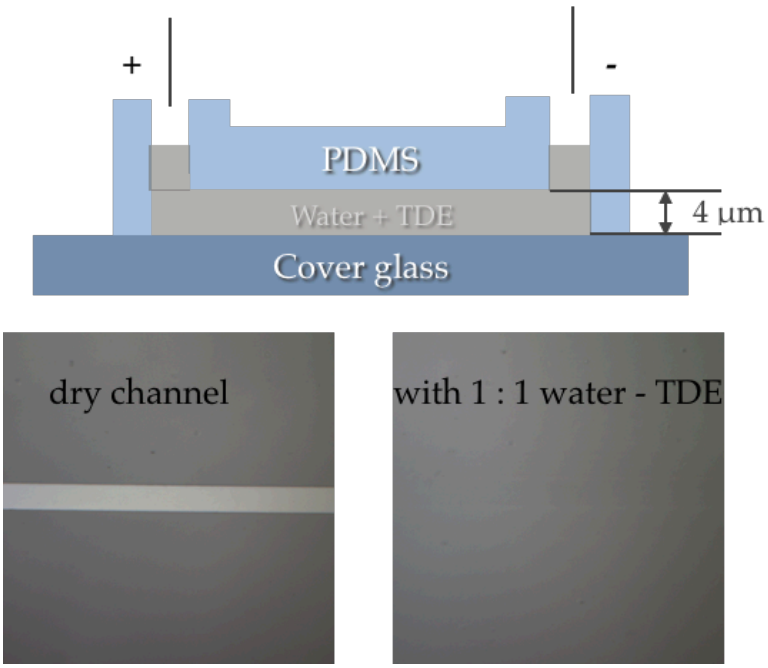


**Figure 4.3.4** Schematics of the microfluidic channel. When the channel is dry (no liquid inside), the microfluidic channel is clearly visible from the optical image. When the channel is filled with water/TDE mix, the channel disappears in the optical image since the liquid refractive index exactly matches the refractive index of PDMS.

We image the electromagnetic field inside the with an IR camera. Since the camera only captures the electric field intensity of the electromagnetic waves, the magnetic intensity cannot be directly imaged. However, the magnetic intensity landscape can be derived from the electric intensity landscape, and the magnetic intensity landscape at p-polarization has the same form with the electric intensity landscape at s-polarization. Fig. 4.3.5 shows the electric intensity landscape at s- and p- polarization captured on the IR camera. When the two beams are s-polarized, we observe a periodic electric field, indicating uniform magnetic field intensity. When the two beams are p-polarized, we observe a uniform electric intensity landscape, indicating periodic magnetic field intensity.

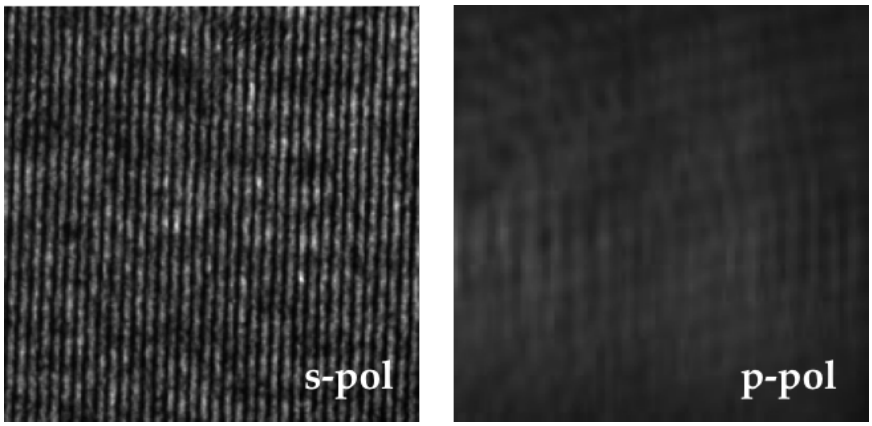


**Figure 4.3.5** Electric field intensity in the interfered region, measured by a CCD camera. Left: the two light beams are both s-polarized, leading to a periodic electric field (uniform magnetic field). Right: the two light beams are both p-polarized, leading to a uniform electric field (periodic magnetic field).

### 4.3.2. Silicon nanospheres synthesis and characterization

We synthesized the silicon spheres by decomposition of $Si_3H_8$ in supercritical n-hexane at high temperature, followed by a vacuum annealing treatment [36]. The size and refractive index of the silicon spheres can be controlled by the annealing temperature. Here we preheat the Muffle to 490 °C, which is 60 °C above the target temperature. Following this, 10mL titanium reactor is injected with 5.8 ml of n-hexane and 25 µL of trisilane in nitrogen filled glovebox, then sealed and moved to the Muffle furnace. Soon after, we set the heating temperature of the furnace to 430°C. After a 25-minute heating, the reactor is removed from the furnace, immersed into ice water and cooled down to room temperature. After that, the hydrogenated amorphous silicon colloid is taken out from the reactor, calcined two hours at 600°C in vacuum after centrifugation and, finally, dispersed in water.

We synthesized multiple batches of silicon nanospheres are different annealing temperature and duration, shown in Fig.4.3.6. It can be seen that for most batches, the silicon nanospheres are a mixture of larger uniform spheres and very small spheres. Here we only want the larger spheres, so the particles are filtered with a centrifugal filter of 0.22 µm pore size to remove the very small spheres. The particles are further filtered with a centrifugal filter of 0.65 µm pore size to remove the particle clusters.

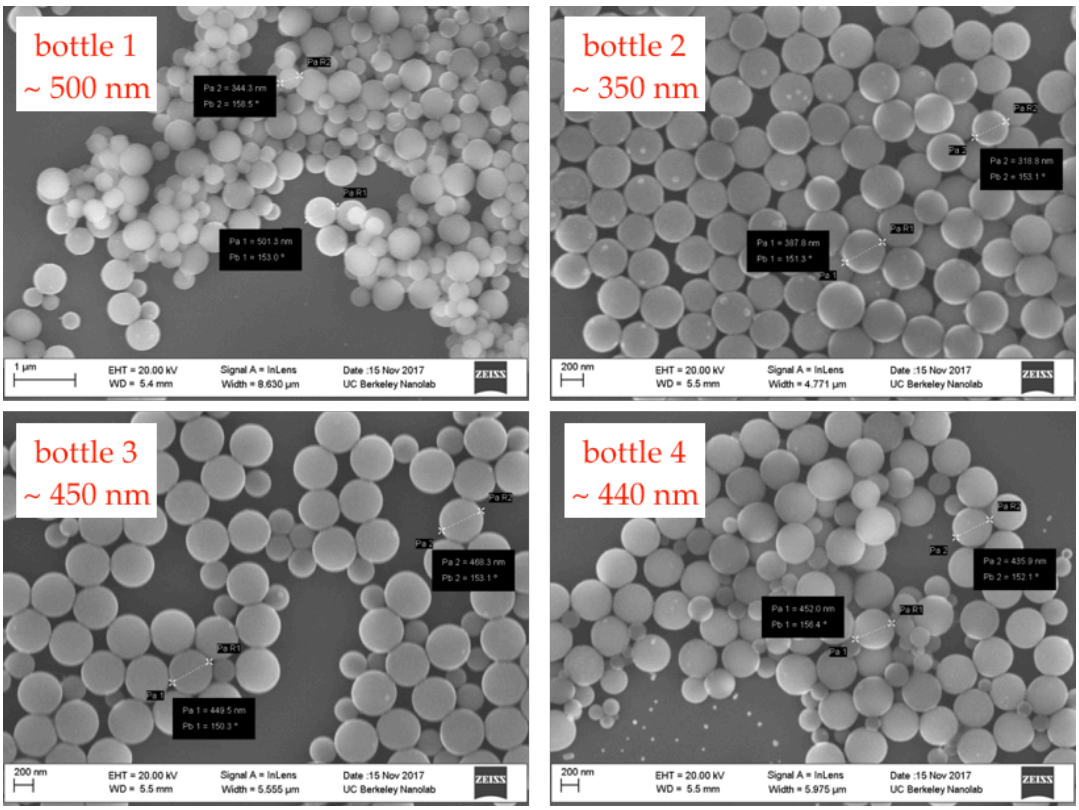


**Figure 4.3.6** SEM images of the four batches of the synthesized silicon colloids.

We characterized the resonance property of the different batches with an FTIR. Bottle 4 is selected to be used in the trapping experiment since its magnetic dipole resonance is close to our laser wavelength (tunable from 1530 nm to 1570 nm). The scanning electron microscope (SEM) image shows that the bottle 4 silicon colloid after filtering has an average diameter of 450 nm and high monodispersity (Figure 4.3.7). Reflection measurement of silicon colloids located on glass substrate reveals the magnetic and electric dipole modes (Figure 4.3.7(b)). A strong magnetic dipole mode appears at 1500 nm, and a weak, broad electric dipole mode can be found at around 1200 nm. Based on the measurement, a fit to the Mie theory yielded a refractive index value of 90% of that of bulk silicon. A simulation is then performed to calculate the real and imaginary part of the magnetic polarizability $\alpha_M$ of the silicon spheres. The optical trapping (gradient) force, which is proportional to the real part of the $\alpha_M$, reaches its maximum at 1.6 μm wavelength.

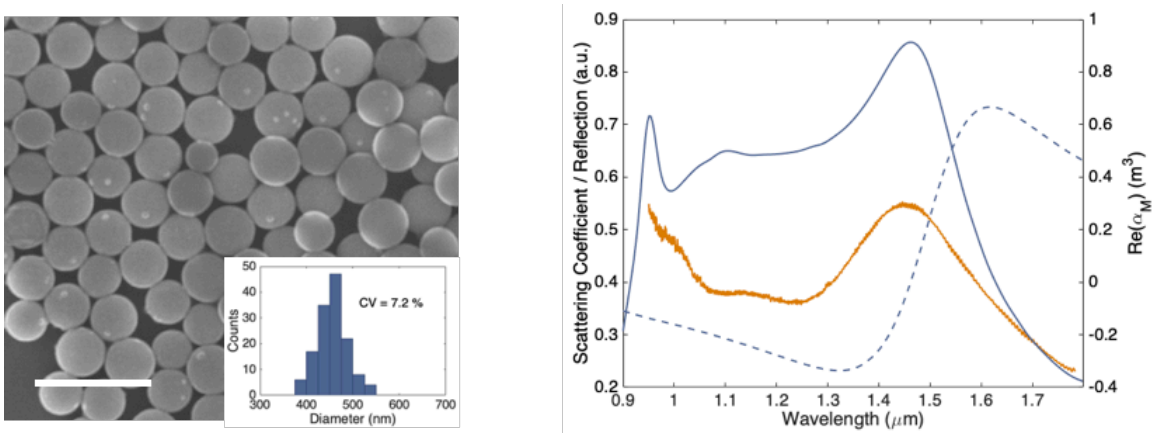


**Figure 4.3.7** Characterization of the synthesized silicon colloids. Left: SEM image of the silicon colloids. The silicon spheres have an average diameter of 450 nm and coefficient of variation (CV) of 7.2 %. Right: The solid blue curve is the simulated scattering coefficient spectrum of the silicon spheres, the solid orange curve is the reflection spectrum of silicon spheres scattered on a glass substrate, measured by Fourier Transform Infrared Spectroscopy (FTIR). The strength of the trapping force is proportional to the real part of the magnetic polarizability, which is plotted with the dashed line.

Considering the size distribution in the silicon colloids sample, we also analytically calculated Re($\alpha_M$) of the silicon nanospheres in water as a function of silicon sphere diameter and excitation wavelength under dipole approximation, shown in Fig. 4.3.8. When the particle is on exactly resonance, Re($\alpha_M$) is zero. Re($\alpha_M$) dramatically increases when the excitation wavelength is slightly red shifted. At excitation wavelength of 1570 nm (fixed throughout this experiment), the real part of the magnetic polarizability ranges from around $1 - 7 \times 10^{-19}$ m3, with maximum value reached at 450 nm diameter, and gradually decreasing on both sides.

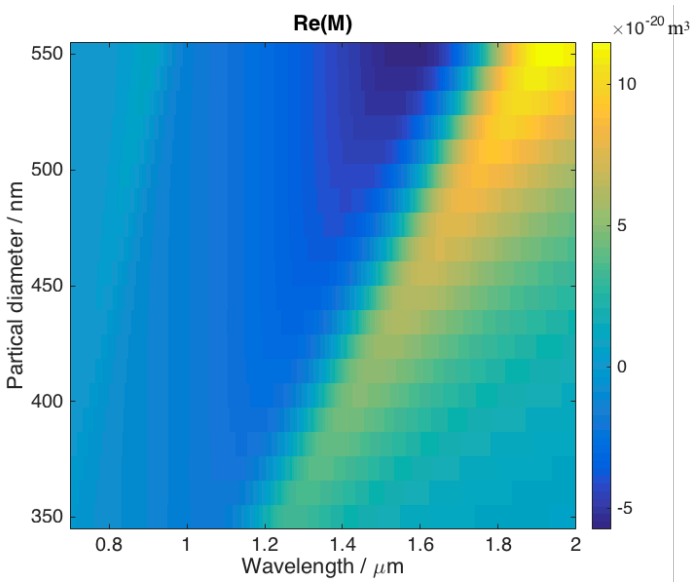


**Figure 4.3.8** Re($\alpha_M$) of a silicon sphere in water as a function of silicon sphere diameter and excitation wavelength, analytically calculated under dipole approximation.

### 4.3.3. Trajectory tracking of silicon nanospheres

The silicon nanospheres' motions inside the microfluidic channel are recorded with an EMCCD camera. The particles are then automatically identified and the trajectories are extracted with the method of digital video microscopy [37]. The method contains two major steps as follows.

Step 1: locate the center of the particles in each frame, as shown in Fig.4.3.8 left. The nanospheres are located by finding local maximum of the brightness. These locations are further examined to distinguish between real particles and spurious ones. The most important way we used is to look at the total brightness in the neighborhood. Locations whose total brightness that are too small (refer to noises, or background, not real particles) or too large (refer to a cluster of particles) are removed.

Step 2: link locations in different frames into particle trajectories, as shown in Fig. 4.3.9 right. From step 1, we have the locations of the particles in each frame. Next we track particles from frame to frame, giving each one a number for identification. First, we must specify a maximum displacement, the farthest a particle can travel between frames. Second, we allow for the possibility that a particle might be missed for a few frames and then seen again. (Perhaps its total brightness slipped below our cutoff due to noise in the video.) Memory keeps track of disappeared particles and maintains their ID for up to some number of frames after their last appearance.

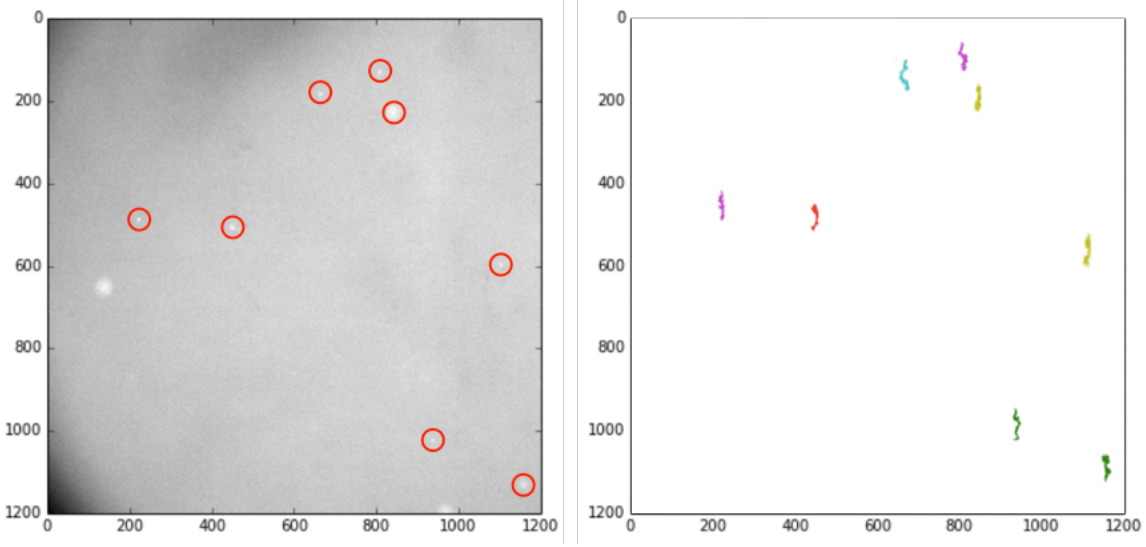


**Fig. 4.3.9** Particle tracking technique. Left: identifying the locations of silicon nanospheres in one frame. Right: Linking the locations in different frames into the trajectories of silicon nanospheres.

### 4.3.4 Trapping and manipulation of silicon nanospheres

We first investigate one-dimensional trapping of silicon colloids in the absence of flow. Trapping measurements were performed on individual spheres. For each trapped sphere, the fluctuations in its position within the trap were recorded via digital video microscopy []. Nanoparticles dispersed in an aqueous medium undergo rapid Brownian motion that is determined by the temperature and hydrodynamic properties of the particle and surrounding fluid. A gradient force optical tweezers imposes a confining potential that limits this stochastic motion to a small volume about the focus of the trapping laser. The resulting equations of motion can be approximated by a series of uncoupled overdamped harmonic oscillators, where each translational coordinate $\vec{q}$ = (x, y, z) is associated with an optical restoring force of the form $F_i = k_i q_i$. From the equipartition theorem, the probability of the trapped particle being displaced from the center of the trap is given by the Boltzmann distribution []:

$$P(q_i) \propto \exp(-\frac{U(q_i)}{k_b T}) = \exp(-\frac{k_i q_i^2}{2k_b T})$$

where U ($q_i$) is the confining potential in the $q_i$ dimension, $k_i$ the trap stiffness, $k_b$ Boltzmann' s constant, and the temperature T = 296 K.

Fig. 4.3.10 depicts the histogram of the position of a single trapped particle in the trapping direction, which is observed to fluctuate around the center of the trap. A Gaussian fit based on the equation above yield trap stiffnesse of k = 10.4 ± 0.3 pN/μm for a trapping power of 86 mW focused in a 100 μm region. The trap stiffness increases linearly with respect to the trapping power. Here we measured a trapping stiffness per unit power of 116 $pN \cdot \mu m^{-1} \cdot W^{-1}$.

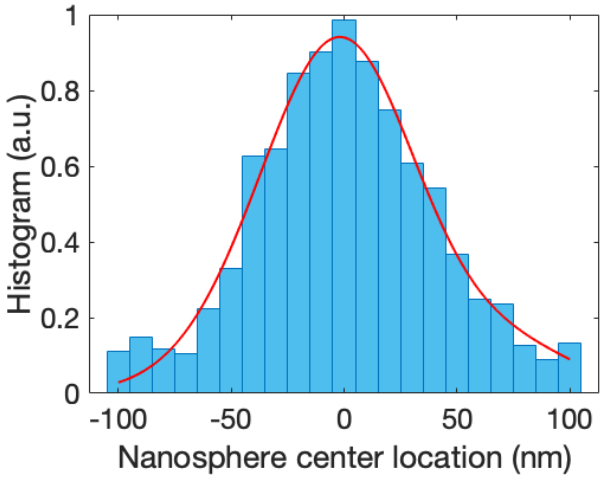


**Figure 4.3.10** Experimental (bars) and Gaussian fit (line) of the particle positions with respect to the center of the magnetic arrays.

Furthermore, we demonstrate deflection of silicon colloids when a flow is present, which is oriented at a 25° angle to the magnetic landscape. Without light on, the silicon particles transport along the direction of the water flow. When the light is on, the majority of the particles are deflected and locked into the magnetic landscape. The less than perfect efficiency here can be explained by the silicon particles' size distribution, since the particles have diameters ranging from 400 nm to 500 nm, and particles with too small or too big diameters are less likely to be trapped.

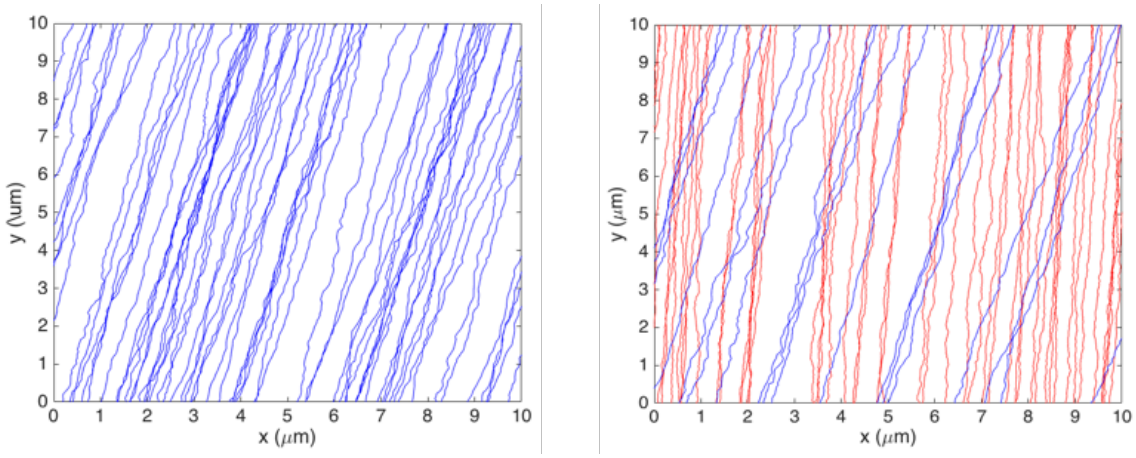


**Figure 4.3.11** Trajectories of the silicon nanospheres with and without the magnetic periodic landscape. Left: The laser is off. The nanospheres are carried by the flow and transport along the flow direction. Right: The laser is on and creates a magnetic landscape. The majority (70 %) of the particles are trapped within the magnetic landscape and the trajectories are deflected by 25°.

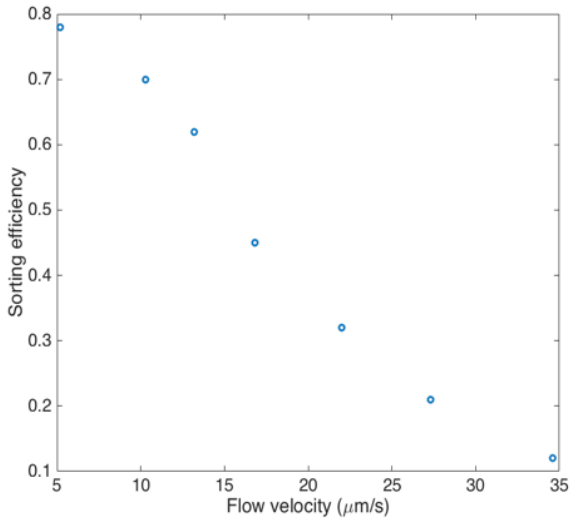

**Figure 4.3.12** Deflection efficiency as a function a flow velocity, taken from statistical analysis of more than 1,200 particle trajectories.

Figure 4.3.12 shows the experimental results for the deflection efficiency, as a function of flow speed, taken from statistical analysis of more than 1,000 particle trajectories. As the flow speed increases, we see a decrease in the deflection efficiency.

We also measured the trajectories of other types of particles in the periodic magnetic landscape, as shown in Fig. 4.3.13. Silica spheres with 1 μm diameter don't support magnetic resonance, and their trajectories are not affected by the magnetic landscape. Silicon particles with 620 nm diameters have magnetic resonance around 1800 nm, which is far from our laser wavelength of 1570 nm. Similarly, these silicon particles cannot be trapped and deflected by the magnetic light.

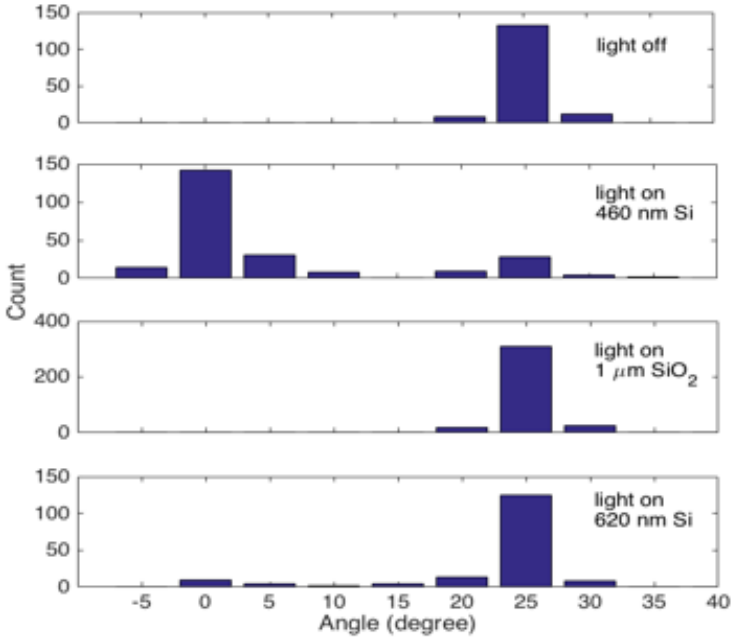


**Figure 4.3.13** Particle trajectories of different type of particles.

## 4.4 Concluding Remarks

We provided the first demonstration that optical magnetism can be utilized for trapping and manipulation of high-index dielectric particles. By interfering two perpendicular travelling light beams, we created a landscape that had periodic magnetic potential and uniform electric potential. We demonstrated that silicon nanospheres that exhibit magnetic dipole resonance could be trapped at the intensity maximum of the magnetic landscape. By adding a driving force to the silicon nanospheres, we showed that their trajectories could be deflected at the encounter of the magnetic landscape. Since the deflection is sensitive to the magnetic dipole strength, the method can be used to achieve optical fractionation based on magnetic dipole moments. We believe that optical forces arising from magnetic interaction have the potential for offering invaluable control parameters for fine contact-free manipulation of micro- or nano-scopic objects.

## References


[1] Ashkin, Arthur. "Acceleration and trapping of particles by radiation pressure." Physical review letters 24.4 (1970): 156.

[2] Ashkin, Arthur, et al. "Observation of a single-beam gradient force optical trap for dielectric particles." Optics letters 11.5 (1986): 288-290.

[3] Phillips, William D. "Nobel Lecture: Laser cooling and trapping of neutral atoms." Reviews of Modern Physics 70.3 (1998): 721.

[4] Ashkin, Arthur, and James M. Dziedzic. "Optical trapping and manipulation of viruses and bacteria." Science 235.4795 (1987): 1517-1520.

[5] Ashkin, Arthur, James M. Dziedzic, and T. Yamane. "Optical trapping and manipulation of single cells using infrared laser beams." Nature 330.6150 (1987): 769.

[6] Block, Steven M., Lawrence SB Goldstein, and Bruce J. Schnapp. "Bead movement by single kinesin molecules studied with optical tweezers." Nature 348.6299 (1990): 348.

[7] Svoboda, Karel, and Steven M. Block. "Force and velocity measured for single kinesin molecules." Cell 77.5 (1994): 773-784.

[8] Korda, Pamela T., Michael B. Taylor, and David G. Grier. "Kinetically locked-in colloidal transport in an array of optical tweezers." Physical review letters 89.12 (2002): 128301..

[9] MacDonald, Michael P., Gabriel C. Spalding, and Kishan Dholakia. "Microfluidic sorting in an optical lattice." Nature426.6965 (2003): 421.

[10] Ladavac, Kosta, Karen Kasza, and David G. Grier. "Sorting mesoscopic objects with periodic potential landscapes: Optical fractionation." Physical Review E 70.1 (2004): 010901.

[11] Pelton, Matthew, Kosta Ladavac, and David G. Grier. "Transport and fractionation in periodic potential-energy landscapes." Physical Review E 70.3 (2004): 031108.

[12] Xiao, Ke, and David G. Grier. "Multidimensional optical fractionation of colloidal particles with holographic verification." Physical review letters 104.2 (2010): 028302.

[13] Spesyvtseva, Susan E. Skelton, and Kishan Dholakia. "Trapping in a material world." Acs Photonics 3.5 (2016): 719-736.

[14] Pelton, Matthew, et al. "Optical trapping and alignment of single gold nanorods by using plasmon resonances." Optics letters 31.13 (2006): 2075-2077.

[15] Toussaint, K. C., et al. "Plasmon resonance-based optical trapping of single and multiple Au nanoparticles." Optics express 15.19 (2007): 12017-12029.

[16] Selhuber-Unkel, Christine, et al. "Quantitative optical trapping of single gold nanorods." Nano letters 8.9 (2008): 2998-3003.

[17] Tan, Shida, et al. "Optical trapping of single-walled carbon nanotubes." Nano Letters 4.8 (2004): 1415-1419.

[18] Marago, O. M., et al. "Femtonewton force sensing with optically trapped nanotubes." Nano letters 8.10 (2008): 3211-3216.

[19] Twombly, Christopher W., Julian S. Evans, and Ivan I. Smalyukh. "Optical manipulation of self-aligned graphene flakes in liquid crystals." Optics express 21.1

(2013): 1324-1334.
[20] Righini, Maurizio, et al. "Parallel and selective trapping in a patterned plasmonic landscape." Nature Physics 3.7 (2007): 477.
[21] Righini, Maurizio, et al. "Surface plasmon optical tweezers: tunable optical manipulation in the femtonewton range." Physical review letters 100.18 (2008): 186804.
[22] Grigorenko, A. N., et al. "Nanometric optical tweezers based on nanostructured substrates." Nature Photonics 2.6 (2008): 365.
[23] Van der Horst, Astrid, et al. "High trapping forces for high-refractive index particles trapped in dynamic arrays of counterpropagating optical tweezers." Applied optics 47.17 (2008): 3196-3202.
[24] Bormuth, Volker, et al. "Optical trapping of coated microspheres." Optics express 16.18 (2008): 13831-13844.
[25] Jannasch, Anita, et al. "Nanonewton optical force trap employing anti-reflection coated, high-refractive-index titania microspheres." Nature Photonics 6.7 (2012): 469.
[26] Monticone, Francesco, and Andrea Alù. "The quest for optical magnetism: from split-ring resonators to plasmonic nanoparticles and nanoclusters." Journal of Materials Chemistry C 2.43 (2014): 9059-9072.
[27] Smith, David R., et al. "Composite medium with simultaneously negative permeability and permittivity." Physical review letters 84.18 (2000): 4184.
[28] Smith, David R., John B. Pendry, and Mike CK Wiltshire. "Metamaterials and negative refractive index." Science305.5685 (2004): 788-792.
[29] Hentschel, Mario, et al. "Transition from isolated to collective modes in plasmonic oligomers." Nano letters 10.7 (2010): 2721-2726.
[30] Fan, Jonathan A., et al. "Self-assembled plasmonic nanoparticle clusters." science 328.5982 (2010): 1135-1138.
[31] Evlyukhin, Andrey B., et al. "Demonstration of magnetic dipole resonances of dielectric nanospheres in the visible region." Nano letters 12.7 (2012): 3749-3755.
[32] Ginn, James C., et al. "Realizing optical magnetism from dielectric metamaterials." Physical review letters 108.9 (2012): 097402.
[33] Shilkin, Daniil A., et al. "Directional Optical Sorting of Silicon Nanoparticles." ACS Photonics 4.9 (2017): 2312-2319.
[34] Andres-Arroyo, Ana, et al. "Optical manipulation and spectroscopy of silicon nanoparticles exhibiting dielectric resonances." Nano letters 16.3 (2016): 1903-1910.
[35] Donato, Maria G., et al. "Optical trapping of porous silicon nanoparticles." Nanotechnology 22.50 (2011): 505704.
[36] Shi, Lei, et al. "Monodisperse silicon nanocavities and photonic crystals with magnetic response in the optical region." Nature communications 4 (2013): 1904.
[37] Crocker, John C., and David G. Grier. "Methods of digital video microscopy for colloidal studies." Journal of colloid and interface science 179.1 (1996): 298-310.

# Chapter 5

# Summary and Outlook

In the recent years, metamaterials and metasurface research has grown tremendously from experiments demonstrating rich physics to enormous potentials for technological advancements. In this dissertation, I have presented my research that focuses on the development of non-conventional metamaterials and metasurfaces that have unique physics beyond the classical regime.

In Chapter 2, I demonstrate the design and application of an anti-Hermitian coupled metasurface, which extend the design principle of metasurface beyond the phase gradient regime. Conventional phase gradient metasurfaces work in the regime where the meta-atoms need to be well separated such that the interaction between neighboring meta-atoms is negligible. Recently, anti-Hermitian systems have gained increasing attention due to their ability to increase the selectivity of resonant devices. Here, an anti-Hermitian coupled metasurface is uniquely positioned to address the optical and electrical crosstalk problem in small pixel color sensors, enabling pixels with subwavelength dimensions, potentially suitable for future optoelectronic systems. By carefully controlling the size and separation of silicon nanocylinders, visible light can be selectively absorbed in multiple color channels with negligible diffraction, leading to spectrally pure absorption profiles of neighboring sub-pixels. Additionally, due to their three-dimensional, non-planar morphology, nanocylinders composed of PIN junctions are inherently immune to electrical crosstalk as charge carriers generated in the intrinsic region are separated by air from the intrinsic region of neighboring sub-pixels. The anti-Hermitian metasurface presented, could have great practical value for the imaging and display industries, where solutions to the small pixel problem are needed.

Chapter 3 brought the classical metasurfaces to the quantum regime. Although typically metasurface is used to control the wavefront of classical light, they can also be applied to manipulate the property of quantum vacuum. Here, we proposed and theoretically demonstrated a judiciously metasurface that can be harnessed at single photon level which opened the door for quantum photonic applications with metasurface. By using a polarization dependent metasurface to engineer an anisotropic quantum vacuum, we have shown that strong quantum interference (coherence) can be induced in three-level systems. Metasurfaces interfaced with quantum emitters and 2D materials have the

potential to opening up opportunities for on-chip quantum state engineering and material property engineering.

In Chapter 4, instead of manipulating light with light-matter interaction, we looked at the reverse problem: optical manipulation of nanostructures' kinetic motion. In the absence of natural magnetism, optical trapping forces have previously been based purely on electric interactions. However, as the emergence of the metamaterial concept, several classes of nanostructures including plasmonic nanoclusters and high-index dielectric particles have been proposed and demonstrated to possess artificial optical magnetism. Chapter 4 provided the first demonstration that optical magnetism can be utilized for trapping and manipulation of high-index dielectric particles. By interfering two perpendicular travelling light beams, we created a landscape that had periodic magnetic potential and uniform electric potential. We demonstrated that silicon nanospheres that exhibit magnetic dipole resonance could be trapped at the intensity maximum of the magnetic landscape. By adding a driving force to the silicon nanospheres, we showed that their trajectories could be deflected at the encounter of the magnetic landscape. Since the deflection is sensitive to the magnetic dipole strength, the method can be used to achieve optical fractionation based on magnetic dipole moments. We believe that optical forces arising from magnetic interaction have the potential for offering invaluable control parameters for fine contact-free manipulation of micro- or nano-scopic objects.